PERFORMANCE INFLUENCE OF LEADING-EDGE TUBERCLES ON A HIGH-SPEED AXIAL COMPRESSOR

INFLUENCES SUR LA PERFORMANCE D'UN COMPRESSEUR AXIAL D'HAUTE VITESSE DES TUBERCULES SUR LES BORDS D'ATTAQUE

A Thesis Submitted to the Division of Graduate Studies
of the Royal Military College of Canada
by

Satpreet Singh Sidhu, B.Eng., M.Eng
Lieutenant

In Partial Fulfillment of the Requirements for the Degree of
Doctorate of Philosophy in Mechanical Engineering

October, 2024

To my mother, as none of this would have been possible without her guidance, love, and support.

Acknowledgement

I would like to thank Dr. Billy Allan for giving me this opportunity to work on this project and for having faith in me. I really appreciate his untiring help and commitment in the writing of my thesis which included multiple iterations. I also appreciate his mentorship throughout the program and his invaluable suggestions and advice. I would sincerely like to thank Dr. Asad Asghar for his indefatigable support throughout the program. I still remember my first day at RMC when I met him and he politely mentioned that we will probably work together. And we worked hard together throughout my research and on several extra projects. It was a pleasure working with him: he was always the person to go to for *any* problem, even some personal advice along the way.

I would like to thank Dr. Perez for his guidance throughout, providing valuable support during different phases of testing. It was always intriguing to listen to Dr. LaViolette sharing his opinion on different aspects of life and fun facts about everyday things. I cannot forget the support from Debbie Fisher during my initial years at RMC. I wish to extend my gratitude to the faculty of RMC Mechanical and Aerospace Engineering department with whom I worked over the years.

This work would not have been possible without the unwavering support from RMC Mechanical and Aerospace Engineering department lab technicians. Specifi-

Abstract

Sidhu, Satpreet Singh. M.Eng. *Performance Influence of Leading-Edge Tubercles on a High-Speed Axial Compressor*. Supervised by William D.E. Allan, B.Eng., M.A.Sc., Ph.D., P.Eng., Professor.

    Gas turbine engines are one of the crucial innovations of the modern world and developments have progressed from their introduction almost a century ago. Historically the compressor has been the target of engineering improvements, including efforts to expand performance and operability. Engine performance is governed in part by achievable compressor pressure ratio, which is limited by compressor stall. To mitigate this, many active and passive flow control devices have been tested over the decades, most of which have never had a practical application. But a bio-inspired passive flow control device known as a *tubercle* has shown promising results when applied to aircraft wings and other lifting surfaces, including 2-D compressor profiles. In this work, a three-phase programme involving tubercle optimization, 2-D and 3-D experiments have been undertaken to better understand performance improvements in various airfoil operation regimes. Self-Organizing Maps (SOM), an artificial neural network technique, were used to compare tubercle geometric and performance parameters. Two new geometric parameters: Reynolds number based on hydraulic diameter and tubercle aspect ratio, and one new performance parameter:

post-stall operability area are introduced in this work to characterize the 3-D flow associated with tubercles. SOM results indicated that higher maximum coefficient of lift and stall angle can be achieved with lower tubercle amplitude and wavelength. Low-speed wind tunnel tests were conducted to expand the data set and findings indicated that optimized geometry is around amplitude of 3% chord and wavelength of 11% chord. A compressor cascade was designed based on the *Rolls-Royce* A-250 first stage rotor blade mean conditions. Total pressure measurements, flow visualization and pressure sensitive paint were used to assess tubercle and baseline performance. Against a range of tubercled test articles, the 3% chord amplitude and 11% chord wavelength geometry was ultimately selected for 3-D testing in the *Rolls-Royce* A-250 axial compressor at operational static conditions. Compressor blades were modified using Electrical Discharge Machining and the compressor with both modified rotor and stator blades showed performance improvements at 80% speed when tested with bleed valve partially open. But these trends were not sustained at higher speeds. The A-250 stall is characterized by stall cell formation at the first stage, eventually developing into compressor stall. Of significance, when tubercles were installed, the compressor successfully eliminated stall cell formation until stall initiated in the final stage, defying the predictions of the Greitzer model. Despite the overall reduced compressor map performance, tubercles successfully increased pressure ratio at 80% even with open bleed valve. Tubercles can potentially improve the overall performance if optimized to individual compressor stages and with improved manufacturing methods.

Keywords: Gas turbine engines, Compressor, Axial compressor, Compressor stall, Compressor surge, Optimization, Tubercles, Passive flow control.

Résumé

Sidhu, Satpreet Singh, M.Eng., *Influence des performances des tubercules de pointe sur un compresseur axial à grande vitesse*. Thèse dirigée par William D.E. Allan, B.Eng., M.A.Sc., Ph.D., P.Eng., Professeur.

    Les turbines à gaz sont une des innovations des plus importantes du monde moderne et on les a développés beaucoup depuis leur introduction il y a presqu'un siècle. Le compresseur est, depuis longtemps, le focus des ingénieurs pour les améliorations, comprenant l'expansion de performance et d'opérabilité. Parmi autres facteurs, la performance d'un moteur est régie par le rapport de pression, qui est lui-même limité par le décrochage. Afin de mitiger le décrochage, plusieurs méthodes de la commande passive et active d'écoulement ont été essayés depuis les décennies généralement sans application pratique. Mais une méthode passive bio-inspirée, des *tubercules*, a montré des résultats promettants quand évalué sur les ailes et d'autres applications, comme les profils 2-D de compresseur axial. Lors de ces travaux, un programme expérimental en trois phases comprenant l'optimisation des tubercules, et évaluations en deux et trois dimensions a eu lieu afin de mieux comprendre la performance améliorée dans certains régimes d'opération. *Self-Organising Maps* (SOM), une méthode de réseau neuronal, a été employé pour comparer des paramètres géométriques des tubercules aux paramètres de performance. Lors de

cette recherche, on a introduit des nouveaux paramètres, deux géométriques soit le nombre de Reynolds basé sur le diamètre hydraulique des tubercules et aussi leur allongement, et un de performance: la région d'opérabilité après décrochage, pour caractériser les écoulements en 3-D introduites par les tubercules. Les résultats de SOM ont indiqué qu'un coefficient de portance maximale et angle de décrochage peuvent être élevés avec des amplitudes et longueur d'onde des tubercules plus faibles. En suites, les essaies dans une soufflerie de basse vitesse ont supporté les conclusions du SOM pour la géométrie optimale des tubercules: une amplitude de 3% de la corde et une longueur d'onde de 11 de la corde. On a conçu une grille d'aubes de géométrie et condition d'opération statique du premier étage de rotors du compresseur axiale du turbomoteur *Rolls-Royce* modèle A-250. Les aubes de compresseur ont été usinées par décharge électrique et le compresseur si modifié a démontré une performance améliorée jusqu'à une vitesse de 80%. Mais cette tendance n'a pas continué aux vitesses plus élevées. Le décrochage de A-250 est caractérisé par la formation des cellules de décrochage au premier étage du compresseur qui développent à un décrochage global de l'avant jusqu'à la sortie. C'était significatif que les tubercules ont éliminé la formation de ces cellules, et le décrochage a eu lieu au dernier étage, contre aux prédictions du modèle Greitzer. Néanmoins la performance réduite aux vitesses élevées, les tubercules ont augmenté le rapport de pression à une vitesse de 80% même avec une valve de prélèvement ouverte. Les tubercules, si optimisés aux étages individuelles et usinés avec une méthode précise, peuvent améliorer la performance globale d'un compresseur axial.

Mots clés: Moteurs à turbine à gaz, Compresseur, Compresseur axial, Décrochage du compresseur, Surtension du compresseur(Pompage), Optimisation, Tubercules, Contrôle de débit passif.

Statement of Contribution

This work on the first experimental application of tubercles to a high speed axial gas turbine compressor was initiated after many studies suggested that airfoil performance could be improved with the use of leading edge tubercles.

Here, a literature survey was performed on the existing tubercle studies to understand the flow phenomena to compare different theories on how they contribute. It was found that existing geometric parameters were not sufficient to characterize the 3-D effects introduced by tubercles. So in this work, two new 3-D tubercle geometric parameters were introduced which showed moderate-to-strong correlation with airfoil performance parameters. These geometric parameters contributed to the understanding of how tubercles generate a pair of stream-wise counter rotating vortices with enough strength to delay boundary layer separation. It was found that tubercles tend to perform when they have a pitchwise aspect rather than tiny delta wings, as widely believed in the scientific community. A novel way to quantify performance improvements in post-stall regime was proposed to compare overall performance benefits of tubercles. Self-Organising Maps (SOM) were used on a wide range of experimental studies in an attempt to correlate geometric and performance parameters, something that had not been done at this scale prior to this study. The existing experimental dataset was also expanded to explore geometric parameters outside the

dataset.

Results from the SOM were used to select promising tubercle geometries for testing in a 2-D compressor cascade at first stage rotor, mid-span flow conditions. This was the first application of tubercles to compressor blades at high Mach number and flow visualization illuminated tubercle flow phenomena. The influence of different tubercle geometry was explored and compared, including those departing from conventional sinusoidal patterns, using wake pressure deficit.

Finally in a pioneering application of EDM to hardened compressor blades, tubercles were manufactured onto the leading edge of *Rolls-Royce* A-250 compressor blades in the first application of tubercles on an operational gas turbine compressor. Baseline and modified compressor profiles were tested at speeds ranging from 60% to 95% maximum rotational speed. The A-250 compressor is known to have stall cell formation at the first stage rotor, complying with Greitzer's theoretical model. Interestingly, it was found that the modified compressor stall characteristics were fundamentally altered by the tubercles, with completely eliminated stall cell initiation. Stall was not observed at any stage, defying the Greitzer model and a novel mode evolved whereby later compressor stages stalled first, leading to a forward propagating full compressor stall. This study showed tubercle potential in delaying stall when they are optimized for all compressor stages and are precisely manufactured.

Contents

List of Tables

List of Figures

Nomenclature

Symbols

$Æ\!R$	Aspect ratio [-]
A	Amplitude,% c
A/L	Amplitude to wavelength ratio [-]
b	Span [mm]
C	Coefficient [-]
c	Axial chord [mm]
I	BMU neuron
i	Angle of incidence [°]
m	Weight of a neuron
P	Pressure [psi]
Re	Reynolds number [-]
S	Lateral distance between neuron
s	Pitch [mm]
T	Lateral interaction effect factor
t	Each iteration
x	Specific neuron

Greek Symbols

α Angle of attack [°]

β Metal angle [°]

δ Stagger angle [°]

η Learning rate

γ Total pressure loss coefficient [-]

λ Wavelength,%c

π Pressure ratio [-]

σ Size of neighbourhood

θ Tubercle angle [°]

Subscripts

0   Total properties

1   Inlet

2   Exit

c Chord

d Drag

Dh Hydraulic diameter

l Lift

max Maximum

p Pressure

s Static or stall when used with α

Abbreviations

$2-D$ Two-Dimensional

$3-D$ Three-Dimensional

AoA   Angle of Attack

AOI   Angle of Incidence

BMU   Best Matching Unit

LE   Leading Edge

LIE   Lateral Interaction Effect

RMC   Royal Military College of Canada

SWCRV   Stream-wise counter-rotating vortices

TE   Trailing Edge

1 Introduction

1.1 Gas Turbine Engines

In the post Second World War era, gas turbine engines have been largely considered as the future of aviation due to their high thrust-to-weight ratio that presents enormous potential for flight at high speed and altitude. Reciprocating engines were increasingly limited by demands for greater thrust, forward speed and altitude, so their use was restricted to small aircraft. Over the decades, gas turbines have also found their applications in other areas like power generation and marine propulsion. Gas turbine engines of various sizes have been developed and used for many aviation applications including helicopters, fighter jets, civilian airlines and recently, drones. The advantages of gas turbine engines include efficiency at higher speeds, power density, high power-to-weight ratio, reliability and durability, altitude performance, versatility and reduced frontal area.

Gas turbine engines have revolutionized air travel, improving global connectivity along with business and trade. Aviation is one of the major contributors to global economics and job creation. Military dominance has historically relied on ground forces but with the aviation advancements from gas turbine engines, air power has become one of the major forces. Aircraft powered by gas turbine engines project

power with implications for defense strategy, humanitarian missions, and disaster response, always enabling rapid deployment of troops and equipment. Developments in the gas turbine engines have led to innovations in material sciences, aerodynamics and manufacturing technologies. Advancements in these disciplines have led to the development of many spin-off technologies like advanced control systems, high-temperature materials and precision machining.

Gas turbine engines are a type of internal combustion, air-breathing engines. The concept was brought to life by two engineers around the same time frame in the 1930s. Frank Whittle in United Kingdom and Hans von Ohain in Germany worked independently on their designs and produced their respective first gas turbine engines during the Second World War. A basic gas turbine engine layout consists of a compressor, combustion chamber and a turbine stage as shown in Figure 1.1. The compressor draws ambient air into the engine and delivers pressurized air to the combustion chamber. Fuel is injected for burning in combustion chamber and combustion gases at high temperature and pressures are delivered to the turbine inlet. The gas expands through the turbine blades, rotating the rotors for power generation, part of which drives the compressor. A gas turbine engine follows the Brayton thermodynamic cycle as shown in Figure 1.2. The layout of the gas turbine engine changes for different applications, and components, for example, the compressor and turbine could be modified for the desired application. Gas turbine for aircraft engines are categorized as: turbojet, turbofan, turboprop and turboshaft engines.

When designing a gas turbine engine, the two basic thermodynamic variables available to a designer are the pressure ratio (PR) generated by the compressor and the turbine entry temperature (TET) (T_4 in Figure 1.2). Performance for a simple gas turbine cycle is measured using cycle efficiency and specific output. The cycle ef-

2
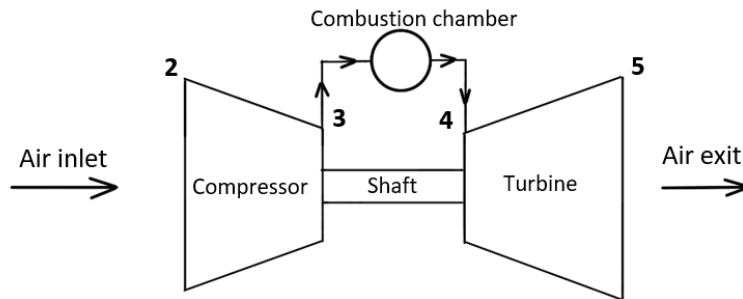
Figure 1.1: Gas turbine engine layout

ficiency and specific output can be increased by simply increasing TET, but that is limited by the maximum temperature that turbine nozzle and blades can sustain. Advancements are being made in turbine blade materials including ceramic coatings, advanced materials, manufacturing and blade cooling techniques. This also results in increased engine complexity. Overall PR is another variable that can be optimized for improved cycle efficiency and specific output. A compressor is designed to achieve a specific PR to efficiently meet the desired output for design flight conditions. PR is the primary objective for achieving compressor performance improvements in this work.

For an aircraft gas turbine, performance is measured using the specific fuel consumption (*SFC*) and specific thrust. The effect of increasing PR is a reduction in *SFC*. Specific thrust increases initially with PR then decreases after an optimum PR is reached, as a function of TET and inlet stagnation temperature. Gain in *SFC* and specific thrust is usually diminished with increased engine weight, complexity and cost since more compressor stages are usually required.
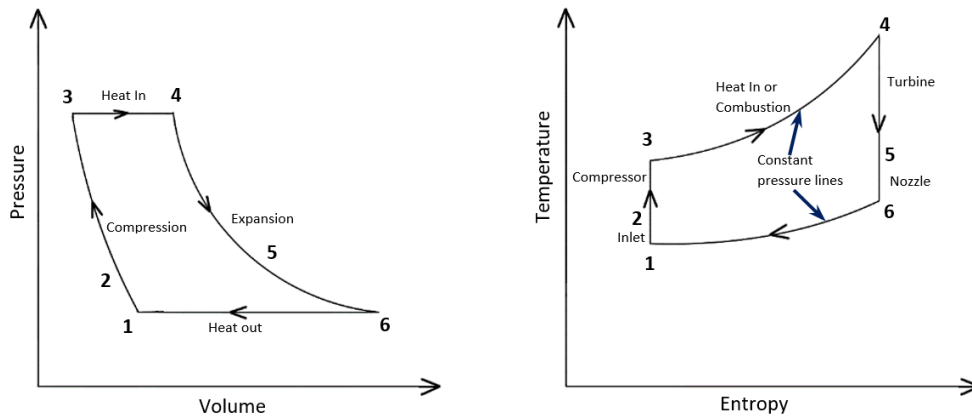
Figure 1.2: Brayton cycle

1.2 The Compressor

Another advantage of the gas turbine engine is the ability to design each component individually. Two compressor configurations are commonly used in gas turbines: axial and centrifugal. In axial compressors, the working fluid flows parallel to the axis of rotation as shown in Figure 1.3 (a). Centrifugal compressors turn the fluid radially at their discharge, perpendicular to the axis of rotation as shown in Figure 1.3 (b). Both axial and centrifugal compressors have their own advantages, with smaller engines usually employing centrifugal compressor to benefit from high PR generating capabilities and relatively reduced mass flows. Centrifugal compressors are shorter axially, more resistant to foreign object damage, and robust in handling a range of mass flow rates at a fixed rotational speed. They require a much bigger engine cross sectional area to increase mass flow rate and are normally restricted to single-stage due to increased duct complexity with multiple stage configuration. Axial compressors have the advantage of handling much larger mass flow rate for

a given engine frontal area, and therefore to the generation of higher thrust. Axial compressor stages can be stacked to increase overall PR. With increased demands for power and thrust, it was clear early on in gas turbine development that axial compressors had a greater role to play in the future. Over the years, internal aerodynamic research led to increases in overall PR for both designs. Centrifugal compressors have also been improved with advanced materials, reaching PR as high as 8:1 from a single stage. Similarly, for multistage axial compressors, some turbofan engines are capable of reaching 40-60:1 PR. In larger aircraft gas turbine applications, axial compressors are mostly used for their smaller cross sectional area and higher mass flow capacity. For smaller engine applications, centrifugal compressors can be employed alone or in a combination of axial and centrifugal modules called *axi-centrifugal* compressors.
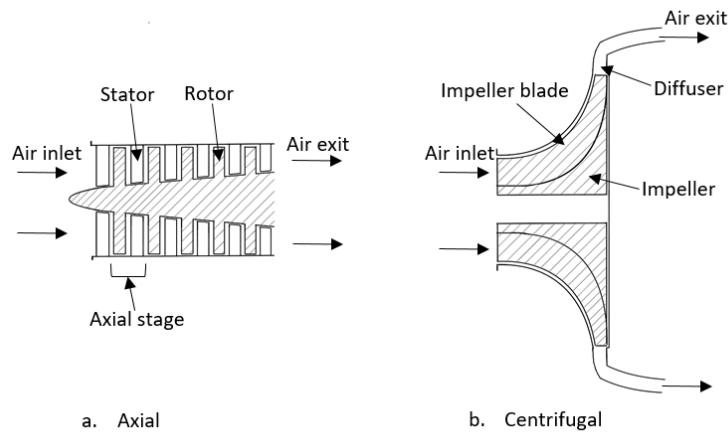
Figure 1.3: Compressor geometries

1.2.1 Axial Flow Compressors

This research will only apply to one of the two configurations, the axial compressor. These are comprised of sets of rotating and stationary rows of blades respectively called rotors and stators. An axial compressor stage is a pair of one rotor and one stator as indicated in Figure 1.3 (a). Fluid entering the compressor is accelerated by the rotor increasing the kinetic energy of the fluid. Absolute velocity of the fluid is increased by the rotor while the stator converts the kinetic energy to static pressure by decelerating the fluid. This process of an increase in pressure is repeated stage after stage, resulting in the overall fluid static pressure increasing to the design output. Rotor and stator blades are designed based on a airfoil shape, essentially acting like small wings. Compressors blades are subject to adverse pressure gradients and always operate at the risk of blade stall. This is a phenomenon whereby fluid departs from the blade suction surfaces, and localized flow reversal occurs. This phenomenon can lead to blockage in part or on all of the compressor annulus that can deteriorate compressor performance.

1.2.2 Compressor Performance

Once a compressor is designed, its performance is charaterized using a compressor map that presents the operating range of compressor, reflecting pressure ratio, mass flow rate and rotational speed. A generic axial compressor map is shown in Figure 1.4. Constant rotational speed curves start at the bottom left of the graph representing lower pressure ratio and specific mass flow rate. At a given rotational speed, as load is placed on the compressor the compressor operating point moves up and left along these curves in the direction of increasing pressure ratio. Compressor pressure ratio

can increase only up to a critical point called *Surge limit*. Compressors approaching surge experience blade stall, and eventually full compressor surge. The diagonal solid line in Figure 1.4 indicates the minimum operable flow rate for a given rotational speed. A compressor will be in an unstable regime when operating to the left of its surge limit. Usually, a valve for later stages or variable stator blades are used during start to ensure a compressor or some of its stages do not enter an unstable region at lower rotational speeds. During compressor start-up, it is desired that the machine follow the operating line shown in Figure 1.4 leaving a stability margin from the surge line.
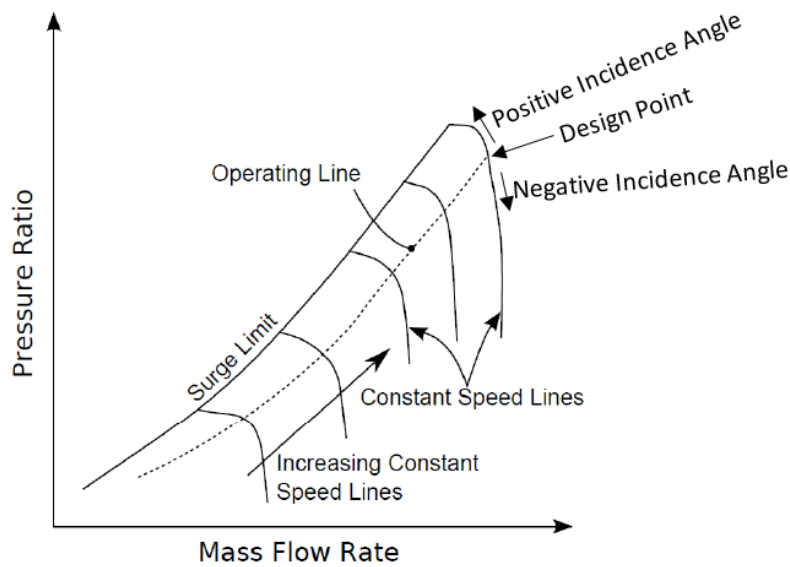
Figure 1.4: A sample axial compressor map

For aircraft gas turbines, weight saving is desired in order to improve the overall performance of the aircraft. With any increase in stage PR, a benefit to overall performance can be achieved in two ways: an increase in PR can result in achieving

7

optimum PR for a given turbine inlet temperature, thereby reducing specific fuel consumption and increasing the specific thrust. Alternatively optimum PR can be achieved using fewer compressor stages resulting in weight savings. With an increase in PR, the increased risk of engine stall exists. A compressor is usually designed based on compressor aerodynamic theory and supporting experiments; it must balance between achieving high pressure ratio and maintaining flow stability.

The objective of this work is to increase the PR of the axial compressor while improving stall characteristics. Many ideas have been explored by various researchers to actively or passively control compressor flow and delay stall to achieve higher PR without reducing stability margins. Some active flow control devices were able to predict the compressor stall but their extra weight and associated reliability concerns prevented their practical application. Some passive flow control devices also improved stall characteristics while being reliable and adding no extra weight, but their presence at design conditions often led to reduced efficiency.

1.3   Research Motivation

The motivation of this research is to determine if a novel application of passive flow control has the potential to increase the stall limit of an axial compressor in order to achieve higher PR. Stall is one of the limiting factors for high compressor performance and a compressor is designed with an operational stability margin for safety. Even a slight delay in compressor stall can result in beneficial increase in PR. Passive and active control devices have been tested over the years, seeking to improve compressor performance but either they employ complex mechanisms or result in reduced efficiency. However, a new bio-inspired flow control device, called leading edge tu-

bercles, has a potential to mitigate stall and is introduced to a high speed compressor in this work. Tubercles were reported by Fish *et al.* [11] in 1995 on the leading edge of humpback whales flippers shown in Figure 1.5. Theirs and subsequent studies have indicated that tubercles help these marine creatures to perform tight manœuvers to catch prey. Over the years, tubercles have been tested on many applications including wings, fans, propellers and marine propellers [12–15]. Their application on compressor blade leading edges was first reported by Keerthi *et al.* [16], where they showed significant improvements in compressor stall characteristics achieved from increases in stall angle. The test blades were operated at very low Mach numbers but nevertheless, it was concluded that the tubercles presented performance improvement potential in their application on gas turbine compressor blades.
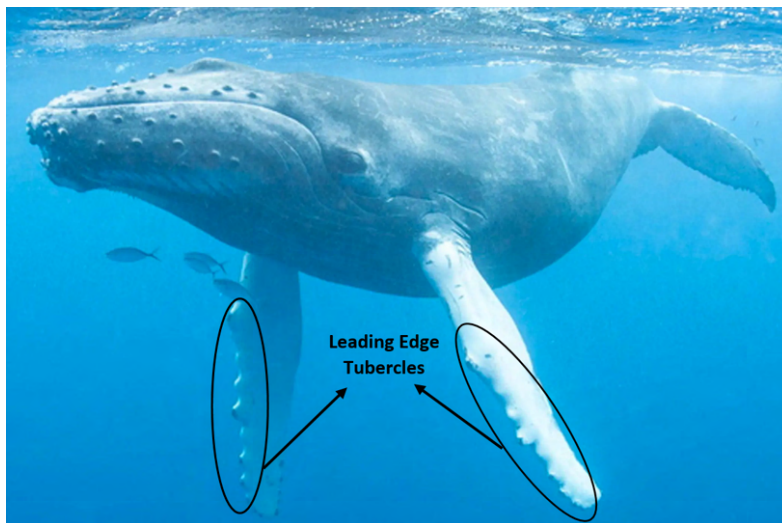
Figure 1.5: Image of an humpback whale displaying tubercles on leading edge of its flipper (modified from [3])

1.4 Research Goal

The goal of this research was to delay stall and increase PR of compressor by modifying leading edges of blades with an optimized tubercle geometry. It provided an opportunity to study the influence of tubercles on compressor blades, both rotors and stators. Improvements can eventually result in higher performance from the same number of compressor stages or perhaps the same PR with fewer compressor stages, with associated weight saving advantages.

1.5 Thesis Outline

This thesis has been divided into five chapters, with the introductory materials found here in the first. Chapter 2 presents background theory and a literature review, including compressor flow control techniques and tubercle performance in various applications. Chapter 3 introduces the methodology used for the research over a range of test campaigns. It explains the approach used for the tubercle shape optimization, design, setup and instrumentations used during cascade testing campaign and finally the setup, intrumentations and data processing of a full scale operational A-250 axial compressor testing. Chapter 4 presents the results from all stages of the research, including an explanation of optimization outcomes and decisions subsequently made for tubercle shape selection. Other results included the cascade testing and those from wake surveys, flow visualization and pressure sensitive paint tests. Finally the operational A-250 compressor results are discussed, comparing compressor maps, and exploring the differences in stall inception for the modified and baseline compressors. The final chapter, chapter 5 presents conclusions from the work along with recommendations for future research.

2 Background theory and literature survey

This work on the assessment of tubercles as a passive flow control device for a high speed axial compressor required understanding of a range of subjects pertinent to the different experimental phases. Tubercles have been widely tested on wings at high Reynolds number. The understanding of external aerodynamics is required to analyze the phenomena affecting the contribution of tubercles. Compressor blades are essentially tiny wings, so the effects of tubercles on compressor blades in a 2-D cascade was required for assessing optimization. This further required the understanding of internal aerodynamics and the performance of compressor blades. The final phase of this work required the evaluation of tubercle shapes on actual compressor blades in a 3-D compressor rig which required the understanding of rotor and stator aerodynamics and compressor performance parameters.

This chapter includes a review of research conducted on basic flow phenomena required to analyze the tubercle performance on wings, 2-D compressor blades and compressor rotor and stator blades. The basics of external aerodynamics are briefly explained to facilitate the understanding of fundamental tubercle behavior.

2.1 An External Aerodynamics Perspective

Boundary layers are categorized into two types: laminar and turbulent. A laminar boundary layer is a very smooth flow of fluid around the surface whereas a turbulent boundary layer contains swirls and eddies, as sketched in Figure 2.1. Evident to the left of that sketch is the early flow where the fluid interacts with the solid surface, and it develops a laminar boundary layer. Reynolds number (Re) is a relation used to characterize the flow, non-dimensionally characterizing the ratio of inertial and viscous forces within a fluid. For airfoils, chord length (c) is used to calculate Re_c. Now, considering the central region in Figure 2.1, as the the flow progresses along the solid surface, the Re_c approaches the transition regime (usually around 5×10^5 for flat plate), and gradually transitions into a turbulent boundary layer. The velocity profiles for both laminar and turbulent flow are sketched schematically in Figure 2.1 as well, indicating much more momentum transfer in a turbulent boundary layer than in a laminar one. This is easily seen in the lowest layers where flow acceleration normal to the surface is more rapid in the turbulent boundary layer (right side of Figure 2.1) than in the laminar boundary layer (left side of Figure 2.1). This ability to exchange momentum from the free stream flow into the lower levels of turbulent boundary layer makes it robust and promotes attachment when presented with an adverse pressure gradient.

The boundary layer around an airfoil is usually attached at lower AoA. At increased AoA, air velocity on the suction surface must increase, to honour the Kutta condition at the trailing edge, to a point beyond which it must decelerate. This deceleration creates a positive pressure gradient to match downstream higher pressure. At the higher AoA sketched in Figure 2.2 (b) air encounters a point (C) where flow is
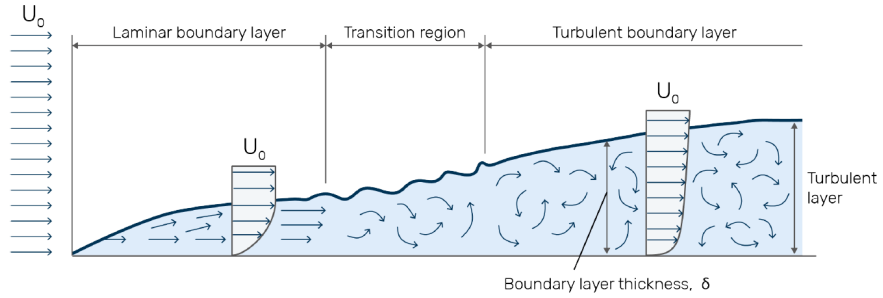
Figure 2.1: Boundary layer transition from laminar to turbulent [4]
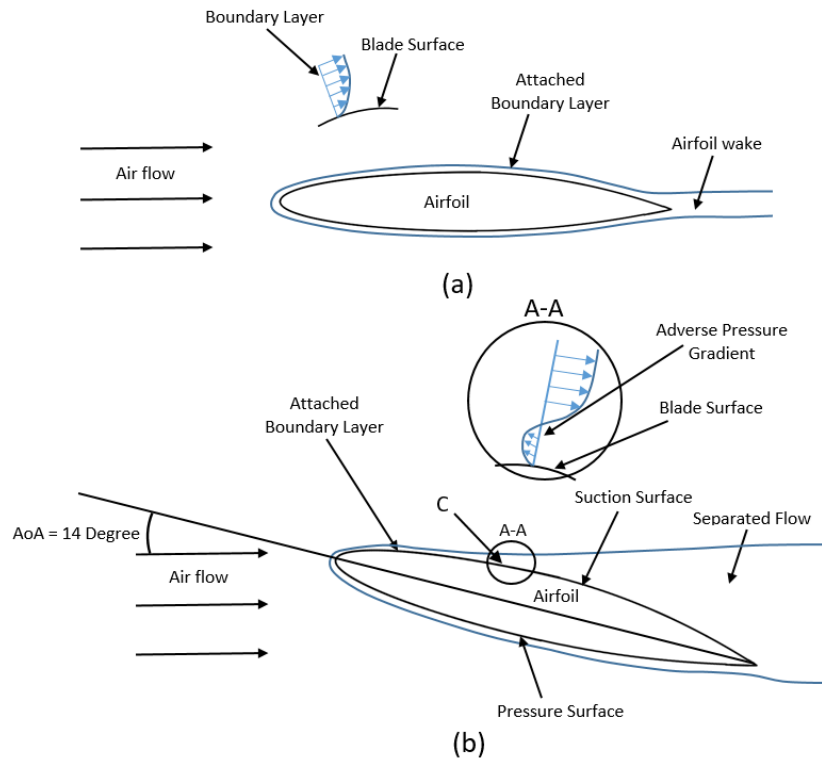
Figure 2.2: Boundary layer separation at high angle of attack (AoA)

unable to remain attached. Avoiding a vaccum, proximal flow reverses as shown in Section A-A. At low AoA, airfoil boundary layers are laminar close to the stagnation region. Re_x based on the linear distance (x) increases as fluid travels chordwise usually with a transition from laminar to turbulent in Re range $3 \times 10^5 \leq Re_x \leq 1 \times 10^6$. A turbulent boundary layer is capable of resisting adverse pressure gradients better than a laminar one, due into their characteristic ability to attract freestream momentum to the sub-layers.
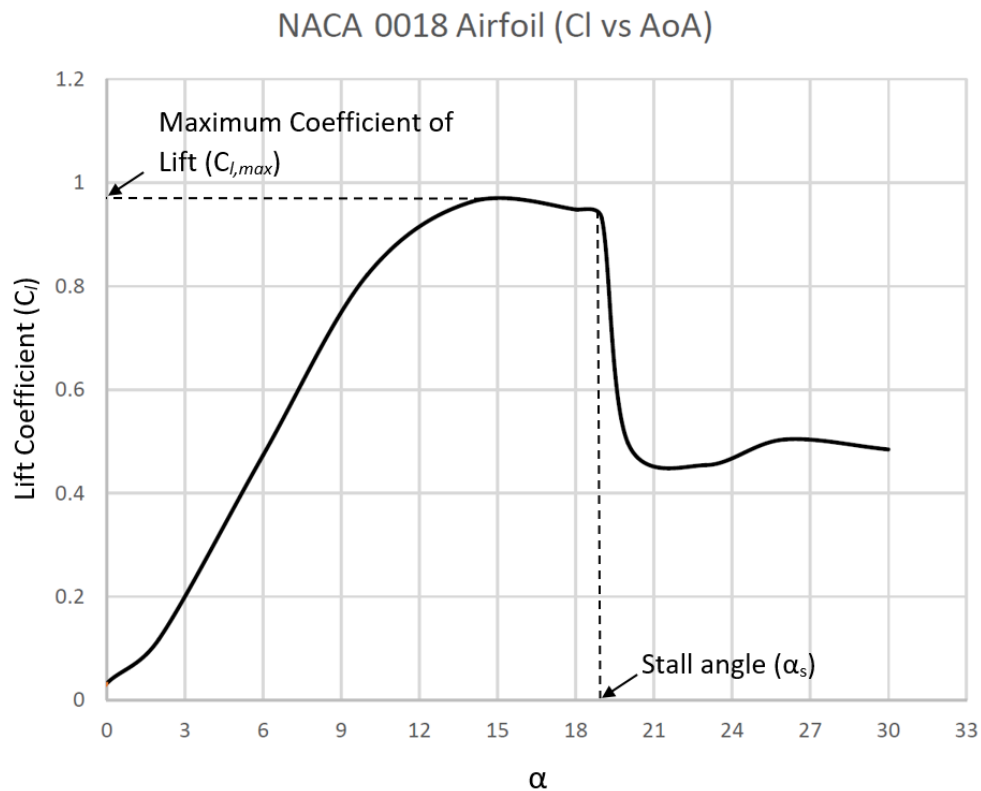
Figure 2.3: NACA 0018 airfoil lift characteristics in subsonic regime [1]

For an airfoil, the evaluation of lift is governed by a coefficient of lift (C_l). Higher

14

C_l values indicate the greater capability of airfoil to generate lift. With increases in AoA, airfoil C_l increases roughly linearly, reaching a maximum $C_{l,max}$ at the point of stall, for example, approximately 0.97 in Figure 2.3. Increasing AoA further results in a loss of C_l and consequently, lift. At this point, flow separates from the airfoil suction surface due to the elevated adverse pressure gradient.

2.2   Internal Aerodynamics

Compressor aerodynamics differs from external aerodynamics since the fluid flows through a passage with combined effects of multi surface boundary layers. To interpret complex compressor aerodynamics, understanding each flow effect becomes very important. Flow entering the compressor is accelerated by the rotor, the blades of which act as tiny wings whose relative and absolute fluid velocity define flow characteristics. Stator aerodynamics is different, since they experience fluid at much lower velocities, but they must diffuse the flow increasing fluid static pressure, with commensurate adverse pressure gradient challenges.

2.2.1   Rotor Aerodynamics

Rotors experience incoming fluid at different local velocities at hub compared to the tip, due to rotation. For the design of a compressor, these flow calculations are incorporated and the rotor blade shapes are modified to accomodate changing flow geometries. The presence of a range of characteristic vortices in an axial compressor stage presents more challenge to the blade designer. In order to meet compressor performance expectations, rotor blades are designed to influence flow to reduce losses. 3-D compressor blades modified for this work are twisted, swept or leaned, as part of

their original design. An understanding of blade design allowed flow velocities to be calculated at different span locations. This influenced the final tubercle parameters for this work.

2.2.2 Stator Aerodynamics

Stator blades are the stationary set of blades that act as diffusers, recovering the kinetic energy added to the fluid in the rotor row in the form of increased static pressure. Stall inceptions are mainly concerned with the rotor blades due to the rotational component. Stators experience absolute flow at much lower velocities, something that is expected to cause early stall near the endwalls. Stator aerodynamics in a multi-stage compressor is adversely affected by rotor tip leakage flow and stalled rotor blades. These different flow conditions of stator blades are important to understand the tubercle application and performance in final testing phase of this work.

2.2.3 Compressor Stall

While the subject of this work is flow control, it will become apparent that an understanding of the flow physics of compressor stall will be crucial to its outcome. Compressor rotor stages or stator rows are essentially a series of tiny wings in an enclosed space, assembled on rotors and in stator rows after careful analysis and testing while flow is designed to be at an low angle of incidence (AOI). However, due to flow conditions or other instabilities, AOI can increase, resulting in the flow separation leading to blade stall, such as that shown schematically in Figure 2.4.

Over the past decades, much progress has been made to understand better compressor internal aerodynamics and stall. Designs have improved with improved analysis, the emergence of increased computational power and extensive experimental

work. However, compressor stall is still a major limiting factor in gas turbine design. Incidents still happen due to compressor stall, some resulting in grave and even fatal consequences. Stall inception studies are conducted to better characterize the flow conditions that lead to undesirable operating modes, so as to set appropriate safety margins.

Full understanding of compressor internal aerodynamics is still a work in progress. Emmons *et al*. [17] were among the first researchers to investigate stall inception. Compressors were known to become unstable at low speeds where performance decreased with typical symptoms including audible thumping and excessive noise emanating from the inlet and exit, both clear signs of surge. Emmons *et al.* created a 2-D compressor model as a series of parallel channels [17]. The presence of small compressor blockages was linked to the flow instability.
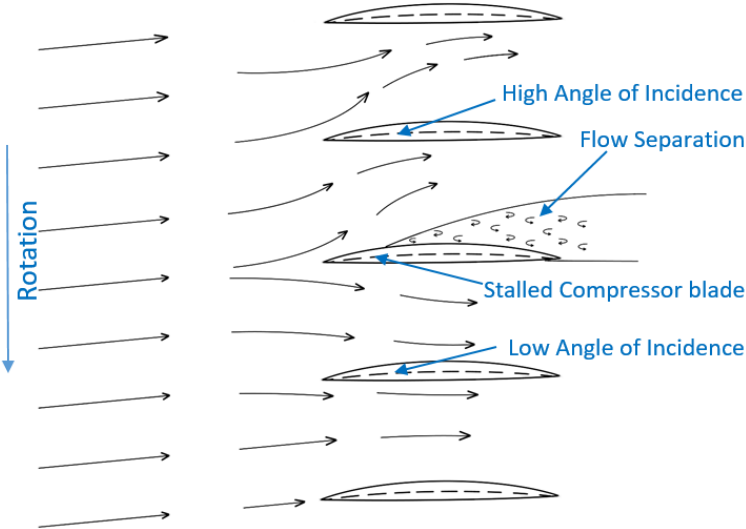
Figure 2.4: Compressor blade stall

A compressor will generate a higher pressure ratio at a constant speed as the mass flow decreases where compressor blades operate closer to their stall limit. At the point of maximum pressure ratio, a compressor becomes very sensitive to the oncoming flow irregularities or instabilities. When such a disturbance occurs, a momentary overloading of the blade will result, possibly leading to a local and intermittent flow separation from the blade surface. This can cause a flow blockage: a stall cell in single or multiple blade passages, as shown in Figure 2.4. Specifically in the case of a rotor blade row, rotation results in increased AOI for the suction side blade adjacent to a blockage. Similarly the pressure side of the adjacent blade will encounter reduced AOI. The stalled rotor blade in the middle will follow suit, leading to its unstall as the stall cell progresses towards the blades on the suction side. Due to the rotational effect, a stall cell will rotate in the same direction as rotor blades but will always rotate at a slower speed than the rotor. A cell like this is referred to as a disturbance on a short length scale. Figure 2.4 is a simple schematic of this and in this case, only one blade is stalled.

Finite Element Analysis (FEA) by Takata *et al.* [18] concluded that compressor operation stability limit is reached when the slope of the total-to-static pressure ratio curve is zero. Studies were performed to understand the stall characteristics and the methods to recover an engine from stall. McKenzie [19] proposed a model to predict the extent of stall, differentiating full-span from part-span stall cells. Later studies by Day *et al.* [20] elaborated on this work using an experimental campaign to analyze the hysteresis loop of a multi-stage compressor as it recovered from stall. Day and Cumpsty [21] used fast-response instrumentation to investigate the presence of a stall cell and related flow behaviour. It was found that the flow continues circumferentially inside a stall cell, in the direction of rotation creating blockage in the annulus. Flow

in a stalled annulus has a reduced axial velocity component, preventing the cell's advance through the compressor. These measurements supported the theory that a stall cell rotates in the same direction as a rotor and always at lower speeds. Day [19] found that inlet guide vanes (IGV) affected stall cell speed more than the rotational speed, blade profile and tip clearance.

Initially, stall cells were thought to develop into full compressor stall. Day observed spike type distrubances around the rotor tip region [22] rotating at about 70% rotor rotational speed. These disturbances were different from previously reported modal type disturbances, one of two types of stall inception.
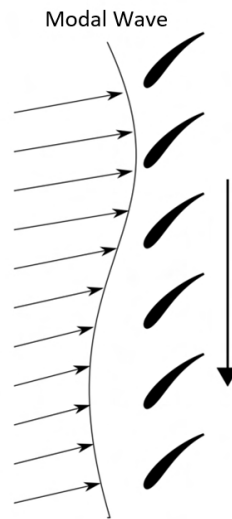
Modal Wave

Figure 2.5: 2-D sketch of a modal wave in a compressor annulus [5]

The second type is known as a *modal inception*, also referred to as a *pre − stall wave*, characterized by velocity perturbations before stall onset as observed by Moore, Greitzer, and Hynes [23–25]. First proposed by Emmons *et al*. [17] and

later elaborated upon by Moore and Greitzer [23], this theory was never analytically proven. In 1990, a study by McDougall *et al.* [26] employed hot-wires and Kiel probes to perform a flow survey for better flow resolution. They reported first-order, modal type flow disturbances around the annulus. It was estimated that the speed of rotation of a modal type disturbance was on the order of 50% rotor speed. The order of a modal disturbance depends on the wavelength of velocity fluctuations around the circumference of the annulus. Figure 2.5 shows a rotor blade row moving top-to-bottom with a velocity fluctuation wave upstream also moving along the blade row, but at a lower speed. It was observed by McDougall *et al.* [26] that such velocity perturbations can exist even when a compressor is not operating close to its stall point, but at very small amplitudes. They observed an amplitude rise when the compressor approached its stall point and were first to reveal modal type perturbations experimentally.

McDougall *et al.*'s [26] experiments concluded that compressor stall was more likely to occur in a rotor with high reaction stages. However, tip clearance determined whether stall occurs at the tip or the hub of the blades. For a compressor with low tip clearance flow, blockage was observed at the hub, while stall was most likely to be observed at the casing for stages with large tip clearances, most often the case for multi-stage compressors. They observed that a rise in amplitude of modal oscillations led to surge.

The presence of both spike and modal stall near the surge limit is not mandatory for stall to occur. However, it was noted that if a finite cell forms first in the compressor, then it rapidly grows, disturbing flow symmetry and modal oscillations do not form. Moreover, if modal oscillations form before a stall cell, the cell can influence or excite oscillations, leading to stall or surge. It was noticed that coupling between two

20

simultaneous disturbances is weak, as long as a stall cell is small circumferentially. However, when a stall cell increases significantly in size, it will appear in phase with modal oscillations; and coupling will smoothly develop without any abrupt change in amplitude or speed.

In summary, spike type distrubances can be initiated at a single blade, eventually affecting overall compressor performance. Modal type disturbances are usually on full compressor scale and can trigger complete compressor stall close to, or at, the static-to-total pressure peak. Research on the stall characteristics has found that compressors can encounter different spike-type stall initiations including features such as front end start-up stall, multi-cell part-span stall, spike modes and abrupt stall at full speed [27].

Stall inception has been explained by Greitzer *et al.* [28] who suggested that by using the *B-Parameter*, compressor stall or surge can be predicted, and specifically, which will be encountered first. This *B-Parameter* is presented in Equation 2.1 and can be used to predict compressor characteristics: for example, a lower *B-parameter* indicates that a rotating stall will precede surge in an axial compressor.

$$B = \frac{N}{2a}\sqrt{\frac{v}{XL}} \tag{2.1}$$

where, N is compressor rotor speed (rpm), a is speed of sound, X is compressor duct area, L is length, and v is Plenum volume.

Greitzer *et al.*'s plenum represents any volume downstream of the compressor including diffuser and combustion chamber. This analysis was used by Bennett *et al.*, who measured the compressor stall characteristics for the *Rolls-Royce* A-250 axial compressor used in the present work. In this compressor rig, the plenum is the vol-

ume of the twin diffuser tubes leading to the combustion chamber. The volume of the A-250 combustion chamber was calculated and used for this calculation by Bennett *et al.* [2]. The maximum value of the *B-parameter* of the A-250 is 1.15. According to Greitzer *et al.* results, a rotating stall will form prior to its development into full compressor stall or surge [2]. In Bennett's research, casing-mounted pressure transducers confirmed the presence of rotating stall cells initiated in the initial compressor stages. It is of paramount interest in this work to see if tubercles are successful in delaying compressor stall, and then how will they affect the calculations and theory presented in Greitzer *et al.*'s work.

2.3   Flow Control

Advancements in understanding of compressor stall behaviour led to a drive to realize stall control. It started when Epstein *et al.* [6], building upon stall and surge research, proposed to prevent the stall disturbances growing beyond some desired limit. They proved that the use of real-time compressor flow data can measure disturbances that can be used to counter a developing stall. It was estimated that a compresssor's stable operating range can be increased by as much as 20%. Figure 2.6, from their work, clearly demonstrates how the normal operating point **A**, can be moved up to a higher pressure ratio point **B**, by employing active stabilizing flow control.

2.3.1   Compressor Flow Control

Two main strategies were simultaneously studied by a range of researchers to prevent compressor stall. First, to detect any stall precursors and secondly, to develop an active system to adjust variable guide vanes or perhaps a bleed valve to return the
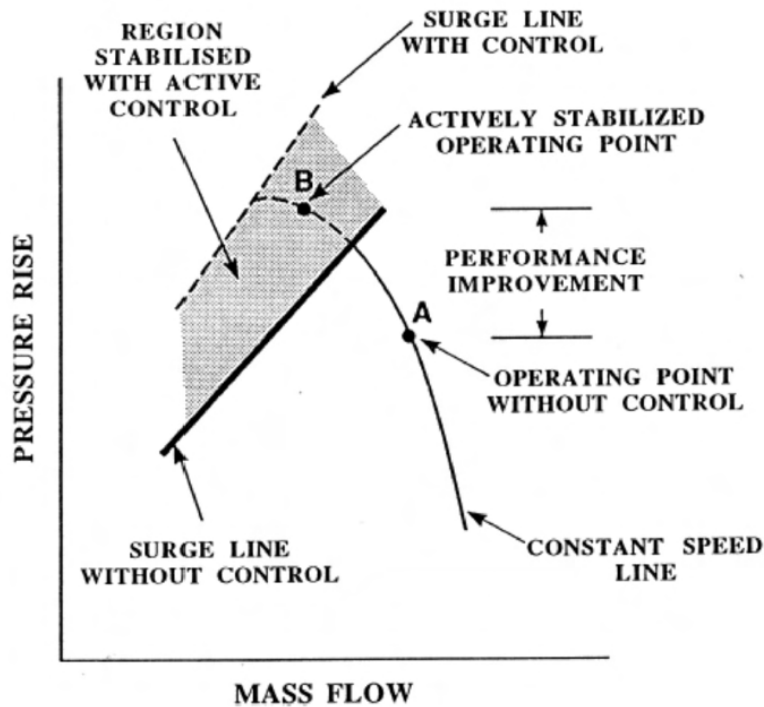
Figure 2.6: Compressor map demonstrating the potential improvements achievable from actively stabilizing flow control [6]

engine to stable operation. The intent was to operate the engine below the surge limit always. This technique, active during the entire engine operation, was used as a stall warning system, and has been widely tested for its application. Ludwig *et al.* [29] were among the first to test their system on a low speed research compressor and also on the J85-GE-5 engine compressor. They used pressure sensors to detect the presence of stall. An internal J85-GE-5 compressor rig with a stock control system was adapted to override the normal operating schedule of compressor bleed valves and variable inlet guide vanes to counter stall and in so doing, control it. The J85-GE-5 compressor shroud was equipped with multiple pressure transducers to analyze

unsteady pressure signals at the compressor case. It was successfully implemented and found to eliminate stall cells rapidly without any compressor damage or engine flame out.

Studies were performed to analyse flow disturbances further, since their identification and status was crucial for the success of any stall warning system, by establishing safety margins and developing stall prevention techniques. Garnier *et al.* [30] experimented with multiple compressors, comparing results with analytical predictions. The experimental data were reported to be in agreement with the Moore and Greitzer Model [28] for qualitative behaviour of the prestall waves and also for the quantitative behaviour of growth rates. These techniques were mainly focused on the disturbances that are part of stall itself. Inoue *et al.* [31] measured pressure at the blade overtip near leading edge and concluded that a loss of periodicity in the pressure measurements indicates the initiation of stall cell precursors. It was reported that as a compressor approaches stall, a highly unsteady region develops near leading edge tip where low momentum fluid accumulates. Data were collected from a single compressor with a small number of low aspect ratio blades. Their study demonstrated the potential of detecting and controlling stall even before one can develop. Other studies were performed focusing on the blade-passing signal and geometric parameters including tip clearance and eccentricity [32]. Tip clearance gaps emerged to be one of the primary factors in improving efficiency and delaying stall inception. These studies were important in understanding flow phenomena and detecting the onset of stall. These studies provided the basis for stall detection using instrumentation and signal manipulation. Compressors were designed with enough stall margin by the manufacturers to provide significant reliability and safe operation so stall detection was not proving to be beneficial for real-time applications. Stall inception detection

never proved to be reliable and efficient enough for its application unless it could be accompanied with a device that could delay stall and surge. This led to the idea of flow control techniques to improve compressor performance.

2.3.1.1 Active Flow Control

With this deeper understanding of compressor stall characteristics, the idea of controlling stall and extending compressor performance range was first presented by Epstein *et al.* [6]. To develop active flow control devices, one first needs the system to detect stall signatures accurately and reliably, and secondly, to suppress flow disturbances actively. Many techniques have been used to control flow by suppressing flow disturbances that precede stall and surge. Paduano *et al.* [33] developed a technique called *wiggling* that individually controlled inlet guide vanes. Modal disturbance wave patterns were measured real-time using a circumferential array of hot wire probes. Initial results indicated mass flow rate improvements of up to 23%. Day [34] conducted a separate study using a series of fast-acting air injection ports in the shroud, just upstream of the rotor. This technique was tested on the same multi-stage compressor on which modal wave disturbances led to a spike-type stall inception. A small amount of air was injected in different sequence using computer-operated valves to damp out modal waves and spike type disturbances. Compressor mass flow rate increased by about 4% and spike-type stall inception was mitigated using local, rather than global, air injection. This led to about 6% improvement in larger stall margin. Furthermore, it was very encouraging that this technique was able to suppress characteristic cyclical pulsing of a compressor in surge. Other flow control ideas focused on suppressing spike type disturbances including synthetic jets, air injection nozzles, and plasma actuation [35–39].

Modal perturbations in a compressor are easier to detect using their circumferential presence. For the modal-type flow disturbances, a wave with multiple harmonics can exist in the full circumference of a compressor annulus. Haynes *et al.* [40] implemented a technique using an array of high-speed, individually-positioned, control vanes that stabilized the first and second harmonics. However, there were no improvements for the third harmonics. This method was not very successful because the introduction of additional circumferential flow variations adversely influenced the stability of compressor. Freeman *et al.* [41], building upon an earlier active stall control, developed a technique for *Rolls-Royce* Viper turbojet engine employing a series of fast-response pressure transducers on the casing. Results indicated significant improvements in the compressor surge margins at full operating range when the bleed air was recirculated to the front stages of the compressor from the middle or rear stages when compared to pure exit bleed.

For potential improvements in the stall margins and compressor performance, very high control system reliability is required. Moreover, it is anticipated that the use of these devices would be increasingly necessary as an engine ages. Active flow control devices also add weight to an engine, reducing overall efficiency of the aircraft and with age, paradoxically, reliability of any active flow control device also degrades, potentially detrimental to engine performance. The benefit and reliabilty of active flow control devices were not significant enough to find their way in to real-life applications.

2.3.1.2   Passive Flow Control

Passive control devices can offer an effective alternative to active systems in compressors. They often involve the modification of stator and rotor blades or the casing

to modify compressor internal aerodynamics, making flow more resistant to stall. Passive flow control devices do not require an external energy source and are inherently reliable and consistent once proven. On the downside, they are always in effect, whether needed or not.

One of the earliest applications of passive flow control was performed by Boyce *et al.* [42] who analytically and experimentally studied the flow influence of radial and circumferential grooves in the overtip casing. It was found that circumferential grooves trapped tip leakage flow and prevented it from mixing with the main compressor flow. Fujita *et al.* among many other researchers, studied a series of configurations of casing treatments on compressors after investigating stall margin improvements demonstrated in their previous study [43–45]. The study demonstrated the potential of circumferential grooves in delaying compressor stall, but also exposed their negative effects on efficiency at design point. Axial grooves showed good potential in improving both stall margin and efficiency at design point when they were constructed at, or less than, blade thickness scale. Fujita *et al.* [43] concluded that stall improvements come with inevitable compromises in efficiency.

Another passive flow control idea is tandem airfoil rotor and stator blades. An early study was completed by Brent while working for Pratt and Whitney in 1972 [46]. This passive flow control technique splits the blade profile into two blades to decelerate the flow using different mechanisms shown in Figure 2.7. The tandem blade design was implemented to increase compressor stage loading and to reduce pressure loss coefficient. Initial results indicated decreased pressure ratio and efficiency [46], but optimization of tandem rotor or stator offers aerodynamic effects and different flow possibilities [47,48]. Tandem blades increase pressure ratio across a single stage as compared to increasing stall margin. Increased single stage PR has

27

potential to considerably reduce length and weight of a multi-stage compressor [49].
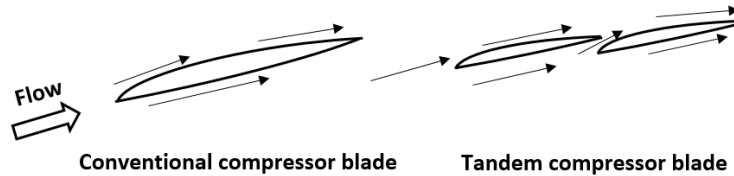
Figure 2.7: Conventional *vs* tandem compressor blade

A bio-inspired geometry called riblets was introduced in early 2000s as a potential means to reduce viscous drag in turbulent boundary layers. It was applied to compressor blade surfaces parallel to blade camber as another promising passive flow control technique [50], that might reduce total pressure loss coefficients by up to 5% for certain configurations and in certain Reynolds number ranges [50]. Riblet location and groove shape have been studied to seek optimal geometries [51]. It was hypothesized that riblets eliminate laminar separation bubbles through earlier transition of a laminar boundary layer [50, 51].

2.3.2 Leading Edge Tubercles

2.3.2.1 Tubercle Background

Stall is a phenomenon encountered by mammals more than aircraft and turbomachines and nature has been responding to the problem for millions of years. Birds, aquatic animals, plants and even trees have encountered and evolved the shape of their bodies and structures to perform their daily routines with maximum efficiency. An exciting observation was made by Fish and Battle [11] in 1995, noticing leading

edge protuberances on the flippers of the humpback whales. These features, also called tubercles, were observed to vary in amplitude (A) and in spacing. Humpback whales are one of the longest and heaviest migrating mammals who perform tight manœvers to catch prey, requiring them to reach high AoA and even stall conditions. Miklosovic *et al.* [52] did an experimental comparison of a tubercled flipper with a non-tubercled flipper using a NACA 0020 baseline airfoil. It was discovered that the airfoil with a tubercled leading edge increased stall angle by 40% and obtained a 6% rise in maximum lift [52]. The tubercled airfoil had a lower drag coefficient with a maximum value 32% less than baseline [52]. It was concluded that humpback whales are able to generate higher lift coefficients, which enhances their mobility in sharp turns.

These studies got the attention of researchers worldwide and the idea of tubercle application was subsequently explored, primarily on airfoils and aircraft wings. Tubercles have been tested on various airfoils including turbomachinery applications at a wide range of Reynolds numbers regularly encountered in real life. Different airfoil profiles have been tested to assess the changing effectiveness of tubercle with wing geometry. Most researchers kept their targeted chord-based Reynolds numbers in the transitional range from 10^5 to 5×10^5 [14, 53–58].

Initial studies from humpback whale flippers were promising and tubercle shape was very well defined, using a sine wave, the amplitude (A) and wavelength (λ) of which were varied to have consistency and simplicity. With variations in tubercle geometry, different flow phenomena have been observed in three regimes: pre-stall, stall and post-stall. The pre-stall regime is defined as the zone at lower angles of attack with a linear lift slope until maximum coefficient of lift or stall angle. The stall regime included regions where angle of attack is high enough to cause the airfoil to

stall. Generally this is when airfoil generates maximum lift. When angle of attack of an airfoil is greater than the stall angle, it is called post-stall regime.

Tubercle research has been reported since the early 2000, but, traces back to 1972 when Soderman [59] performed tests on a serrated wing. A thin strip with serrated edge was attached to leading edge of the airfoil at different locations. A conventional NACA 66-012 airfoil was used as the baseline profile [59]. The study showed that serrations delayed the onset of separation to higher AoA, with consequent increases in maximum lift. Multiple serrated strips with variable gaps between them were tested. It was found that the smallest serrations were most effective in delaying separation when the strip was attached to the pressure surface [59].

After modelling the humpback whale flipper with a NACA 0020 airfoil, Miklosovic and Murray [60] tested the tubercle shape on 2-D airfoil. It was interesting to note that the tubercled 2-D airfoil reduced maximum lift coefficient and overall aerodynamic drag. Drag characteristics of tubercled airfoil were similar to baseline in the pre-stall regime with significant reductions in post stall, due to the attached flow being longer on the suction side. This study was interesting in the fact that tubercled airfoils performed far better than the baseline when applied to modified flippers.

Pre-stall performance characteristics are crucial for airfoil assessment. These lower lift coefficient results were discouraging but research for the optimized tubercle geometry began with different combinations of A and λ being tested. Pre-stall regime results are explained next to understand the extent of work performed and assess the potential of performance improvements in all regimes, including pre-stall.

2.3.2.2   Pre Stall Regime

Johari *et al.* [7] conducted experiments at a Reynolds number based on chord Re_c = 1.83×10^5 on a baseline NACA 63-021 and tubercled airfoil, varying A and λ. The tubercled airfoils produced lower maximum lift coefficients in the pre-stall region, and amplitude rather than wavelength seemed to have a greater effect on lift characteristics [7]. However, they only investigated two wavelengths: 25% and 50% of chord, and both showed decreased lift and stall angle with a further enhancement of similar gradual stall characteristics.

Advancing the understanding of tubercles, Hansen *et al.* [54] experimented with two distinct airfoils NACA 65-021 and NACA-0021 at 1.2×10^5 Reynolds number and compared performance. The airfoils had the same maximum thickness values but the position of maximum thickness was at 30% chord for the NACA-0021 and at 50% for the NACA 65-021. With increased tubercle amplitude, very smooth stall behaviour was observed but it came at the cost of reduced maximum lift coefficient [54]. They also observed the behaviour of tubercled geometries with identical amplitude-to-wavelength ratios and that the airfoil with smallest amplitude and wavelength performed best [54].

A study performed by Peristy *et al.* showed interesting results [1] including the effects of varying tubercle amplitude and wavelength at different Reynolds numbers. It was shown that with increased Re_c, lift coefficient and stall angle were increased for all airfoils [1]. Peristy *et al.* tested three different geometries with amplitudes varying from 3% to 6% and wavelengths from 11% to 21% of the airfoil chord [1]. It was concluded that for a $Re = 3.0 \times 10^5$, tubercles with $A = 3\%$c and $\lambda = 11\%$c generated higher lift at pre-stall angles of attack. From the general performance

31

trends, it was concluded that with increased amplitude-to-wavelength ratios, maximum lift coefficient decreased [1]. However, the amount of suction created by an airfoil increased with amplitude-to-wavelength ratio, an observation also of Zhaoyu *et al.* [61]. Tubercle geometry with $A = 3\%c$ and $\lambda = 11\%c$ generated higher lift coefficients in the pre-stall regions and were characterized by a more gradual stall.

Similarly, in a study by De Paula *et al.* [62] tubercle performance was examined for two different airfoils in a range of Reynolds numbers from 8×10^4 to 2.9×10^5. They used NACA-0012 and NACA-0020 profiles because of their respective difference in maximum thickness of 12% and 20%. Agreeing with other researchers, they noted that tubercle effectiveness was not simply a function of amplitude-to-wavelength ratio, but also on the number of tubercles on the leading edge. In their experiments, two different geometries of approximately the same amplitude-to-wavelength ratio were tested and the one with the largest number of leading edge tubercles (small amplitude and small wavelength) outperformed all others [62]. The lift enhancements of the tubercles also trended with Reynolds number: As it increased, the lift generated by tubercle-modified airfoils improved over that of the baseline [62]. Consistent with others, the amplitude:wavelength ratio of 3:11% chord out-performed the others. Tubercles with $A = 3\%c$ performed best in terms of lift coefficient and gradual stall for both airfoils tested by Peristy *et al.* and De Paula *et al.* [1, 62].

These studies showed promising tubercle results in the pre-stall regime but it must be reiterated that a majority of tubercle studies in this regime have also showed performance degradations. Clearly a tubercle optimization is required to explore the full potential of tubercles both in terms of performance enhancement and in the mitigation of performance loss.

2.3.2.3 Post Stall Regime

Post stall regime is the part where tubercles really become interesting. They have been shown to promote delayed and more gradual stall characteristics in many different studies. For instance, Miklosovic *et al.* [60] observed that the stall of a tubercled airfoil was attractive, since it happened in a stepwise manner, and higher post-stall lift was observed. In fact, a 50% increase in lift in the post-stall regime over the baseline was quantified by Johari *et al.* [7,60]. From the experiments performed by Johari *et al.*, there exists a possibility that, with further optimization of tubercle amplitude and wavelength, the same or better lift characteristics can be achieved while increasing stall angle, and reducing lift penalties in pre-stall regions [7]. This is consistent with Rostamzadeh *et al.*'s [63] work, that showed higher lift in the post-stall region for tubercled airfoils over the baseline airfoil. Peristy *et al.*'s experiments showed that tubercled airfoils stalled at a lower angle of attack; stall was more gradual and the tubercled airfoil was able to generate the same reference lift even after stalling, and significantly more in the post-stall regime. Research has demonstrated that most tubercle shapes result in lower stall angles, but stall is usually more gradual. Tubercled airfoils perform significantly better in the post-stall regime than their respective unmodified profiles do. Optimization of tubercle shape is required, since significantly better pre-and post-stall characteristics are achieveable [1,16,62,64].

2.3.2.4 Tubercle Flow Control Theories

Many flow visualization and numerical simulation attempts have been made to understand the flow phenomenon introduced by tubercles. It is broadly accepted that tubercle pairs generate Stream-Wise Counter Rotating Vortices (SWCRV) on the down-

stream suction surface, resulting in delayed boundary layer separation. While tubercles were initially compared to vortex generators, with the introduction of SWCRV theory, Van Nierop *et al.* [65] argued that this is not appropriate because of tubercle's relatively large size compared to the boundary layer. However, another hypothesis holds that tubercles alter the pressure distribution on the suction side of airfoil making it favourable downstream of the peaks leading to a delayed stall [65].

Initial tubercle simulations were focused on tubercle performance contributions to different airfoils. To understand better the flow phenomenon, Pedro *et al.* [66] and other researchers conducted numerical studies on the flow over a model whale flipper and on airfoils at a range of Reynolds numbers varying from 1.5×10^4 to 5×10^5. Their findings supported conclusions that tubercles generate vortices that delay separation on the suction surface [66, 67]. The presence of span-wise flow on the suction surface of test airfoils was also observed by Dropkin *et al.*, with low pressure regions found downstream of tubercle troughs [67]. Tubercled airfoil lift also remained higher in the post-stall regions as compared to the baseline results.

Regardless, it remains widely believed that tubercles behave like vortex generators so it is relevant to discuss how vortex generators (VG) work. Normally, VG are defined on the basis of their height being on the order of boundary layer thickness, where they enhance the mixing of free stream, higher momentum flow from outside the boundary layer, increasing the latter's resistance to an adverse pressure gradient, and its likelihood of remaining attached to the surface. VG effectiveness relies on the strength of vortices generated and their decay rate downstream of the devices. VG spacing was found to be equally critical just as chord-wise position is important. In the literature survey by Lin [68], it was concluded that for VG, it is crucial to have an appropriate gap between two adjacent VGs. The close proximity to adjacent SWCRV

34

leads to mutual interference between adjacent vortices, reducing their effectiveness. Moreover, for a sub-boundary layer, vortex strength decreases because of wall shear stress for VG with heights on the order of 10-50% of boundary layer thickness [68]. Ashill *et al.* [69] gave a relation for the rate of decay of vortex circulation, however it will not be applicable for tubercles because of their height above the boundary layer. The key difference is that tubercles generate vortices that extend well outside the boundary layer while VGs generate them inside the boundary layer.

Many other studies used flow visualization to analyse the flow phenomenon introduced by tubercles. Johari *et al.* [7] and Camara *et al.* [70], observed bi-periodic tubercle behaviour from tuft visualization for a modified airfoil with 50%c wavelength and 5%c tubercle amplitude. The phenomenon can be observed in Figure 2.8 where the apparent stall has been compartmentalized bi-periodically: that is to say, repeating un-stalled regions bounded by stalled regions along the span. This figure also reveals span-wise flow downstream of the tubercles. Detached eddy simulation conducted by Camara *et al.* also predicted bi-periodic flow, supporting experimental results [70]. However, this behavior was not observed for all tubercled geometries. Bi-periodicity can be a major contributing factor in preventing span-wise stall propagation.

Numerical analyses performed by Rostamzadeh *et al.* [63] revealed that flow moving over an airfoil generates a low pressure zone downstream of tubercle valleys. The flow downstream of the peaks converges towards this low pressure zone, creating separation bubbles downstream of valleys. Rostamzadeh *et al.* noticed that tubercled geometries with large amplitude and small wavelength produced higher suction downstream of the tubercle troughs, as compared to downstream of peak regions close to the leading edge, resulting in spanwise periodic pressure gradients.
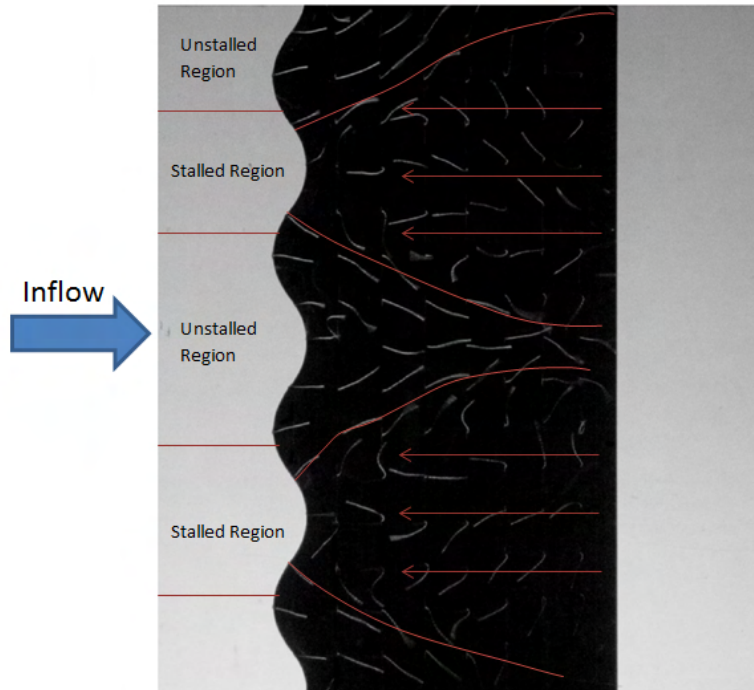
Figure 2.8: Custodio *et al.*'s Tuft visualization of a biperiodicity on a tubercled airfoil at 18 degrees AoA (Modified from [7])

However, airfoils with tubercles of smaller amplitude (on the order of 10%c) created more suction along the peaks and at the mean cross-sections. Nonetheless unmodified airfoils for all profiles tested created the most suction in the pre-stall regime, and generated the most lift [63]. The results from this study were different from the bi-periodicity characteristics observed in other studies.

In 2015 Bolzon *et al.* tried to relate and to compare all published theories to reach a conclusion regarding the contribution of tubercles [56]. It is certain from their analysis that tubercles generate pairs of SWCRV however, the most prominent driving mechanism behind tubercle performance is debatable: either vortex gener-

ators result in boundary layer attachment or vortex lift generators [56]. Vortex lift generator mechanism is when tubercles perform more like delta wing by creating low pressure zones using SWCRV. They observed that an increase in tubercle amplitude leads to the commonly observed decreased maximum lift in the pre-stall region. However that might be an effect of earlier stalled regions along the tubercle troughs, due to higher leading edge curvature in tubercle valleys. Vortices migrating towards the trough regions led to contractions of stalled regions.

Nor can tubercles be compared to delta-wings because the presence of such a wing's long leading edge generates two very strong, wing-scale vortices that create low-pressure zones over the upper surfaces of the wing, while tubercles generate a series of SWCRV just larger than boundary layer scale [56]. For tubercles, SWCRV are significantly weaker than those of delta wings and the effect of their interference with each other is unclear. Rostamzadeh *et al.* explained that the flow phenomenon can be even more complex because of potential lateral flows caused by span-wise pressure gradients along tubercle troughs and peaks.

Using particle image velocimetry (PIV), Wei *et al.* [61] observed a pair of SWCRV being generated by each tubercle converging downstream of the trough regions with intensity decreasing steadily as they progressed downstream. With increases in tubercle size, the SWCRV ultimately cancelled each other out [61]. The reason for the reduced intensity was suspected to be their spanwise migration towards the troughs, causing them to interact, so viscous dissipation reduced their vortical momentum. They concluded that a higher value of amplitude-to-wavelength ratio resulted in better control of flow separation [61].

Protuberance effectiveness at a low Reynolds number of 5×10^4 was also measured using PIV by Zhang *et al.* [53]. The main highlight was the flow behavior

37

description along the trough regions, further to the evidence of SWCRV. They observed contours of normalized stream-wise vorticity in the troughs, and formation of a laminar separation bubble earlier than the baseline. Flow over the suction surface of tubercled airfoil finally separated closer to the trailing edge [53].

Oil flow visualization used by De Paula *et al.* [62] showed laminar separation bubbles forming along the troughs on all tubercled airfoils. They moved upstream along the troughs even at small angles of attack, supporting the simulation results of Rostamzadeh *et al.* [63]. It was concluded by De Paula *et al.* that tubercle behaviour differs for different geometries and flow conditions, and similar tubercle geometries behave differently for airfoils of different thicknesses. Even the formation of the delta-shaped separation region explained by Rostamzadeh *et al.* was seen to grow upstream towards the leading edge as airfoil angle of incidence was increased [62]. In short, flow behaviour was unique to airfoil geometry [62]. Flow compartmentalization, where tubercles act as fences on the wing, was proposed by Fish *et al.* and supported by Cai *et al.* as they tested a modified airfoil with only one tubercle [71]. The presence of one tubercle made stall occur in two steps: one before the stall angle of baseline airfoil with the second side remaining un-stalled longer, or until a higher angle of incidence than the stall angle of baseline stall [71]. It was observed that even after the modified airfoil stalled, there remained a region close to the leading edge on the tubercle where flow was still attached, contributing some post-stall lift [71].

Most tubercle studies randomly selected tubercle shape based on the individual literature survey. Levert-Beaulieu *et al.* were one of the first teams to perform tubercle shape optimization allowing geometry to depart from sine waves, and exploring power functions. They used a gradient-based optimizer to get a most effective tubercle shape on a NACA-0012 airfoil at zero angle of incidence in transonic flows [72].

Tubercle curvature was found to be of significant importance, because some significant drag reduction was observed with the reduction in power function to 0.2 from 0.75, ultimately resulting in an increasingly triangular tubercle shape [72]. It is suspected that the power function of 0.2 led to the formation of a narrow channel of flow accelerating along the tubercle trough region, creating a span-wise pressure gradient leading to lateral flows along span and in their particular transonic flow conditions resulting in a weaker shock structure [72].

Tubercles have not been tested just on the 2-D airfoils or wings, they have been applied to other real applications like swept wing and UAV wings. The tubercle effect on the swept wing of an aircraft was tested by the Bolzon et $al.$ using hydrogen bubbles in a water tunnel for flow visualization at $Re = 2.2 \times 10^5$ [73]. They clearly observed wing tip vortices on a conventional swept wing, but tubercles were able to suppress these vortices, while decreasing the induced drag [73]. For compressor applications, wing tip vortices are essentially tip leakage that contributes to losses but worse, they are one of the major contributing factors to stall propagation in a compressor stage. It is believed that tubercles used on compressor blades have the potential to resist tip leakage flows, and thereby increase the stall limits of an axial compressor. Tubercles on a swept UAV wing were tested at Reynolds numbers of 1.8×10^5 and 2.7×10^5 by Sudhakar et $al.$ [74]. In their work, wings with tubercle showed significant improvements in lift and stall angle, but only at the lower Reynolds number tested. At higher values the modified profiles under-performed when compared to the baseline. Sudhakar et $al.$ also concluded that tubercles led to much more stable flight of their UAV, a feature that can be beneficial in case of wind gusts. This is not restricted in any way to UAVs: in fact compressors or fans in gas turbine engines face similar unsteadiness at a range of operating conditions [74].

2.3.2.5 Tubercle Application in Turbomachinery

The idea of applying tubercles to the leading edges of a turbomachinery component, in this case an axial fan or compressor, was first presented by Corsini *et al.* [13] in 2013 when they performed a simulation on a NACA-0015 airfoil. While the relation between individual blade performance and full compressor performance is not made, the delayed stall characteristics of tubercled airfoils is attractive in terms of compressor performance. Their simulation revealed the presence of delta-shaped recirculation zones at trailing edges downstream of the tubercle valleys [13].

Weber *et al.* [15] tested tubercles on boat rudders, specifically focusing on those susceptible to cavitation. The elimination of which would reduce hammer-like impact loads caused by the collapse of suction side separation bubbles. It was observed that a tubercled rudder profile accelerates the onset of cavitation that occurs in tubercle vallies. Tubercle application to propeller blades was tested for the first time by Asghar *et al.* [12] on a widely-used drone propeller blade profile. Flow control on drone blades has great potential, because propeller efficiencies are known to be as low as 40% [12]. In their work, the propeller leading edge was divided into three different regions: hub, mid-span and tip. Tubercles, when used in the mid span and tip sections, resulted in a considerable increase in efficiency that was calculated based on the coefficients of power and thrust [12].

Most tubercle studies have been conducted on Reynolds numbers based on airfoil chord and in flows where Mach number is less than 0.3. Bouchard *et al.* [14] tested tubercles on transonic cascade vanes leading edges at $Re_c = 3.5 \times 10^5$. Their results showed small reductions in total pressure loss for tubercled vanes when compared with the baseline, but a narrowed wake at the cascade exit was also observed [14].

Keerthi *et al.* evaluated the effect of tubercles on total pressure loss, stall angle and flow deflection on compressor blades in a cascade [16]. Tubercles with the lowest amplitude and amplitude-to-wavelength ratio outperformed all the other geometries tested, resulting in a 43% increase in stall angle from 6° to 8.6° [16].

2.4 The Self-Organising Maps

Self-Organizing Map (SOM) is a type of neural network technique that reduces the dimensionality of input data to simplify comprehensive output. SOM is an unsupervised learning algorithm that does not employ the error correction learning of conventional artificial neural networks. It was introduced in the 1980s by Kohonen [75].

2.4.1 SOM Principles

SOM operates in two phases; training and mapping. Following the typical neural network technique, the training phase handles multi-dimensional input data sets and lays them out in a 2-D form. In the training phase, a network of neurons is created and weights are attached to each neuron. In the mapping phase, a map space consisting of nodes and neurons is created using training data to represent inter relationships. As an output, the SOM produces 2-D training samples called a *map*, that makes establishing links between multiple variables. At this point a generalized map is generated that does not represent any particular space. An existing data set is required to train this map to represent the data set where its size plays significant role in accuracy.

The SOM process uses two layers of neurons: an input layer and an output layer. The latter is usually arranged in 2-D hexagonal or rectangular grid. Weight vectors

of input layer dimensionality are assigned to each neuron in the output layer. Weight vectors are selected randomly using one of two processes: either selecting small random values or spanned uniformly across the two largest input vectors. Unsupervised training of the output layer uses a technique called *competitive learning* that has three steps: *competition*, *cooperation* and *adaptation*.

In the competition phase, the distance (d) between each neuron weight vector and the input space point is calculated using the Euclidian distance relation given in Equation 2.2.

$$d_j(x) = \sum_{k \in K} (x_k - m_{jk})^2 \tag{2.2}$$

where x is the datum, K is the number of training data set variables, j is the number of neurons and m is the weight vector of neurons.

The closest neuron to the selected input variable wins the competition and becomes the *Best Matching Unit* (BMU). In the cooperation step, the neuron closest to the BMU is selected. The neurons are moved using a method called *lateral interaction effect* (LIE) that depends on the distance of the neighbour neurons to the BMU. This can also be dependent on a time function between the BMU and other neurons. The BMU therefore, has a circle of influence that diminishes with radius, as shown in Figure 2.9.

Cooperation is primarily concerned with the selection of neighboring neurons. In the adaptation step, after finding the lateral interaction effect, individual weights (m) of every neuron are calculated using Equation 2.3. The influence of the BMU on neighbouring neurons is calculated using the LIE factor.
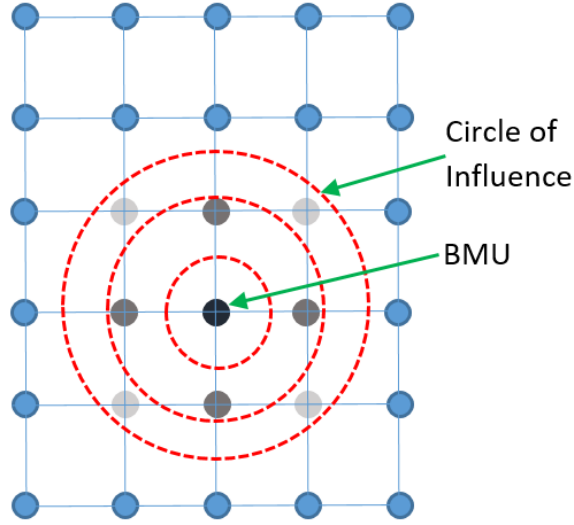
Figure 2.9: Demonstration of a BMU circle of influence

$$\Delta m_{j,i} = \eta(t) \cdot T_{j,I(x)}(t) \cdot (x_i - m_{j,i}) \qquad (2.3)$$

where, $m_{j,i}$ is the weight for a specific neuron, $\eta(t)$ is the learning rate, updated on every iteration (t), defined by Equation 2.4. $T_{j,I(x)}$ represents the lateral interaction effect (LIE) factor, defined by Equation 2.5.

$$\eta(t) = \eta_0 \, exp(-t/\tau_\eta) \qquad (2.4)$$

$$T_{j,I(x)} = exp(-S_{j,I(x)}^2/2\sigma^2) \qquad (2.5)$$

where S is the lateral distance between neuron j, $I(x)$ is the BMU neuron and σ represents the size of the neighbourhood, which is expected to decrease with increased

iterations.

Figure 2.9 demonstrates a mesh of neurons. After the distance calculation, these neurons move towards the input point **X**, shown by the movement and dashed lines in Figure 2.10. It can be shown that the darker neuron, the *BMU*, gets quite close to the input point. The movement of other neurons (light grey) is restricted.
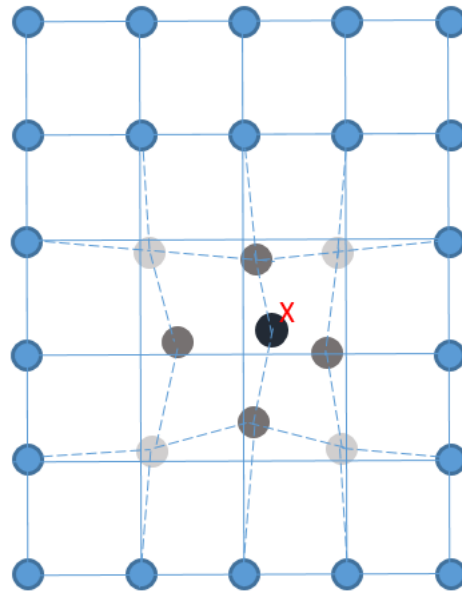
Figure 2.10: Demonstration of a BMU iteration step

Multiple iterations of these steps are performed to converge the output map to a solution. At each iteration, learning rate is assessed to adjust weights accurately. After performing sufficient iterations, the learning rate converges to zero, indicating analysis output.

SOM has been used for a range of applications, such as when Miljkovic [76]

detected faults on aircraft piston engine by visualizing different parameters. It was concluded that the data from the engine test could be used to identify an engine parameter space for the identification of normal engine operation and by extension, faulty engine operation [76]. Another interesting SOM study was performed by Rai *et al.* [77] when they used SOM to predict the remaining useful life and deterioration of roller bearings. They used the time and frequency domain of vibration data to effectively employ SOM for calculating bearing health index. Results indicated the efficient tracking of bearing useful life [77].

This chapter explained the basics of flow mechanics, internal aerodynamics of axial compressors and the tubercle effect on airfoils. This was crucial for the understanding of work performed here and the results obtained in the process, especially the understanding of tubercles' influence on boundary layer separation and airfoil stall. The basic understanding of tubercle theories proposed by researchers is crucial to understand the results of their testing on axial compressor at design conditions. With a basic understanding of SOM, it will be easier to understand why different steps have been performed in the methodology in order to conduct SOM analysis. This, along with subsequent experimental technique methodology, will be described next.

3 Methodology

This chapter commence with the introduction of new tubercle geometric and performance parameters which are essential to understand the tubercle performance. Tubercle optimization was performed using SOM maps. The data set for the analysis was extracted from various published research studies. Data extraction processes and parameter normalization has been explained in section 3.2. New tubercle geometries were selected to expand SOM analysis and tested in the wind tunnel. Experimental set-up for low speed testing of new tubercle shapes are explained next. A set of tubercle shapes were selected for compressor cascade testing. The design and setup of compressor linear cascade with the different measurement techniques employed are detailed in the second part of this chapter. Final part of this chapter explains the A-250 compressor rig setup and instrumentation system designed to measure performance of tubercles in 3-D rotating compressor application.

3.1 Tubercle Optimization

The neural network based method of SOM has been widely used by researchers for a range of different applications. This is possible due to their open-source code being available in *Matlab* and *Python*. SOM *Matlab* toolbox [8] (*MATLAB* SOM) explains the procedure and technique in detail. The data was imported into the *Matlab* code

in a specific format. In the output format, each variable is identified using an hexagonal cell with a legend on the right side. During the SOM process, all the variables were converted to standard values for comparison with each other. After comparison these values are restored to actual numbers for the better understanding of the variable comparison and estimation. Figure 3.1 is an example of an output taken from *MATLAB* SOM, modified for the demonstration purposes. The U-matrix on top-left provides information on the overall neural structure. This is used to assess data density, where darker regions indicate smaller neuron distances. Recall that neuron distance indicates that U-matrix can be used to differentiate data sets and to estimate the location of greater data densities for deeper analysis.
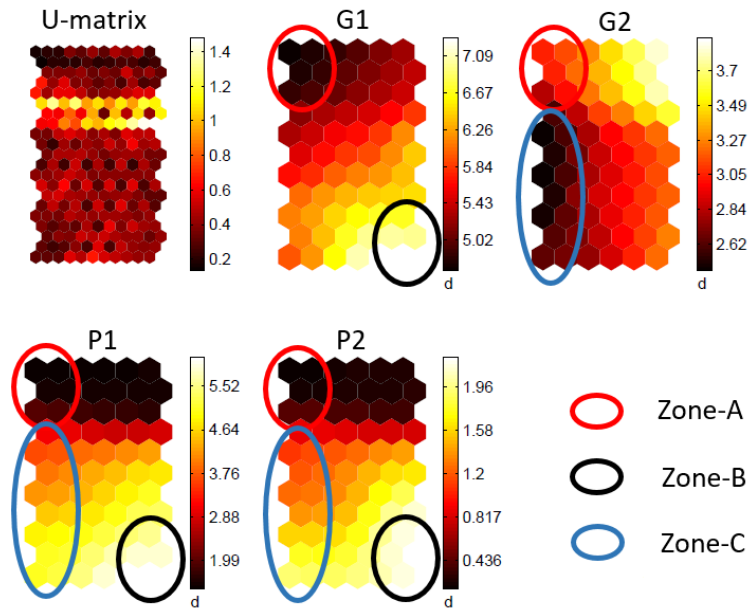
Figure 3.1: Demonstration of SOM. Modified from [8]

In Figure 3.1 G1 and G2 are two geometric variables while P1 and P2 are performance parameters. The legend on the right side of the hexagonal mesh indicates that the values decrease from bright yellow to red. Thus geometric parameters can be compared to performance parameters, based on the colour coding that essentially indicates the variable values. G1 values are lower in Zone A, where P1 and P2 also have lower values. This indicates that the lower G1 values result in lower P1 and P2 values. Another similarity between G1, P1 and P2 is apparant in Zone B that higher G1 values correspond to higher P1 and P2 values, indicating another trend. This was the case when one variable's similarities can be observed. G2 does not seem to correlate with P1 and P2, nor G1, but some sections can still be compared. The upper right corner represents higher values of G2 and in the same sections, lower values of P1 and P2 are observed. G2 has dark red region in the lower left portion of the grid (Zone C) but P1 and P2 change too much in this region to draw any conclusions or G2 is not correlated with P1 and P2.

3.1.1   Novel Parameters and Data Extraction

SOM technique has been explained in the previous chapter. A data set required to train the neurons was collected from various studies. During the literature review, it was determined that to understand the 3-D effects introduced by tubercles, new geometric and performance parameters were required. Tubercle geometric and performance data varied across different studies and reverse engineering was required to extract all geometric parameters. Data extraction and normalization section explains the procedure to extract data and the normalization performed to compare results from different studies.

3.1.1.1 Novel Geometric Parameters

Tubercles have been widely tested using the two 2-D parameters: amplitude (A) and wavelength (λ). However, it is not possible to predict the 3-D tubercle effects on performance using only 2-D parameters. Studies have revealed no concrete conclusion on exactly which tubercle characteristics positively influence airfoil performance, but it is established that their associated SWCRV are known to be key contributors. To better understand the 3-D effects of tubercles, two new tubercle geometric parameters were introduced in this work. Tubercle shape, viewed from the upstream flow, was considered significant due to its 3-D nature and possible effects on the generation of SWCRV. To incorporate different flow conditions, airfoil sizes and the upstream view of the tubercle shape into the analysis, a Reynolds number based on the hydraulic diameter (Re_{Dh}) was introduced. Next, to analyze the effects of tubercle shape as seen from oncoming fluid perspective, tubercle aspect ratio ($\!R$) was measured for each tubercle shape.

To develop $\!R$ and Re_{Dh} parameters, a tubercle was sectioned at mid-amplitude position as shown in Figure 3.3(b). This shape was elliptical in nature and its major and minor semi-axes were measured, denoted as a and b respectively as shown in Figure 3.3(c). The 2-D view of the tubercle and its sectioning is shown in Figure 3.3. The tubercle shape cross-section aspect ratio ($\!R$) is the ratio of axis parallel to the leading edge (a) to the axis perpendicular to leading edge (b) of ellipse as stated in Equation 3.1. The hydraulic diameter of the ellipse was calculated using Equations 3.2. Similarly, Re_{Dh} is another 3-D parameter proposed to be the better alternative than Re_c to compare tubercle performance parameters. Re_{Dh} was calculated using the

49
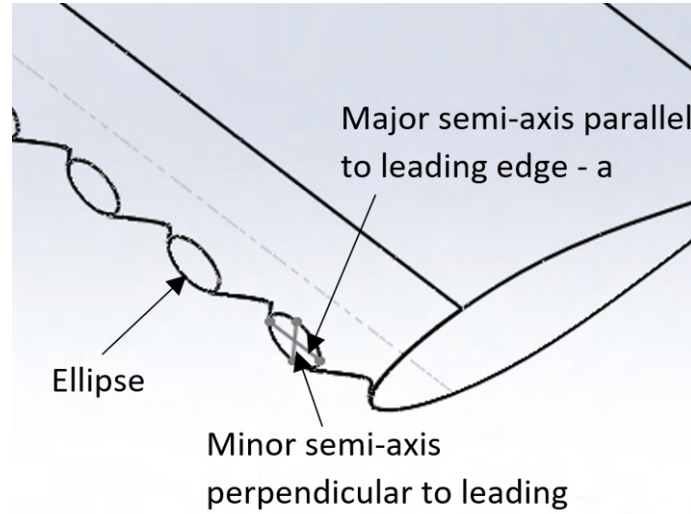
Figure 3.2: 3-D tubercled wing, truncated at the mid-amplitude position of the tubercles
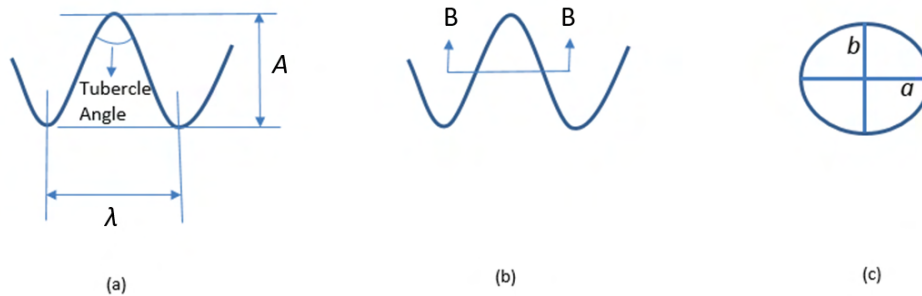
Figure 3.3: (a) Tubercle representation with 2-D sine wave, (b) Representative tubercle sectioning, (c) Section B-B of tubercle with major axis a, and minor axis b

hydraulic diameter instead of the chord length using Equation 3.4.

$$\mathit{R} = \frac{a}{b} \qquad (3.1)$$

$$D_h = \frac{4A}{P} = \frac{4ab(64 - 16e^2)}{(a+b)(64 - 3e^4)}, \tag{3.2}$$

where, A is the area of the ellipse, P is the perimeter of ellipse and

$$e = \frac{a - b}{a + b} \tag{3.3}$$

$$Re_{Dh} = \frac{\rho V D_h}{\mu} \tag{3.4}$$

Since pressure gradient due to the leading edge geometry was more representative of 3-D flow than profile chord, Re_{Dh} was considered due to its strong influence on flow separation and nature of SWCRV generated. These two parameters can change the strength of vortices generated which influence the contribution of the tubercles on stall and lift characteristics. A tubercle AR greater than unity meant that the ellipse section's major axis 'a' aligned with the leading edge and its sharper radii on either side increase the chances of abrupt flow separation since it acts more like delta wing. On the other hand, a tubercle AR less than unity results in a more gentle flow separation and possibly weaker SWCRV since the minor axis (a) is now aligned with the leading edge line.

3.1.1.2 Novel Performance Parameters

While performance is governed by tubercle shape, tubercles themselves have demonstrated potential in improving maximum coefficient of lift ($C_{l,max}$) and stall angle (α_s) performance. Tubercles often lead to gentle stall characteristics and provide significant improved lift in the post-stall regime. The α_s and $C_{l,max}$ characteristics of tubercled wing and airfoils have been widely studied, but a quantitative comparison

of their post-stall regime effects have never been analyzed. This can be observed in Figure 3.4 from Johari et al. [7], where baseline airfoil performance is compared with two different tubercled airfoils. Baseline airfoil stalled at an AoA of about 21° where the tubercled airfoils stalled at 13 and 15°. From a α_s perspective of the performance, tubercles reduced airfoil performance and were not able to reach $C_{l,max}$ of the baseline. But the tubercled airfoil stall was much more gentle. Comparing the performance of the tubercled airfoil at angles greater than α_s, it can be clearly observed that there are significant lift improvements in the airfoil post-stall regime, shown as shaded region in Figure 3.4. The size of the shaded region qualifies the post-stall operational improvement. This will be called *Post-stall area* in this work.
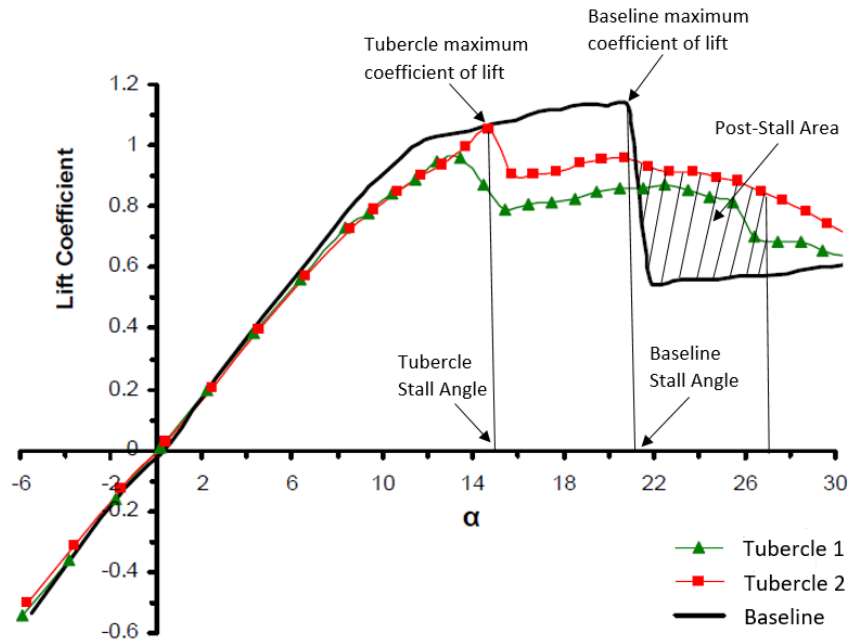
Figure 3.4: Tubercle performance characterization parameters. Data modified from [7]

To quantify these data, it was important to standardize this newly introduced post-stall area parameter. The experimental data collected for this work varied in terms of maximum α that was tested. In an attempt to normalize this parameter, the post-stall area was calculated starting from baseline α_s, extending 6 ° into the post-stall regime. Six degrees was chosen arbitrarily, to ensure the area can be calculated for all data sets.

3.1.1.3 Data Extraction

SOM require data to train its neural network, the effectiveness of SOM results depend on the size of the training data set. For the present work, this data set required geometric and performance parameters to be comparable. Insufficient data sets were available from this lab, but tubercle experiments have been done on airfoils used in other applications such as compressor blades or turbines. It was decided to collect any published experimental data for any range of tubercles. Coefficient of lift *vs* AoA curves are normally used for different tubercle applications to determine the effects of tubercles on airfoil performance. SOM presented an opportunity to combine all published experimental data sets in order to optimize tubercle geometry.

For the experimental work, researchers performed testing on different airfoils and flow conditions. A significant data set was provided by five research groups. Data sets including the airfoil profiles shown in Table 3.1 were combined. *Solidworks* was used to create 3-D CAD models of each airfoil, a necessity for the extraction of geometric parameters that were newly introduced in Section 3.1.1 (Re_{Dh} and R). A standard extraction procedure of sectioning tubercled airfoil at the mid-amplitude sine wave location was used. The various sizes and shapes of tubercles varied the R significantly from 1 to 4. Performance parameters like $C_{l,max}$ and α_s were recorded

by digitizing plots using open-source software. The experimental data sets used for this study are listed in Table 3.1 with their geometric parameters.

Table 3.1: Data used for the SOM analysis

Authors	Airfoil	A [%c]	λ [%c]	Re_c	c [mm]
Hansen *et al.* [54]	NACA-65-021 and NACA-0021	3, 6 and 11	11, 21, 43 and 86	1.2×10^5	70
Johari *et al.* [7]	NACA 63$_4$-021	5, 10 and 12	25 and 50	1.8×10^5	102
de Paula *et al.* [62, 64]	NACA-0012, 0020 and 0030	6, 10 and 12	11 and 40	5×10^4 8×10^4 1.2×10^5 2.0×10^5 2.9×10^5	150
Peristy *et al.* [1]	NACA-0018	6, 10 and 12	11, 13 and 21	7.5×10^4 1.5×10^5 3.0×10^5	152.4
Huang *et al.* [78]	SD8000	3 and 17	6.5 and 15	1.0×10^5	150

3.1.1.4   Data Normalization

Generally, experimental tubercle shapes seem to have been selected randomly by researchers and few attempts have been made to optimize tubercle shape. Levert-Beaulieu *et al.* [72] however, used a gradient-based optimizer to modify tubercle shape on a thin symmetric airfoil in the transonic flow regime at zero angle of attack. Tubercle shapes based on sine waves with A and λ as geometric parameters were tested and the outcome raised the possibility of an unconventional tubercle shape based on power series curves. Initial attempts for the tubercle study using sine waves to roughly identify the optimized shape led to performance improvements. The power series tubercles also performed well, however, that study was limited to the transonic regime and only one data set was generated that looked promising. Tubercle optimization combining all the experimental results was needed.

Experimental results from different studies had varying airfoil profiles, chords, *Re*, Mach numbers, etc. therefore, to generate a combined data set, parameter normalization was essential. Amplitude and λ were traditionally normalized using airfoil chord. The *A* definition varied among studies: for this work, full amplitude was standardized, measured from the peak to valley of the tubercle. Re_{Dh} and $\cancel{R}$ needed to be extracted but due to their non-dimensional status, no normalization was needed.

The $C_{l,max}$ and α_s of all tubercled airfoils were normalized based on their respective baseline airfoils. Post-stall operability area was already defined with relation to the baseline airfoil performance, so there was no further normalization needed for this parameter.

3.1.2 Experimental Setup and Procedures for Tubercle Selection

3.1.2.1 Airfoil Geometry Selection

From a SOM output map, trends were observed, but there exist tubercle geometric parameter regions that have never been tested. An attempt was made to explore these unknown territories to expand the existing data set. The work of Peristy *et al.* [1] was selected to expand upon the training data set from their best performing geometries that were also an example of a randomly selected geometry. A new tubercle geometry was selected based on results from SOM analysis: A2L7 with *A* and λ of 4 and 7%c respectively. A2L7 tubercled airfoil was tested in low speed wind tunnel. Experimental results of A2L7 were compared with the baseline geometry and those of A3L11, since that was the best performing tubercle geometry from Peristy *et al.*'s [1] work. Another tubercle geometry was subsequently selected: The tubercle λ was increased from 7%c to 9%c, increasing the distance between tubercle peaks. These

Table 3.2: Peristy *et al.* [1] (NACA-0018) airfoils (A3L21, A5L13 and A3L11) with the new tubercle geometries (A2L7 and A2L9) at $V_a = 7.5$ m/s.

Re_{Dh}	A [%c]	λ [%c]
6560	6	21
5074	5	13
4206	3	11
3370	2	7
3970	2	9

newly introduced tubercle geometric parameters are shown in Table 3.2.

3.1.2.2 Airfoil Fabrication

Expansion of tubercle geometries from Peristy *et al.*'s work dictated the use of NACA-0018 airfoil for experimental testing. They had selected the NACA-0018 airfoil due to its wide application on wind turbines and small UAV aerial vehicles. The chord length of the airfoil was 6 inches and span was 18 inches. Due to the excessive span of the wing, it was constructed in five small sections. The central span section was instrumented with pressure taps on both pressure and suction sides. The manufacturing details of the wing section are provided in reference [1]. Metal hypodermic tubes were inserted into the pressure taps and long plastic tubes (*Tygon*) were fitted on the metal tubes and to the instrumentation.

3.1.2.3 Experimental Setup

A subsonic, closed-circuit wind tunnel was used for experimental tubercle optimization testing in the Department of Mechanical and Aerospace Engineering, Royal Military College of Canada. The test section measured at 42 inches wide by 32 inches high. The wing section was enclosed using endplates to simulate an infinite wing and an AoA of 30° was the maximum α tested during this experimental campaign.

56

Flow conditions were measured using a Pitot tube about four chord lengths upstream of the wing leading edge. A *Scanivalve MPS4264*, 64-channel miniature pressure scanner was used to measure all the 64 pressure taps on suction and pressure surfaces of the test models. The pressure measurements were performed along the valley and peak of the central tubercle to analyse thoroughly the tubercle performance, as shown in Figure 3.5. Results only included the averaged coefficient of lift. Maximum uncertainity of the *Scanivalve* measurements was 0.06% full scale for each pressure port. Once the wind tunnel settings were made, the wing was rotated using a disc at the base of the wind tunnel section to change α in the increments of $0.1°$ using an protractor on the mounting plate. The α of the blade was varied from 0 to $30°$ with small increments in the critical stall regions to determine the α_s accurately. From earlier experiences, a water manometer was also used to monitor previously observed dynamic effects of tubercles near α_s.
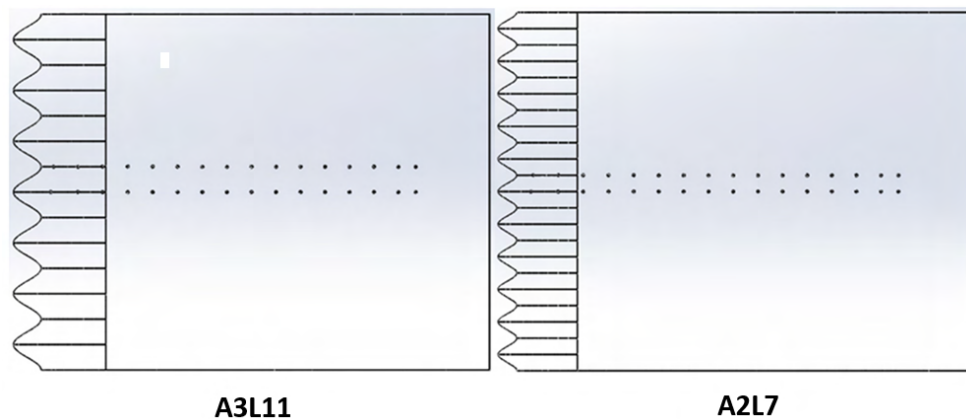
Figure 3.5: Suction surface plan view of NACA-0018 test airfoils showing two streamwise sets of pressure taps

3.1.2.4 Flow Visualization Setup

Oil flow visualization was performed on the mid-section of the wing to analyse flow affected by the tubercles at α of $15°$ and the intermediate Re_c of 1.5×10^5 for two airfoils: A3L11 and A2L9. This allowed analysis of performance differences between best performing and new geometries. A equal mixture of isopropyl and *Aeroshell* aviation oil was used as a visualizing medium. The purpose of alcohol is to reduce the viscosity of the oil, enhancing its interaction with the flow. A pneumatic spray gun was used to spray the mixture evenly on the suction surface of the wing. The volatility of alcohol also ensured that the oil initially moved generally chordwise with the flow, and then set when flow stability was achieved. A very thin layer of oil could be deposited on the surface by adjusting jet pressure.

To ensure that the oil mixture did not interact with the low speed flow when the wind tunnel was accelerating to test speeds, the oil was applied with the wing at α=$45°$. Test procedure had the wind tunnel quickly initiated and when the desired flow conditions were reached, the airfoil was gently set at the desired α. The wing surface was observed using a blacklight (UV-A) lamp with $\lambda = 450$ *nm* to take advantage of the fluorescence of the aviation oil. A high resolution camera was used to video the wing during the transition process between $\alpha = 45°$ and $15°$. The effects of gravity were minimized by the thin layer of fluid. This technique was used primarily to highlight separated regions, since oil will accumulate there.

3.2 Compressor Cascade Testing

3.2.1 Wind Tunnel and Experimental Setup

For compressor casacade testing, RMC's transient transonic wind tunnel was used [1]. A photograph of the test facility is shown in Figure 3.6. This in-draft, short-duration wind tunnel is capable of reaching Mach 4.0 and uses a 1.6 m^3 vacuum tank to create the flow through the test section. The vacuum tank is connected to an *Elmo-Rietschle V-VC100* series vacuum pump on one side and the test section on the other, using a paper gasket to isolate them. First, the vacuum tank is evacuated to a desired low pressure. To initiate a run, the gasket is punctured using a solenoid operated mechanism. The pressure difference between atmosphere and vacuum tank forces air to enter the compressor cascade through a fifth-order polynomial bellmouth. The desired inlet Mach number is set using an iris valve with an adjustable throat. This chokes the flow downstream of the test section, enabling the inlet Mach number to be lower than unity. For this compressor cascade, an inlet Mach number of 0.7 was set for tests at different incidence angles. Cascade data were recorded during the steady state wind tunnel operation: about 0.6 sec in duration.

3.2.2 Compressor Linear Cascade Setup

3.2.2.1 Linear Cascade Design

A *Rolls-Royce* A-250 gas turbine engine's axial compressor rotor first stage was used to design the linear cascade blades. This is a single piece part, so blades are integral to the rotor hub. The entire rotor was scanned using 3-D optical *FARO Laser Scan-Arm* to extract the first stage geometry. The single piece construction, made scanning
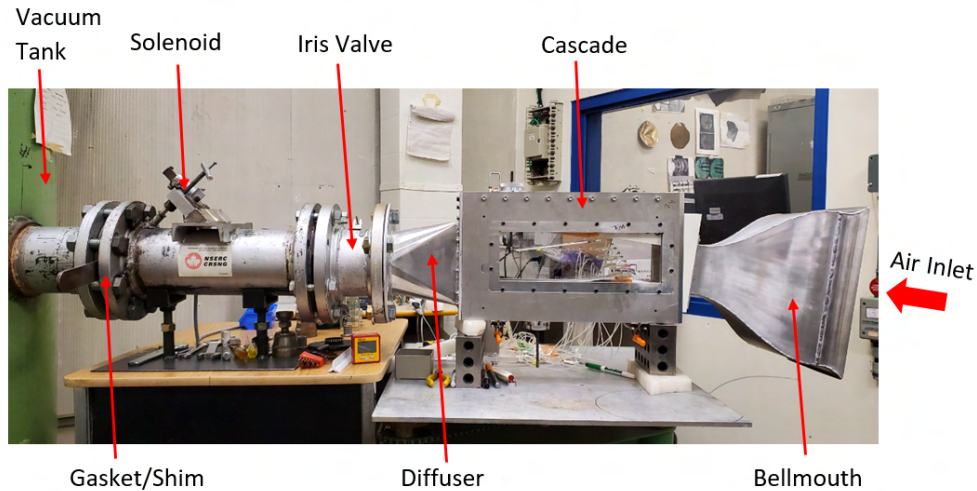
Figure 3.6: Compressor linear cascade test facility

difficult and approximations were used to complete the entire image. The compressor blade with the most data points, representing the most accurate approximation, was isolated. Selected blade points were imported into *SolidWorks* to construct a complete 3-D blade profile and mid-section profile was used for cascade tests. Any uncertainity in this arose from the complex rotor design. To verify the accuracy of the extracted blade profile, multiple blade profile were extracted and compared.

The actual first stage compressor blades are very small, with measured chord length of only 14.9 mm. A 1.5 times upscaled blade was adopted for use in the cascade. A longer scale blade was also needed to allow effective flow visualization. Manufacturing the compressor blades for cascade testing was challenging since they are extremely thin and high aspect ratios were needed for cascade testing. Compressor blade scaling increased the blade chord length to 22.45 mm, consistent with *AGARD* cascade design guidelines [79]. Five compressor blades were used in the cascade, creating four passages. The side walls were shaped to mirror the suction

Table 3.3: Compressor cascade geometry parameters

Parameter	Value	Units
Axial Chord, c	22.45	mm
Span, b	50.8	mm
Pitch, s	22.8	mm
Aspect Ratio (b/c)	2.22	[-]
Solidity (c/s)	0.98	[-]
Stagger Angle (δ)	30	[°]
Inlet Metal Angle (β_1)	39.5	[°]
Exit Metal Angle (β_2)	30	[°]
Inlet Mach Number	0.7	[-]
Reynolds Number, Re_c	3.6×10^5	[-]

and pressure sides of the cascade blade. They were placed at a half pitch distance to mitigate boundary layer interference. Boundary layer calculations were performed and a maximum thickness of 1.9 mm was estimated just before the flow reaches the cascade. To minimize boundary layer effects on perodicity, a half pitch gap on the both sides of the cascade was estimated to be sufficient. Two side walls were manufactured using a 3-D *Fortus 380mc* printer using *ASA black filament* material. The end walls were *Plexi glass* windows to facilitate installation of compressor blades and allow for flow visualization. Plastic holders tightly fitted into the Plexi glass window, were used to insert the blades into the cascade, as shown in Figure 3.7. The blade holder allowed for quick blade replacement.

In the post bellmouth section, interchangable wedges were used to guide the flow at different AOI. The zero AOI was designed to be along the leading edge of camber line of the baseline blade and side wedges were used to align the bellmouth with the incoming flow. Bellmouth wall profiles were designed using a fifth-order polynomial to minimize inlet flow disturbances [80]. The geometric parameters of the compressor cascade are listed in Table 3.3.
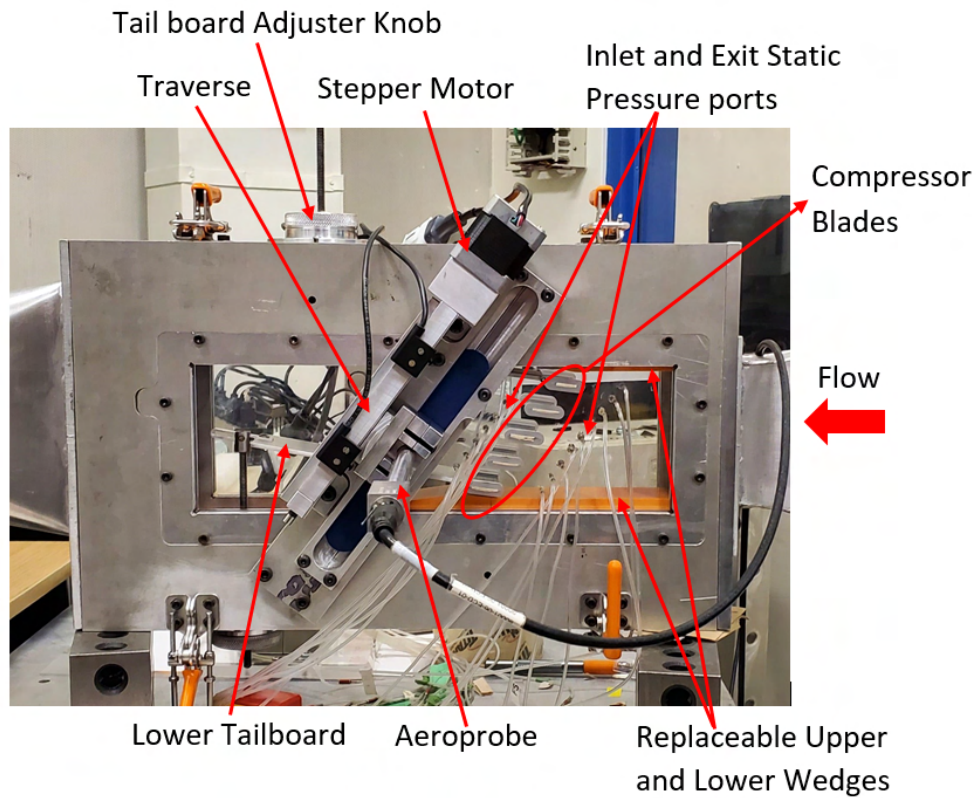
Figure 3.7: Details of compressor cascade

Two cascade tailboards were used to perform the adjustments to periodicity. Tailboard installation and adjustment mechanisms were designed to be operated from outside the sealed compressor cascade. Tailboards were controlled using a self-locking, fine-threaded rod, controlled by a threaded wheel; see Figure 3.7. Periodicity was measured using the inlet and exit wall static ports. Nine inlet static ports were set one axial chord upstream of the cascade. Five static ports were aligned with the compressor blades and four at mid-passage. Exit pressure was measured using seven static pressure taps about 3/4 of the blade chord downstream of the cascade. Three pressure taps were aligned with the blade trailing edge and the rest were set

at mid-passage. All airfoil sets were tested at AOI by sequentially interchanging blades. Flow conditions were kept constant and minimal adjustments were made to the tailboards from run to run.

3.2.2.2 Cascade Blade

The tubercle amplitude on the order of 1.35 mm on the small blades complicated their manufacturing and the choice of 3-D print material. The cascade blade geometric parameters are given in Table 3.3. The feasibility of multiple materials was explored to achieve smooth surfaces and accurate tubercle geometries. Since the test models were thin and air loading was high, 3-D printing materials like *Accura bluestone, Vero black plastic* and *Accura ClearVue* were tested for their suitability to meet anticipated blade stresses without failing or flexing excessively. 3-D metal printed blades were also explored, but the surface finish was coarse at the small geometries. *Accura bluestone* was tried due to its high strength, but its poor repeatability in finer resolution tubercle regions was unsatisfactory. Ultimately, *Acura ClearVue* was used for manufacturing the compressor blades. A flow coefficient of 0.3 was used for the calculation of loads at an AOI of $10°$ [16]. The average value of the material's listed flexural modulus with an assumption of fixed end continuous load conditions resulted in a maximum deflection estimate of 0.22 mm at mid span. Blades were carefully sanded to achieve the desired smooth surface and consistent dimensions for all blade geometries. Roughness coefficient was not measured but the test blades were all sanded to a qualitatively assessed smooth finish. An initial set of tubercle shapes was selected and tested. Details of the tubercle selection process and geometries are explained in the next section. From the initial analysis of the cascade results, two new tubercle geometries were selected for testing with improved manufacturing

technique.

3.2.3 Instrumentation and Data Acquisition

3.2.3.1 Total Pressure Measurements

Total pressure measurements were performed in wake surveys for the comparison of different tubercle shapes. *Aeroprobe* ER fast response, 5-hole, L-shaped probe was used for total pressure measurement. The detailed dimensions and shape of the *Aeroprobe* are shown in Figure 3.8. The probe's small size and diameter ensured minimum blockage at the exit of the compressor cascade. A *Velmex* stepper motor, controlled using an automated *LabView* program, was used to traverse the probe pitchwise. A maximum sampling rate of 20 kHz was available for the probe, but 10 KHz was deemed sufficient for this application as it allowed 500 samples per mm of traverse. The probe was mounted onto the traversing system, controlled using a stepper motor time synchronized with the tunnel operation using a *Kulite* pressure transducer. The probe was traversed at 20 mm/sec, recording about 500 samples per mm of traverse. The probe was centred at the mid span of the blade, aligned with the exit static pressure ports at about 75% of the chord length. The probe was aligned horizontally at 0° AOI and this was checked repeatedly during the testing using an precision electronic level with an accuracy of $\pm 0.01°$. *Aeroprobe* has a listed uncertainity of about 0.4° in flow angle and less than 0.8% in total flow velocity.

3.2.3.2 Static Pressure Measurements

The idea of having static pressure ports on the blade suction surface was explored. However, their very small thickness (2 mm) and barely sufficient strength of the
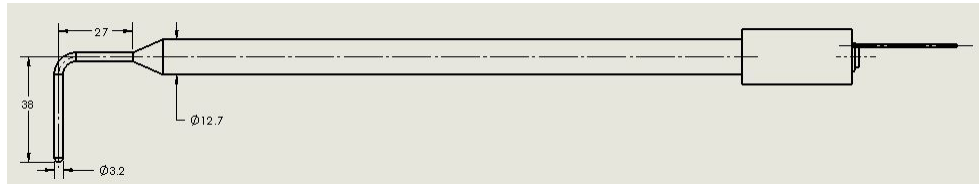
Figure 3.8: 3.2 mm diameter, fast-response, L-shaped, 5-hole *Aeroprobe*

test blades restricted their implementation. Endwall static pressure measurements were made using nine pressure ports at the inlet and seven at the exit as mentioned in section 3.2.2.1. All the 16 pressure taps were connected to the *Scanivalve DSA 3217/16Px* scanner with a full scale of 15 psi and a listed accuracy of 0.1% full scale. Static pressure measurements were converted to Mach numbers to assess periodicity. Mach number standard deviation maintained throughout the testing was ±0.004 at the inlet and ±0.0035 at the exit representing about 1.14% of Mach tested.

3.2.3.3 Data Acquisition

LabView was used to integrate the multiple data acquisition systems. A separate *LabView* program customized by *Scanivalve* for their scanner was used to measure static pressure measurements while a *LabView* program was designed to integrate the stepper motor and the *Aeroprobe*. The latter had custom-designed software to record pressure values directly, however this system did not allow integration with the *LabView* used to control the stepper motor. *Aeroprobe* measurements were integrated with the stepper motor control to relate the measurements with its position. The program was designed to record the voltage of the *Aeroprobe* and results were converted to the pressure measurements using a *MatLab* program, with position provided by the *Aeroprobe* software. Wake surveys were performed using the traverse moving
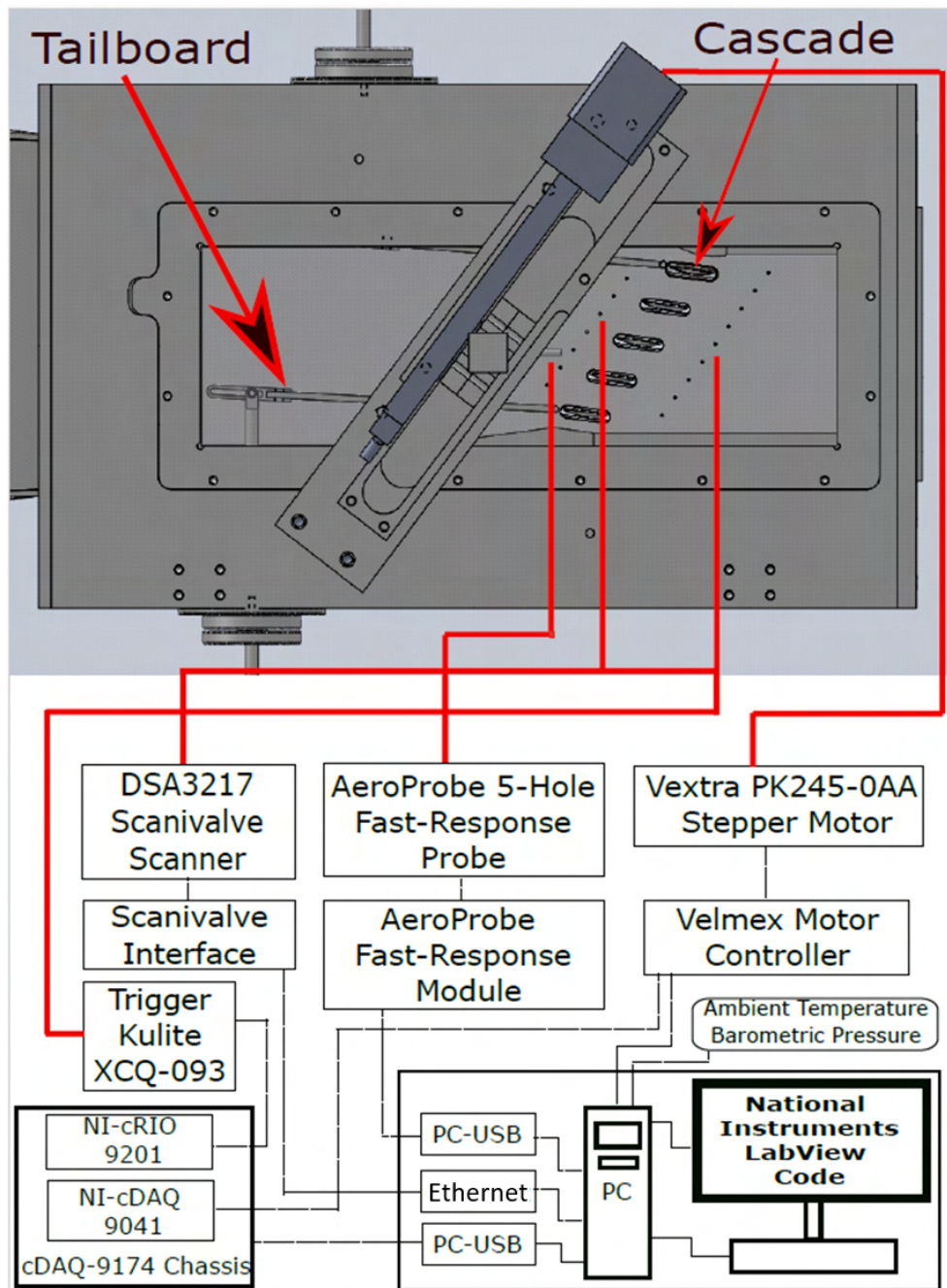
Figure 3.9: Instrumentation layout for compressor cascade testing

from pressure side to the suction side of the blade. A *Savitzky-Golay* filter was used to smooth the data and to understand specific frequencies of interest. Multiple polynomial and window sizes were tried to ensure that any important data value is not being missed. A detailed layout of the data acquisition system is shown in Figure 3.9.

3.2.4 Periodicity
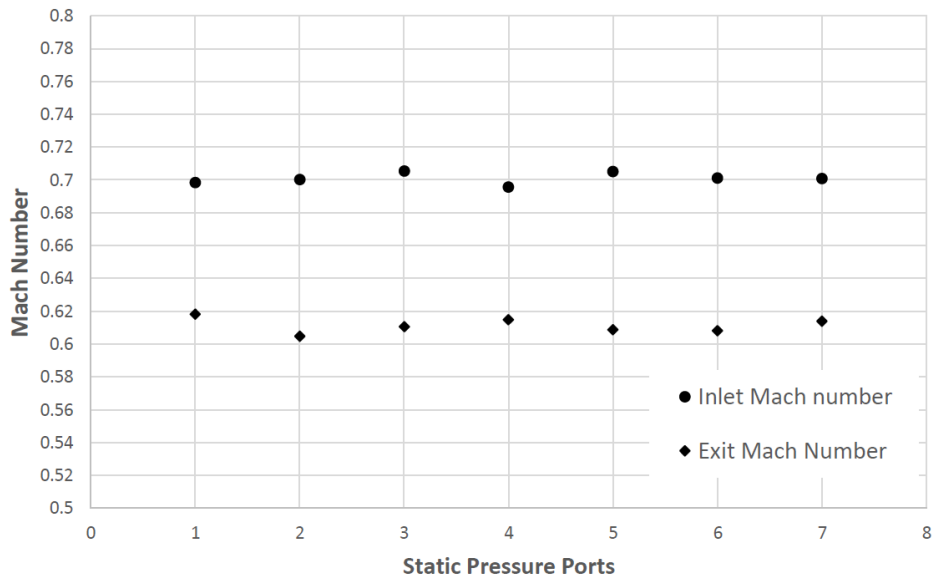
Figure 3.10: Cascade periodicity example

The periodicity of inlet and exit flows of the compressor cascade was tested using the static pressure ports for each test run on every airfoil. The combination of iris valve and two tailboards were used to adjust periodicity. While the iris was primarily used to set the inlet Mach number. Testing on all airfoils was performed consecu-

tively for each AOI. Minor adjustments were made to the tailboards to ensure that periodicity remained within acceptable limit of about ±0.004 standard deviation of inlet Mach for all airfoils. Tailboards were moved in parallel as a common practise and an example periodicity plot for one of the test runs is shown in Figure 3.10.

3.2.5 Flow Visualization

Most published tubercle research and flow visualization has been performed at low Mach number. For this research flow visualization was performed in the cascade to understand the flow phenomenon primarily on the suction surface of the blades, using the mixture described in Section 3.1.2.4 for the low speed wind tunnel tests. There were no gravity effects this time. Flow at higher Mach number mobilized the mixture at much higher rate than observed in low speed wind tunnel. It was not possible to photograph the flow because steady state flow only existed for about 0.6 *s*. A high-resolution video camera was used to record flow images on the casacade middle blade in blacklight and post test still images were also taken.

3.2.6 Pressure Sensitive Paint (PSP) Technique

Pressure sensitive paint (PSP) was used to perform the flow analysis and compare flow separation on different airfoils leading to blade stall. All PSP equipment was purchased from *Innovative Scientific Solutions Inc. USA* including paint, camera, and light.

3.2.6.1 PSP Camera

A *PSP-CCD-C* camera shown in Figure 3.11 was used to capture the images of the blade under different flow conditions. PSP-CCD is a 2 MegaPixel charged coupled

device (CCD) camera. The specifications of the camera and other equipment are listed in manufacturer's manual [81]. The camera was mounted on a tripod to set it at an optimal angle to capture the complete blade surface. *ProAcquire GigE* software installed on the *Windows* PC was used to control the camera and process the image during the test. The camera was connected to the computer using ethernet connection. Variables such as camera exposure time, number of frames, average of frames were decided based on the wind tunnel run time.

Figure 3.11: Image of PSP-CCD-C camera used for PSP [9]

3.2.6.2 PSP Software

The *ProAcquire GigE* interface allowed camera feature during operation. *ProAcquire GigE* did not allow any integration with the *LabView* software to synchronize the wind tunnel operation and camera triggering, so the camera and wind tunnel were triggered simultaneously. Multiple frames were captured over a period of exposure decided based on the application. The software could average all the frames over the period of exposure. In a normal, longer steady state operation, average can be selected where software will average frames captured and provide the finalized im-

ages with pressure distribution on the blade surface. Due to the short run-time of these tests, no averaging was used and all frames were saved in the computer for post processing.

Camera synchronization with wind tunnel could not be automated due to incompatability of the two different software suites. Finally, *ProAcquire GigE* was programmed to capture the frames which were manually analysed by importing files in the software. The camera was trigrered for 3 seconds capturing 60 frames.

3.2.6.3   Pressure Sensitive Paint

PSP is an optical sensor for the surface pressure measurement. UniCoat and Binary UniCoat are two types of coatings used for different applications. UniCoat is a single-luminophore suitable for application requiring slightly lower pressure sensitivity and is ideal for academic applications for its ease of use. Binary UniCoat are packaged in aerosol cans and involves acquiring data from two distinct luminiscent dyes to compensate for errors caused by model displacement. Aerosol spray cans of *Binary UniCoat* PSP were used on the blade which provided consistency and a suitable outcome in transonic flow. A paint gun and air brush were employed ensuring the uniform application of paint on the blade surface.

3.2.6.4   PSP Setup

Only the middle blade was painted using a Binary Coat. Hardware setup for PSP measurement was as shown in Figure 3.12. The camera was aimed at the test blade from one side of the Plexi glass window. UV LED light was focused on the test blade from the other side, illuminating the paint for the camera. UV LED light was allowed to settle for 5 minutes before any data acquisition was performed and camera

filters were installed over the lens, per the table listed in user manual and the camera was controlled using the *ProAcquire GigE* software. A preview from the camera was used to adjust focus on the test blade until the image looked clear and well exposed. For this specific setup, a total of 60 frames were selected and a maximum exposure time of 50,000 μs. (The unit $m$sec is less commonly used by PSP users.) These settings allowed the camera to record 20 frames per second for a total of three seconds used. The averaging tab was kept at unity to ensure no frames are averaged since they were to be post processed individually. Once the setup was finalized, no changes were made, and sets of compressor blades were swapped sequentially to ensure repeatability.
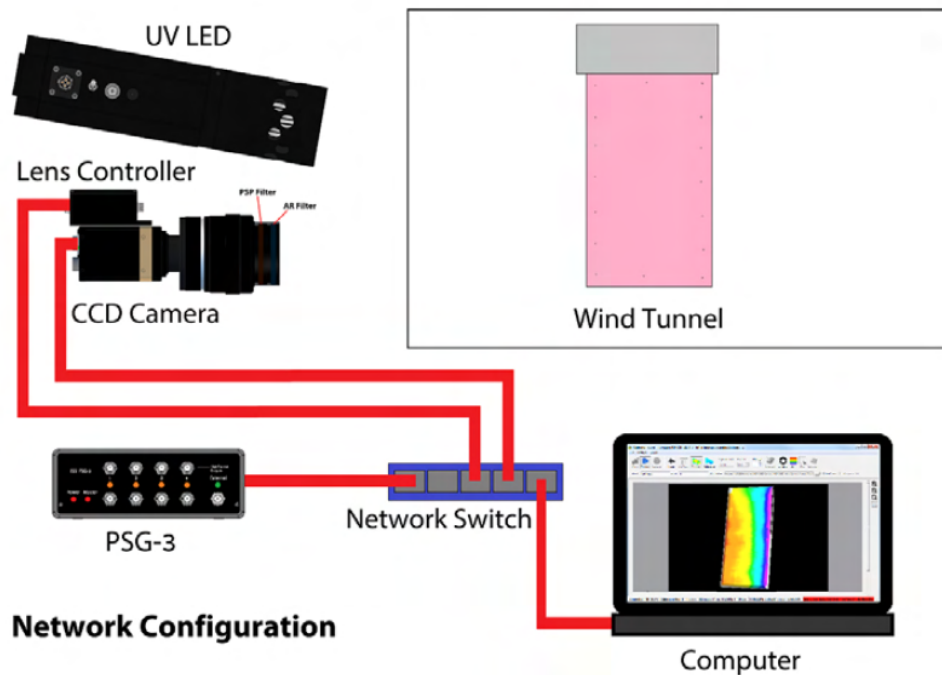
Figure 3.12: PSP camera setup demonstration in the wind tunnel [9]

PSP testing was performed in a dark lab ensuring no outside illumination in the

room. An image of the background condition was acquired first, ideally in complete darkness then a reference frame was acquired with no flow, but with the experimental illumination source on. All three images are taken at similar environmental conditions with minimal light entering the room.

Images saved were imported subsequentially to determine the frame number at which the wind tunnel flow started. Wind tunnel flow progression could be seen in the frames as pressure dropped on the suction surface. The camera captured frames at its maximum speed of 20 frames per second and provided enough images to have confidence on the data captured. Standard procedures were drafted to select the frames captured for data analysis for each blade. Each set of frames captured provided at least five frames with the same pressure distribution. These frames indicated the steady state wind tunnel operation where all five frames were processed for results and comparison to detect any irregularities. Selected frames during steady state wind tunnel operation showed consistent results for all the airfoils at all applicable AOI.

3.3   A-250 Compressor Rig Testing

The A-250 axial compressor consists of six axial stages with slight differences in geometry from stage to stage. Compressor blades had 3-D geometries including twist and lean. Tubercle geometric shape was optimized using only percentage mean chord length because it was not possible to measure accurately the compressor blade chord variation from hub to the tip. In addition, tubercle shape was optimized using mid-blade flow charateristics for first stage relative conditions. The flow conditions varied significantly from hub to the tip due to the radial contribution to circumferential speed. The rotor tip speed of the first stage blade approached the transonic

regime at design conditions; however, 3-D testing was performed at different compressor speeds to generate a complete compressor map, resulting in further complexity. Moreover, the relative speed of the flow for the first stage rotor was in the high subsonic range due to rotational speed but for the stator, it was in the low subsonic range.

To remain within the scope of the study, one tubercle shape tested in the compressor cascade for the first stage rotor mean chord length was selected as the key dimension to modify all the rotor and stator blades, irrespective of the stage.

3.3.1   Compressor Blade Modification

Compressor material information was not available, however testing determined that blades are made of high yield strength, low alloy, hardened steel. Multiple compressor blade modification techniques were explored. One of the initial ideas explored was to use a tubercled griding disk pressed against the leading edge of the compressor blades. The single piece compressor rotor design and two stator shells with small spaces available to reach the leading edge of the blade made the modification by this method highly challenging. The compressor blade's complex shape restricted this method application due to the anticipation of results with low accuracy. Moreover, the operation needed 5-axis machining that was not available. All but one machining companies refused to take on the work due to the small size of the tubercle geometry, its complexity and required accuracy.

Once the leading edges were modified to the A3L11 pattern, with consequent stress concentrations, the hardened A-250 compressor blades could be at risk of cracking. For this reason machining with cutting tools was not explored. Plunge Electrical Discharge Machining (EDM), also called *Sinker* EDM machining, was

Figure 3.13: Electrode used for the modification of compressor blades

also explored due to its high accuracy. Plunge EDM was finally selected for compressor blade modification due to its high precision, and likelihood of least damage to the blades. Modification of the compressor blades was performed in two steps: In the first step, the wire EDM machine was used to cut the flat surface of the electrode, in the shape of the electrode shown in Figure 3.13. A high accuracy of ± 0.001 inches (0.0254 mm) was achieved and a custom-designed fixture was manufactured to hold the compressor rotor in place.

The compressor rotor was dipped in the highly refined dielectric oil to achieve an optimal rate of material removal and to achieve best tolerances. In the plunge EDM process, the electrode is moved very close to the blade leading edge and pulsating high frequency current is applied. The material from the compressor blade is removed at a very controlled rate generating the tubercles valleys. The process was completed when the leading edges of the blade had been eroded sufficiently to craft a

74
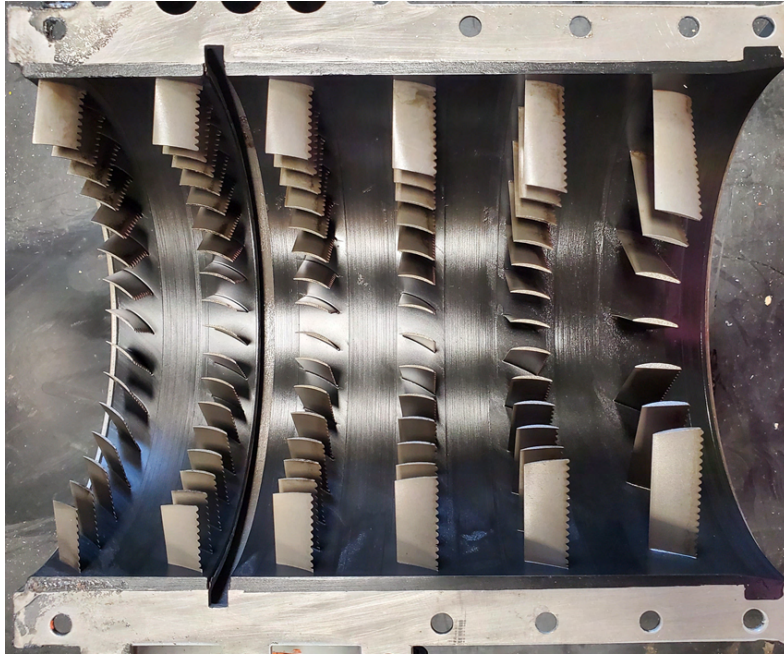
Figure 3.14: Tubercle modified compressor stator shell

smooth tubercle shape. In the A-250 compressor rotor stages two and three are manufactured as a single piece. To modify the third stage rotor blades, a semi-circular electrode was manufactured and used in the confined space. Similarly, for compressor stator shells, a single piece holding a $180°$ sector of all stator blades from stages one through six was used as shown in Figure 3.14. These were also modified using the semi circular electrode. To improve the tubercle shape precision and consistency, multiple sets of electrodes were used throughout the manufacturing process. The modified compressor rotor blades are shown in Figure 3.15.
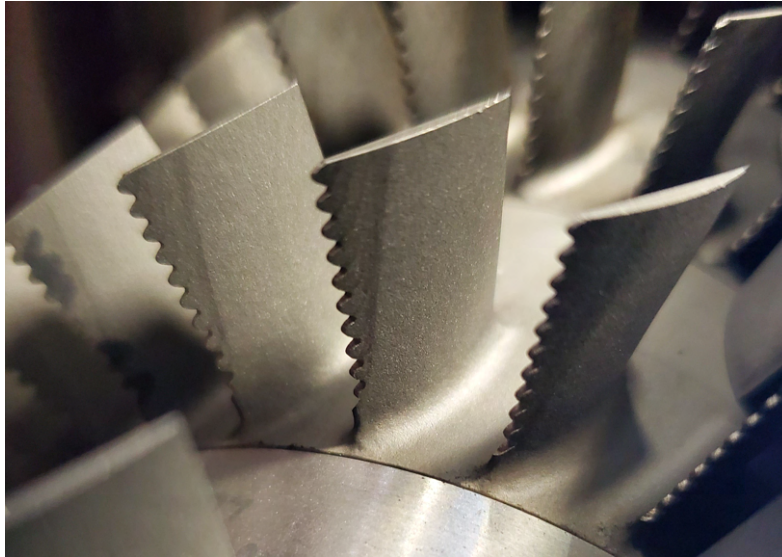
Figure 3.15: Tubercle modified leading edge of compressor rotor blade

3.3.2 Compressor Rig Setup

3.3.2.1 Power Input

It is attractive for researchers to control experimental conditions fully over the complete range of operation, and fortunately, gas turbine engine components can be tested separately. Greitzer *et al.* [28] presented a theoretical compressor model listing the minimum components required for the testing. The key components required are: a bellmouth inlet, the compressor, a diffuser duct, a plenum and a throttle valve as sketched schematically in Figure 3.16. The same layout used in this work.

For this work, the full-scale *Rolls-Royce* A-250 compressor rig at the Royal Military College of Canada was used. It was first commissioned in 2006 by Bennett [2] for his work on the characterization of A-250 axial compressor stall behaviour. The model A-250 compressor was selected for this compressor rig due to its modular de-
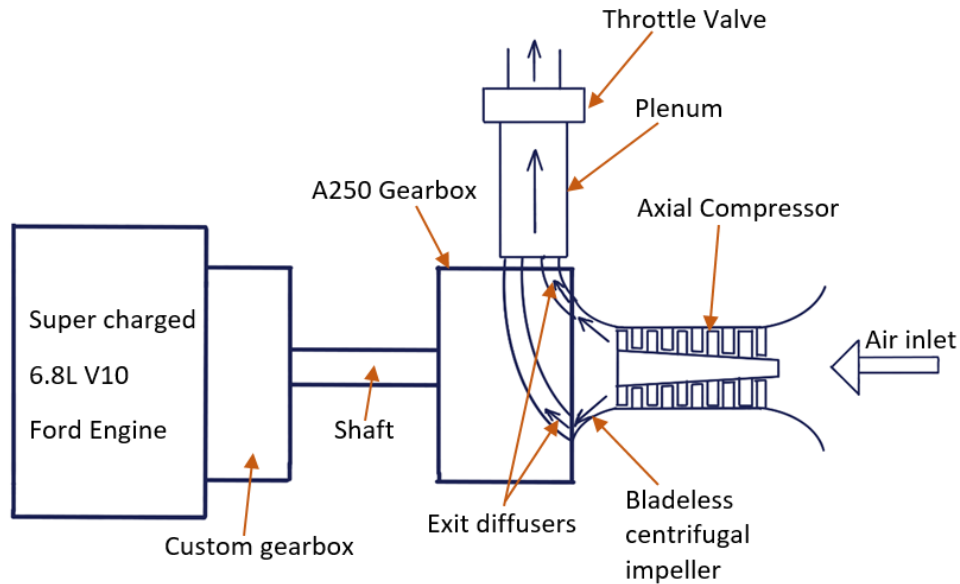
Figure 3.16: A-250 Gas turbine compressor rig layout

Table 3.4: Model A-250 performance parameters [2]

Parameters	Values	Units
N	50970	RPM
Maximum tip speed,	298	m/s
$\dot{m}$,	1.56	kg/s
D	11.176	cm
Re_c	1.3×10^5 -2.25×10^5	[-]
Π	7.1:1	[-]

sign shown in Figure 3.17. The compressor was assembled using refurbished parts declared non-airworthy. These parts had the same fit, form, and function but were not reliable for the air operation. The compressor was powered using a super charged, 6.8 litre, V-10 *Ford* engine. The essential specification of A-250 compressor is given in Table 3.4. The A-250 compressor design speed is 50970 revolutions per minute. A gear ratio of 11.08 to 1 was achieved using a series of custom designed gearboxes.

The original purpose of the rig was to study the axial flow compressor for its stall characteristics [2]. To simplify this effort, the centrifugal compressor was removed but the impeller was not removed from the compressor to maintain the integrity of the assembly. It was modified by grinding down its vanes to the roots. Removal of centrifugal compressor would change the pressure and direction of the air exiting the compressor so the exit diffuser was redesigned to accept the exit flow of the sixth axial stage.
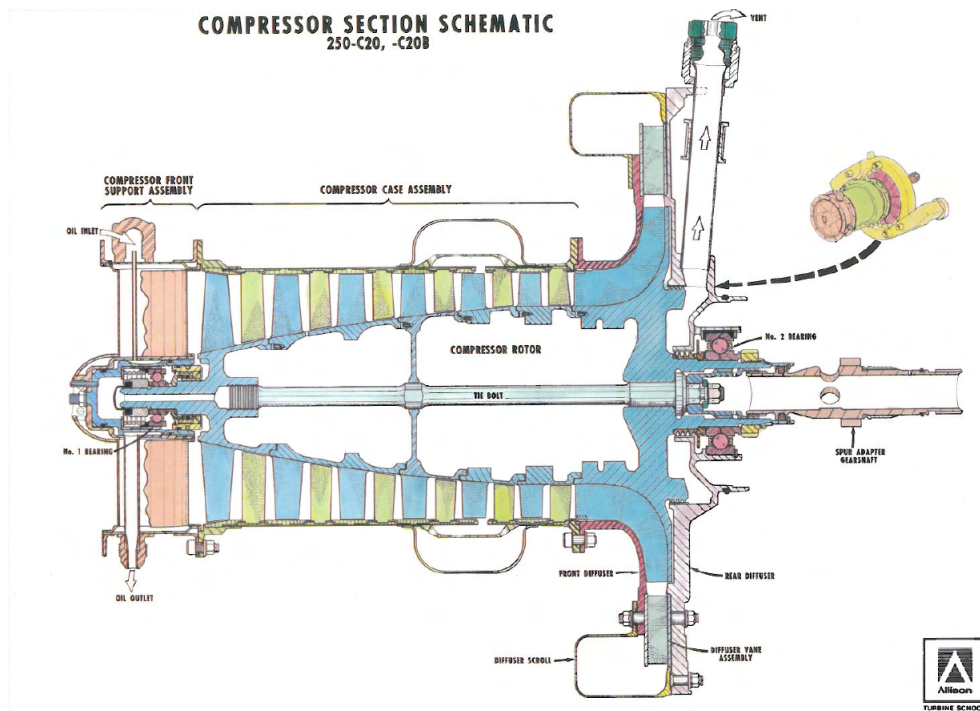
Figure 3.17: A-250 Gas turbine compressor cutaway [2]

The RMC compressor rig was later used by the Ilott [10] for his work on the characterization of the discharge flow from the full dual volute, axi-centrifugal compressor. Ilott studied the complete A-250 compressor, while Bennett focused on the six

axial stages. Ilott calculated the power requirement of the axi-centrifugal compressor using a thermodynamic analysis. It was estimated that the maximum input power required to run the compressor at its design speed was 610 Hp. The power output of the *Ford* V-10 automotive engine was increased using an after-market supercharger kit manufactured by *Paxton*. A belt-driven centrifugal compressor supercharged the V10 engine to an estimated power output of 425 Hp. The V-10 engine was modified to produce this output when operating at an output shaft speed of 4600 rpm.

But the modified V10 automotive engine was still not able to match the input power requirement of compressor so the compressed flow from the compressor was redirected to power the A-250 turbine prior to releasing it to the environment. Ilott performed theoretical calculations and determined that even a moderate pressure ratio of 2.9 in the turbine was sufficient to meet the power needs of the A-250 compressor. The compressor exit tubes were therefore modified to reroute the compressor discharge flow back to the turbine inlet through a throttle valve. The combustion chamber was not used in the testing but the flow was routed through it to the turbine.

The A-250 is a twin spool turbo-shaft engine with a high pressure turbine (HPT) powering both axial and centrifugal compressors and a power turbine (PT) driving a shaft propeller through a gearbox. The A-250 gearbox was used to couple the V-10 and turbine, providing a gear ratio of 5.53. In this configuration the PT and HPT spools were coupled to apply the power in parallel with the V-10, backwards through the A-250 gearbox.

Since the present work was concerned with the application of tubercles on the axial compressor, modifications were made to restore the full axi-centrifugal compressor used in Ilott's tests to a simple axial configuration used in Benett's work. Initially it was decided to use the same compressor exit tubes with some power in-

put from the turbine, however, after performing multiple runs, it was found that flow was choking and the axial compressor was not able to perform at the expected flow conditions. There was also a possibility that flow was choking at the throat of two venturis used to measure the discharge mass flow rate of the compressor. It was also suspected that the flow was choking due to the flow separation at $150°$ turn after the compressor discharge. During Ilott's testing, the centrifugal compressor increased fluid density to prevent choking in these locations. To alleviate these problems, the compressor exit tubes were replaced with the ones used by Bennett in his work.

Ilott used the A-250 turbine in parallel with the *Ford* engine to power the compressor. In the present work, the turbine section was not required to perform this testing since power requirement was reduced with the centrifugal impeller removed. Compressor exit tubes from Bennett's work released the compressed fluid into the environment directly rather than routed to the turbine inlet. To avoid further major modifications, the turbine was left connected to the compressor. The V10 engine was able to run the compressor with the turbine free wheeling, but isolated from the flow.

3.3.2.2 Throttle Valve

Bennett used a pneumatically controlled butterfly valve for throttling the compressor and this was improved upon by Ilott in his work [2, 10] by introducing an electromechanical actuation mechanism. The operation of butterfly valve is in itself a non-linear operation. It was recommended by Ilott to improve the throttle valve control to make it more linear, especially when operating near stall conditions. For the present work, the throttle valve was completely redesigned and a shutter valve design was selected and manufactured. The shutter valve was linear in motion. A 3-D model of the valve is shown isometrically in Figure 3.18.
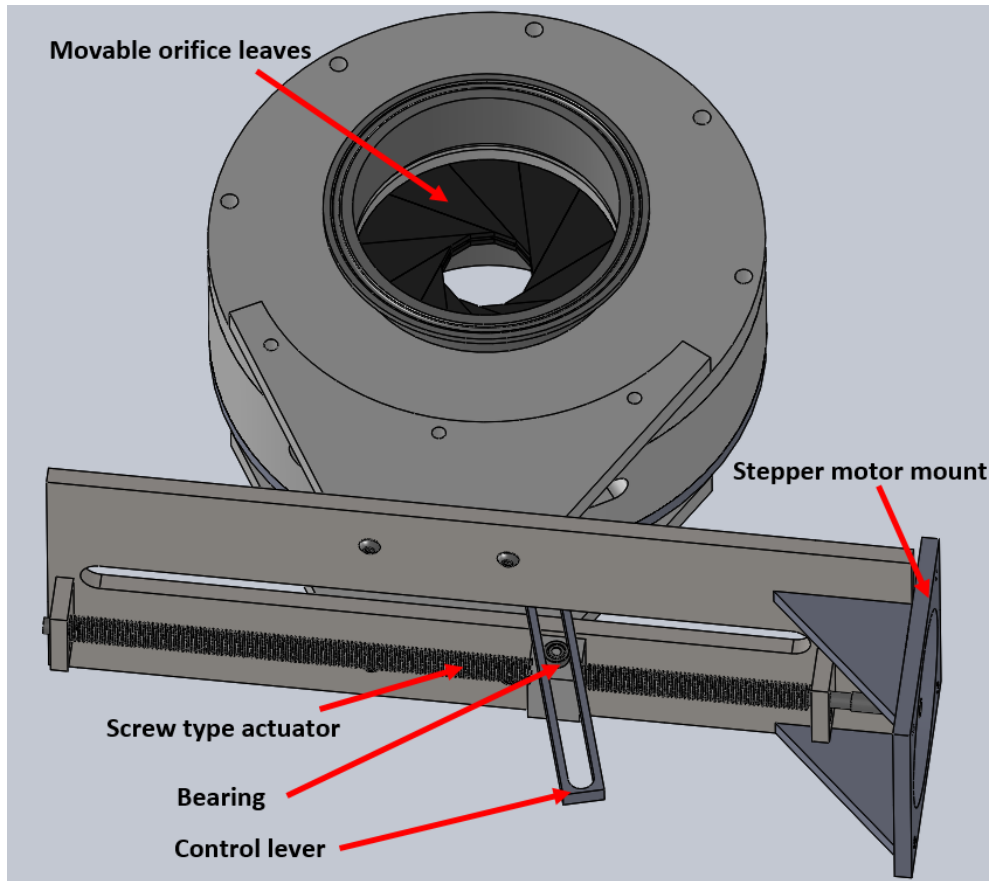
Figure 3.18: Custom designed throttle valve

The shutter valve's design was based on mechanical iris where, at its fully open position, there was no obstruction to the flow. Twelve leaves interconnected using grooves and pins that were rotated with a guide disk. The guide disk was further connected to the control lever using a threaded hole. The circular motion of the lever was converted to a linear path using a sliding joint and a small bearing, that eliminated the friction between the two mating surfaces. The linear mechanism was selected to simplify the operation and to use existing equipment.

3.3.2.3 Compressor Flow Path
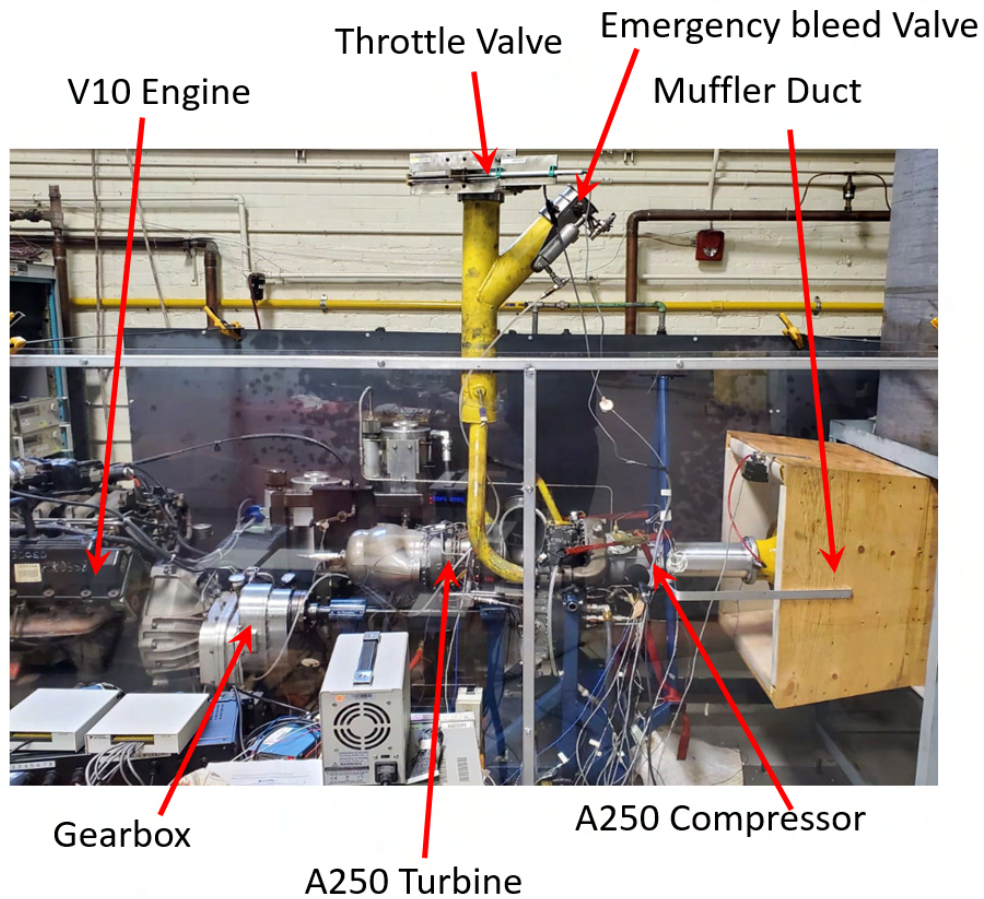
Figure 3.19: A-250 Gas turbine compressor rig

A photograph of the compressor rig, is shown in Figure 3.19. The flow enters the compressor from the right through the muffler duct and a bellmouth (the yellow component visible in the muffler duct). The mass flow rate is measured at the bellmouth using the differential pressure transducer. After passing through the bellmouth the air enters the A-250 axial compressor, then exits through the modified vaned diffuser. It

is finally delivered to diffuser tubes through the volute. The compressor exit pressure is measured using a pressure transducer on both left and right exit diffuser tubes. The flow is directed vertically through the yellow-coloured plenum in the upper centre of Figure 3.19 and then through the throttle valve. The compressor load is controlled using the custom designed shutter valve previously described. A separate blow-off exit was installed on to the side of the throttle valve to allow an instant unload of the compressor should an emergency be encountered.

3.3.2.4 Test Facility and Assembled Test Rig

The supercharged V10 6.8 Litre automotive engine required heat exchangers to maintain coolant and oil temperatures in specified range. Another heat exchanger was used for the A-250 gearbox oil. The existing lubricating system designed by Bennett *et al.* [2] was retrofitted for this work. Two oil reservoirs were mounted on the side of the rig, feeding oil to V10 and A-250 gearboxes. An oil pump was retrofitted to supply oil from the reservoir to V10 and the A-250 engine driven oil pump was used to supply oil to compressor, gearbox and turbine sections. Scavenge pumps were used to collect oil from compressor and turbine, and to route it back to the A-250 gearbox. The A-250 ran this internal pumping system using gear reduction from the shaft.

For this work, many improvements in the compressor rig were made to ensure safe operation of rig. Two magnetic plugs from the A-250 gearbox were connected and warning lights installed in the control booth to detect any debris before it damage the engine. A mechanical pressure gauge, electronic pressure tranducer and a J-Type thermocouple were fitted to the gearbox port to monitor oil conditions from the control booth. This was a preventative measure after an incident which resulted in a

bearing failure due to oil starvation.

The entire rig was placed on a large steel pad with T-slots to provide stability. This also facilitated the alignment and attachments of individual parts and ensured the rig was firmly fixed while in operation. A muffler was installed upstream of the compressor to absorb the excessive noise. The compressor rig was operated from the sound insulated control booth.

3.3.3 Data Acquisition and Compressor Rig Instrumentation

A data acquisition system designed by Ilott [10] was inherited for this work. Data acquisition system and instrumentation were modified and replaced for present work. A dual-core real-time *National Instruments PXIe-8108* controller was dedicated to real-time data acquisition while a *LabVIEW Real-Time (LVRT)* software interface was used for the measurements and hardware control. The dual core *PXIe-8108* and other *PXI* devices were installed in *National Instruments PXIe-1082* chassis. A *PXI-1082* sampling clock was used for the phase synchronization of the low- and high-speed data acquisition. Low-speed data acquisition used the *PXIe-6361*. A *PXIe-6368* module was used for high-speed records. Low-speed data acquisition was primarily used for compressor discharge pressure measurements while a separate *PXIe-4353* data acquisition card was used for measuring temperature from all thermocouples on the compressor rig.

3.3.3.1 Software and Data Architecture

The *PXIe-8108* processor had some inbuilt data storage space that ensured no loss of data during experimental runs and was designed to store all data. The *LabVIEW Real-Time (LVRT)* operating system, *Target*, allowed remote and independent op-

eration of data acquisition, providing deterministic execution of data recording and control. The control inputs and data were shared across the systems using real-time network variables controlled from the desktop computer (PC) situated in the control booth. The *LVRT* data system was installed in close proximity to the compressor rig, ensuring minimal signal noise and LVRT *Target* was connected to PC using TCP/IP connection. The recorded data were transfered to the PC after each run to restore data space to the *Target* hard drive. This is all shown schematically in Figure 3.20.
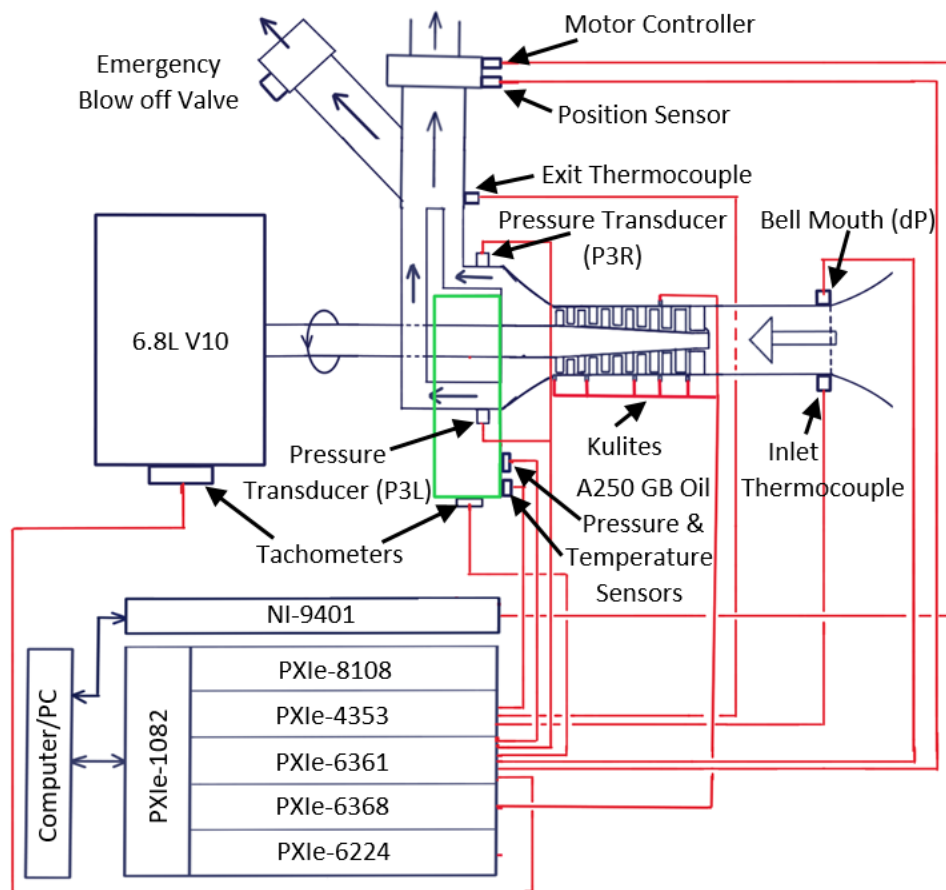
Figure 3.20: A-250 Compressor rig instrumentation layout

Software data architecture was designed to provide separate user interfaces for the automotive engine and the compressor operator. It allowed each individual to focus on their respective panel without distractions during the operation. The automotive engine operator set engine speed and monitored coolant and lubrication, ensuring safe operation of the V10 and A-250 compressor. The automotive and A-250 engine operator's interface is shown on right in Figure 3.21. The compressor operator monitored the compressor instrumentation to verify values remained within limits as shown on left of Figure 3.21.
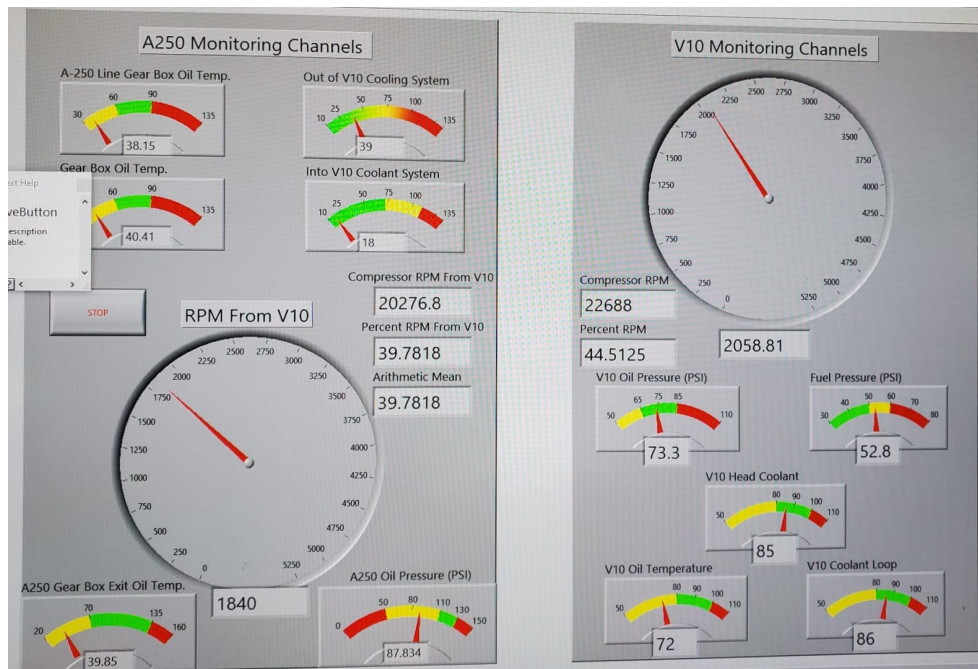
Figure 3.21: A-250 Rig Engine Operators Monitoring Panels

The A-250 compressor monitoring and control interface was designed separately and is shown in Figure 3.22. Compressor pressure and temperature were congregated to the left, with parameters coded to include a visual alarm to prevent damage to the

rig and/or instrumentation. The parameters were displayed in green when within normal operating limits and red to alert the operator of a dangerous state. Vibration velocity values from three different accelerometers were displayed using colour coding for magnitude and values from the Ilott's [10] work were used as maximum limits. The throttle valve was also controlled from this panel and position signal from linear potentiometer (described in section 3.3.3.10) was displayed for the operator.
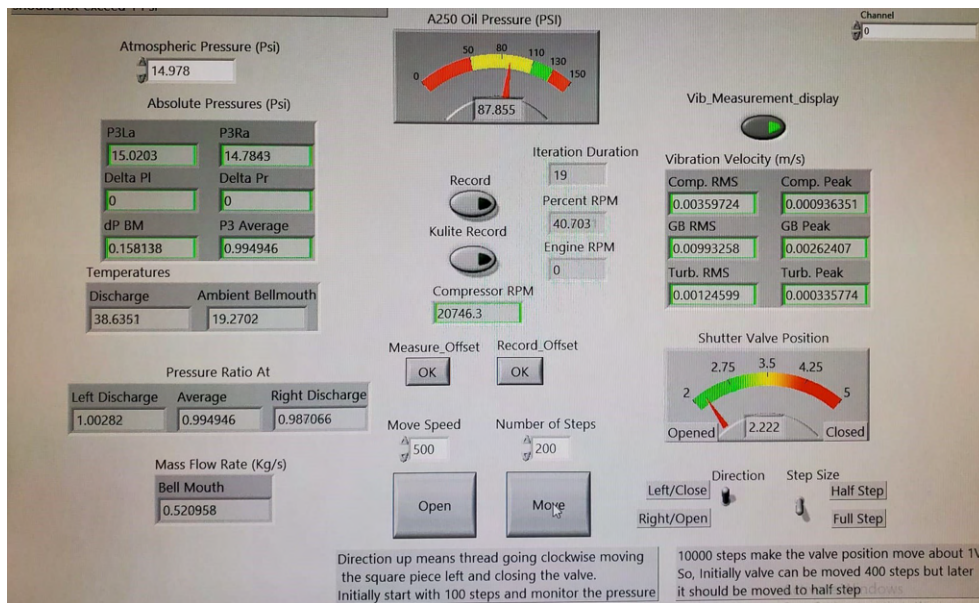
Figure 3.22: A-250 Compressor data acquisition screen setup

3.3.3.2   Low-Speed Data Acquisition

A *PXIe-6361* data acquisition module was used for low speed data acquisition: including outputs from pressure transducers at compressor discharge, differential pressure transducers at the bell mouth, the A-250 gearbox oil pressure transducers and the throttle valve position sensors. Tachometer readings from the A-250 gearbox and

the V10 were also recorded (described in section 3.3.3.9). The *PXIe-6361* module allowed simultaneous sampling of up to 16 single-ended inputs with a maximum combined sampling rate of 1.5 MS/s. The *PXIe-6361* also included 24 digital I/O channels which were used for controlling the stepper motor throttle. For this work, motor control functions were removed due to the excessive noise being introduced to the pressure transducer signals. The *PXIe-6361* provided 16-bit resolution allowing precise measurement of analog transducer data. Pressure transducer data were measured at 8 kS/s with raw values measured and stored to a file on the *Target*. While an averaging function in *LabVIEW* was used to display mean values on the compressor control operator panel, thermocouple data were recorded at 16 S/s using a *PXIe-4553* thermocouple digitizer.

3.3.3.3 High-Speed Data Acquisition

Kulite high-speed pressure transducers were installed at six axial locations along the A-250 axial compressor casing (dexcribed in section 3.3.3.4). The *PXIe-6368* data acquisition module was used to record their output at 2 MS/s taking advantage of the fast response signal available. The *PXIe-6368* allowed the high-speed simultaneous sampling for each of 16 analog input channels with 16-bit resolution. Due to the high sampling data file size, these data approached the maximum limit of the *Target* processor. The *PXIe-6368* was also used for measuring accelerometer data from the compressor and gearbox, also at 2 MS/s. It was not possible to transfer any data with the size exceeding 2 Gigabytes from the target to the host PC. To ensure the data file did not exceed this limit, values were recorded in multiple files, with priority given to the pressure transducer data. In the *LabVIEW* program, high-speed data acquisition was given the highest priority so no samples were lost.

88

Table 3.5: Kulite pressure transducer locations

Axial stage	Location	Kulite model
1	Upstream	*XCE-093-50A*
2	Upstream	*XCE-093-50A*
2	Upstream (120°)	*XCE-093-50A*
3	Upstream	*XCE-093-50A*
5	Upstream	*XCQ-093-50D*
6	Downstream	*XCQ-093-50D*

3.3.3.4 Kulite Placement and Installation

Six *Kulites* were installed at different axial locations of the A-250 compressor: The single *Kulite XCE-093-50A* absolute pressure transducers were used in front of the first and third stage rotor blades and two *Kulite XCE-093-50A* gauges were placed upstream of the second stage, displaced at an azimuth angle of 120°. *Kulite XCQ-093-50D* differential pressure transducers were installed respectively upstream of the fifth stage rotor blade leading edge and downstream of sixth stage rotor blade trailing edge. *Kulite* pressure transducers installed are listed in Table 3.5. These pressure transducers were placed directly between two upstream stator blades to avoid wake effects. *Kulite* transducer, sensing elements were flush-mounted with the compressor shroud to maximize the frequency response of the transducers. A series of holes were drilled in the compressor stator casing and double ferrule type tube fittings were installed on the outer surface of the shroud using *J-B* weld. As shown in a Figure 3.23, this facilitated the installation and removal of the pressure transducers from the modified compressor.

3.3.3.5 Kulite Signal Conditioning

Kulite pressure transducers are piezo-resistive transducers, producing 50 mV at full-scale when excited with 10V supply but are susceptible to aliasing of high-pass fre-
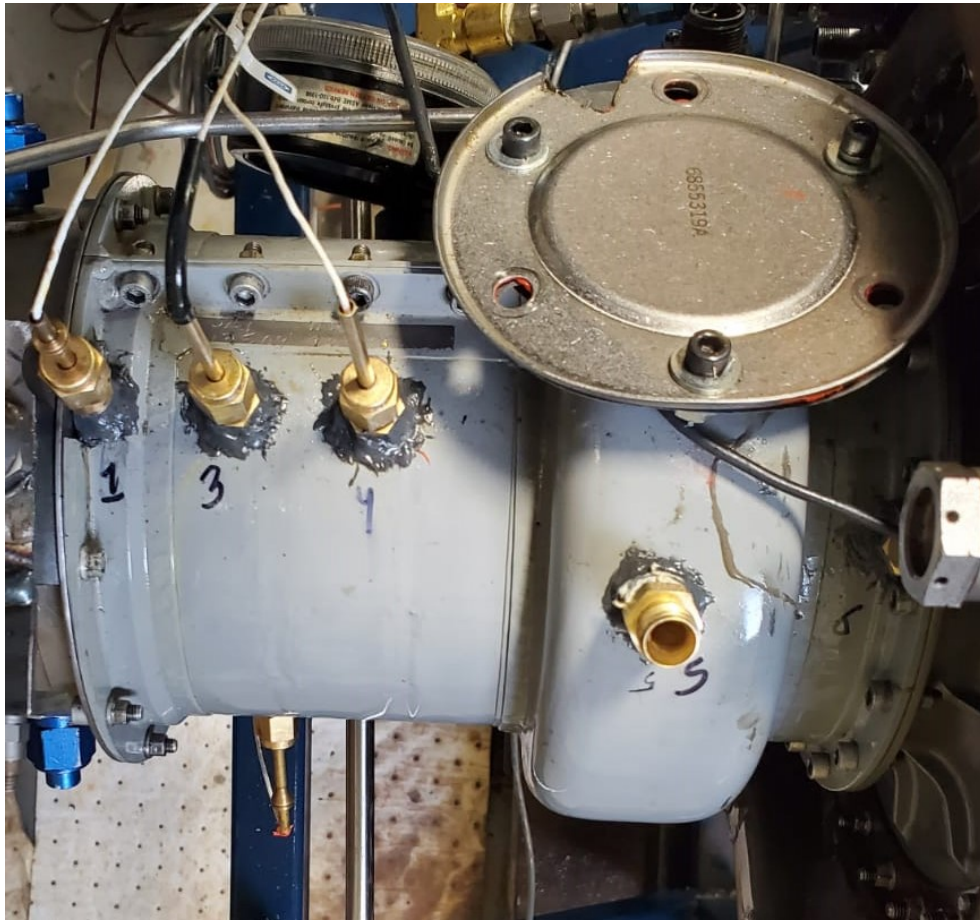
Figure 3.23: Kulite pressure transducer placement at different axial locations

quency signals and to noise. A customized signal conditioner was designed as described by Ilott [10] for his work and restored for this work (Figure 3.24). This unit provided low pass filtering with a cut-off frequency of 320 kHz and a gain of 100. It also provided a constant 10V excitation to the pressure transducers.

3.3.3.6 Throttle Valve Control

A stepper motor was used to actuate a screw-type actuator providing high resolution control of the throttle diameter. An *A-Tech* 8709 miniature potentiometer displacement sensor was used to measure the diameter of the throttle valve, which was calibrated with the linear values of the potentiometer output in voltage, varying from 0 to 5. It was capable of measuring diameters up to 200 mm with a resolution of 0.1 mm.

3.3.3.7 Exit pressure measurement

Pressure transducers were installed on compressor exit diffuser tubes. Two pressure transducers *PX429-100G5V* with a maximum range of 100 psi were used for pressure measurement. These pressure transducers offered accuracy of ±0.08% full scale. Study by Ilott *et al.* showed difference in the mass flow rate among two diffuser tubes [10]. Averaged pressure from two diffuser tubes was used for compressor map.

3.3.3.8 Inlet Mass Flow Rate

The compressor inlet was elongated to dampen out any incoming swirl and a bellmouth upstream was used to determine mass flow. The bellmouth throat had a diameter of 4.469 inch and four static ports at the throat were connected to a plenum to provide an average static pressure for that plane. The four holes were placed 90° to each other and the plenum was connected to an *Omega PX2300-5BDI* differential pressure transducer to measure the bell-mouth throat pressure ratio with ambient total pressure. A *J-Type* thermocouple was connected to the bell-mouth to measure the air temperature. Reasonably assuming incompressibility and no losses, the differen-
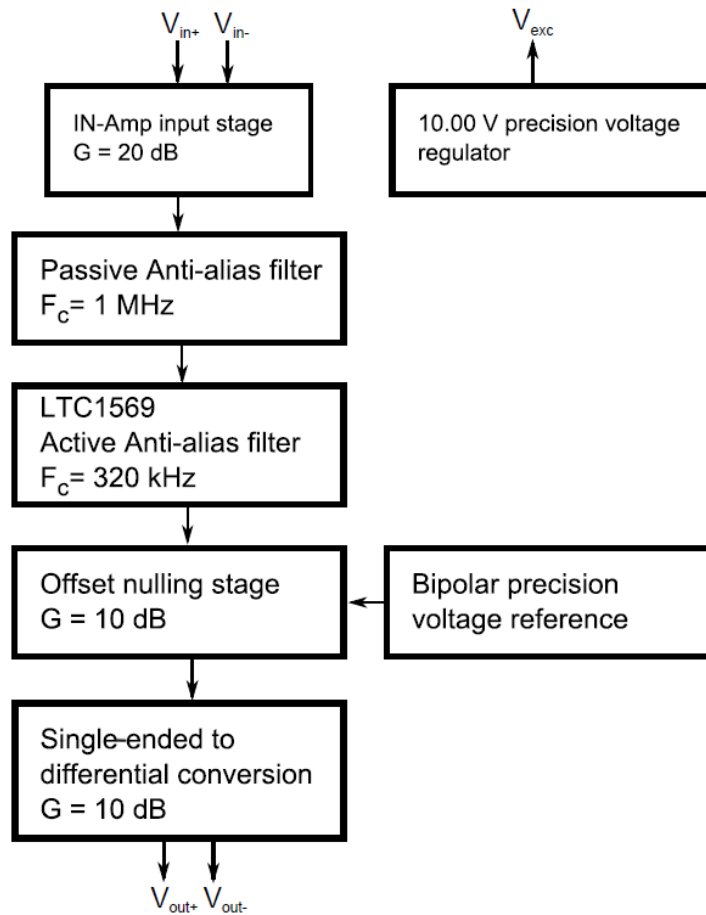
Figure 3.24: Block diagram of analog signal conditioner [10]

tial static pressure drop from the atmospheric to the throat of the bellmouth provided accurate reading of the flow rate using Equation 3.5.

$$\dot{m} = \rho c_d A \sqrt{\frac{2\Delta p}{\rho}} \tag{3.5}$$

Here, A is the bellmouth throat area, Δp is the differential static pressure, ρ is the air density. The discharge coefficient (c_d) was estimated to be 0.994 using average Reynold's number of flow based on bellmouth throat diameter Re_d and Equation 3.6.

$$c_d = 1 - \frac{5.25}{\sqrt{Re_d}} \tag{3.6}$$

3.3.3.9 Rotating Speed Measurement

The A-250 compressor speed was measured using the OEM tachometer-generator connected at the engine gearbox. The 3-pole output from the tachometer was converted to DC signal using *Omega CCT-05-70/125* frequency-to-voltage converter. A tachometer from the *Ford V10* automotive engine was also used to monitor engine RPM and to validate the main instrumentation. The V10 tachometer was used to monitor automotive engine performance, since the A-250 OEM tachometer only provided signal when the clutch was engaged. It was important to monitor the V10 engine during the warm up and startup of the A-250.

3.3.3.10 Experimental Testing Procedures

The tubercled compressor tests were performed methodically as listed in Table 3.6. Initially, the baseline compressor was tested to establish the compressor performance. All rotor and stator blades, were then modified using EDM machining. During the

Table 3.6: Tubercled compressor test configurations

Configuration	Rotor	Stator
1 (Baseline)	Unmodified	Unmodified
2 (Bleed Valve Open)	Tubercled	Tubercled
3	Tubercled	Tubercled
4	Tubercled	Unmodified

second trial run with tubercled A-250 compressor, a bleed valve at the fifth axial stage was partially open. Nevertheless data were valid and proved useful for a baseline comparison. The bleed valve was completely sealed for a third trial on the modified rotor and stator blade configuration. Next, the compressor stator blades were replaced with the unmodified stator blades to evaluate their effects on performance.

Test procedures were established and used for all four configurations: Each trial began with a warm up of the V10 automotive engine while it was isolated from the A-250 compressor by disengaging the clutch. Compressor temperatures remained at normal room temperature during the V10 warm up. After the clutch was engaged, the rig was accelerated to about 30% RPM. The A-250 gearbox oil temperature and pressure both remained low during startup. The compressor was idled at low, 30 to 40% RPM until desired gearbox oil temperature and pressure were reached. Then RPM was ramped up to the desired test point. A complete A-250 compressor test consisted of multiple stall events at different RPMs, bringing the compressor periodically from a stable condition to a stalled condition and back again. Atmospheric pressure and temperature values were recorded at the start of the test session for normalization over test campaign. The test procedure for each RPM setting is explained here:

1. A-250 compressor set at the desired speed.

2. All pressure and temperature readings verified normal.

3. Low-and high-speed data acquisition systems initiated.

4. Throttle valve slowly closed, increasing back pressure and decreasing mass flow rate.

5. During throttle closure, compressor pressure and mass flow rate were monitored.

6. Throttle valve was closed until stall was evident in the compressor.

7. Stall clearly evident from a step change in compressor noise.

8. Unstable pressure and mass flow fluctuations are both indications of stall.

9. Once stall was evident, the throttle bypass emergency valve opened to release compressor load.

10. The main throttle valve rapidly opened using the *LabVIEW* and the data acquisition system stopped.

11. Steps 1-10 were repeated for the each compressor configuration and speed range.

12. Data files for low-and high-speed data acquisition transferred from *Target* to host PC.

4   Results and Discussions

Results of this work will be presented and discussed in three sections: Self-Organizing Maps, Cascade Testing and Compressor Rig Testing. This follows the sequence of work performed as early findings were the crucial input step to subsequent research. This chapter commences with the work performed to optimize the tubercle shape using Self Organizing Maps and low speed wind tunnel testing using existing experimental data. The 2-D linear testing results follow comparing the modified compressor blades performance with the baseline at first-stage rotor design conditions. Finally, optimized tubercle geometry is tested on a modified *Rolls-Royce A-250* axial compressor.

SOM results were analysed to predict an optimal tubercle geometry that would enhance airfoil performance over the baseline unmodified airfoil. This work led to two new test cases, and the results of these two new tubercle shapes are shown. The SOM was then updated, with the two new experimental data sets.

With promising geometries determined, three tubercle shapes were selected for Phase 1 of the blade linear cascade testing at the relative inlet flow conditions for first stage compressor rotor. These results are presented, comparing all three modified blade profiles with the baseline. Total pressure measurements of blade wakes and flow visualization results are also presented. Results from Phase 1 of 2-D linear

cascade testing were analysed to select four additional tubercle shapes, including the two from Phase 1. In Phase 2, pressure sensitive paint (PSP) results are presented along with total pressure wake surveys. Finally, an optimized tubercle geometry was selected and taken to the rotating compressor rig.

Compressor rig testing was conducted to determine and to compare the performance map of the baseline and modified compressors. Results from high-speed pressure transducers at different axial location of compressor are also presented.

4.1 Self-Organizing Maps

Self Organising Map results are explained by finding correlations between geometric and performance parameters. The results from experimental testing of wings with two new tubercle shapes are explained next along with the flow visualization to better understand the flow phenomenon. Finally, the conclusions from updated SOMs are presented including two new data sets. Optimized tubercle amplitude and λ values are predicted based on the complete SOM analysis.

SOM was used to explore the design space of tubercle geometries for multiple parameters and to find a correlation among geometric and performance parameters. Based on the correlation, tubercle geometries were selected that improved the performance of the airfoils test. SOM did not result in a single tubercle geometry, but informed the design of optimal parametric domain.

Experimental data sets were used for performing SOM analysis with different flow conditions and airfoil geometries. SOM were applied to both individual and combined data set for better understanding of the results. The assessed geometric variables: amplitude (A), wavelength (λ), amplitude to wavelength (A/L), tubercle

angle (θ), aspect ratio (Æ) and Reynolds number based on hydraulic diameter Re_{Dh}. The performance parameters were *ClNormalized* ($C_{l,max}$), *StallNorm* (α_s), and post-stall operability area (*PostStallArea*). The bar next to the hexagonal cell shows the range of values from lowest (dark blue) to highest (bright yellow). The SOM results for the combined data are shown in Figure 4.1. Using this as a simple demonstration, tubercle angle and *A/L* are geometrically inversely proportional to each other since it is clear they have perfectly opposite grid colours.

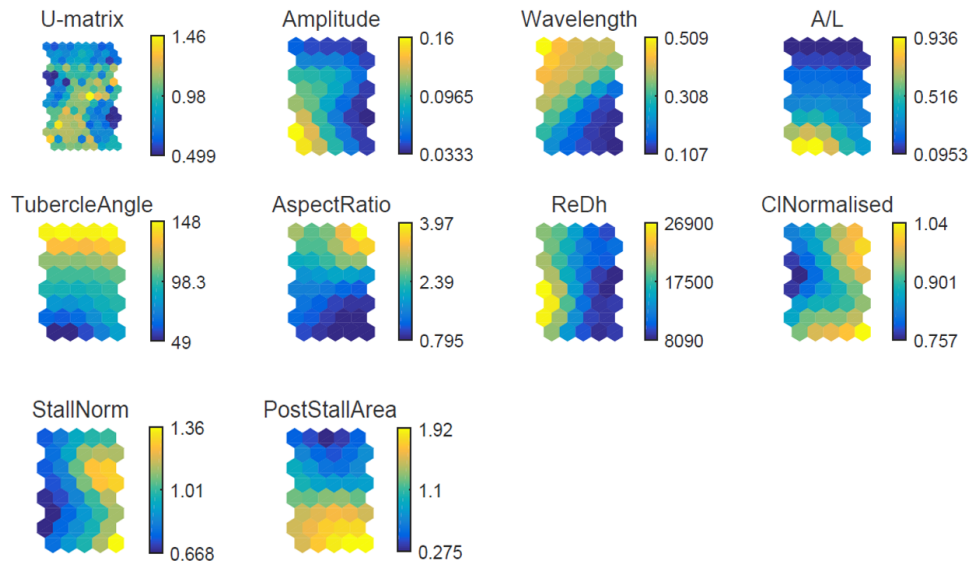Figure 4.1: SOM of combined experimental tubercle data

4.1.1 Reynolds number based on hydraulic diameter (Re_{Dh}) Influence

A new variable, Reynolds Number based on hydraulic diameter Re_{Dh} (see Equation 3.4), is introduced for the first time in this work and normalized α_s (*StallNorm*) is observed to be inversely proportional to it. Re_{Dh} hexagonal cells on the lower left

have the highest values and α_s displays the lowest values in that zone. Similarly, lower Re_{Dh} values on the right side corresponds to the higher α_s values in that zone. However, lower Re_{Dh} values do not translate exactly into higher α_s values. So, it can be concluded that the highest α_s is somewhere in the lower range of Re_{Dh} meaning smaller tubercle size seems to be more effective in delaying stall. It is believed that small and more frequent tubercles result in larger number of SWCRV with optimal strength resisting boundary layer separation.

Normalized Re_{Dh} have a similar, but weaker inverse corelation with normalized $C_{l,max}$ (*ClNormalized*). Dominant yellow on the right side reflects higher values of the normalized $C_{l,max}$, corresponding to the lower normalized Re_{Dh}. Results agreeing with the highest values of normalized $C_{l,max}$ are evident in the lower right corner, similar to the α_s. Re_{Dh} does not display any correlation with the post-stall operability area.

Normalized Re_{Dh} demonstrated clear inverse correlation with α_s and normalized $C_{l,max}$. Lower values of Re_{Dh} indicate improved performance in α_s and $C_{l,max}$ however it can also be observed that the lowest value of Re_{Dh} might not result in best airfoil performance.

4.1.2 Wavelength (λ) Influence

Values of λ varying from 11 to 86% of chord have been experimentally tested. It is a significant range with a limited number of data points. No strong correlation was observed when the λ hexagonal grid was compared with performance parameters. Post-stall operability area is the only parameter that displayed a modest correlation with λ. It can be observed that lower wavelength values correspond to higher post stall operability area, evident in the lower right corner comparison. The lack of data

points with $\lambda < 11\%$c could be the reason why no clear correlation of λ could be established with either α_s or $C_{l,max}$. This is a reasonable conclusion since the lowest λ also corresponded to the highest values for $C_{l,max}$ and α_s.

4.1.3 Amplitude (A) Influence

Amplitude seems to have moderate inverse correlation with the $C_{l,max}$. Colour coding in the A hexagonal grid suggest that the lowest values, around 3%c amplitude (dark blue), did not result in maximum $C_{l,max}$. An A of about 5%c seems to correspond with higher $C_{l,max}$ values, near unity. However, it was not possible to extract the exact values from these plots. Amplitude of around 9%c (light blue) seemed to result in relatively higher $C_{l,max}$ values. Similar A relation can also be observed with α_s: it is clear that amplitude of less than 3%c did not improve $C_{l,max}$, but tubercle amplitudes between 3 and 6%c should be explored. No clear trend between amplitude and post-stall operability area could be established.

4.1.4 Aspect Ratio Influence

The aspect ratio, $Æ\!R$ is a geometric variable introduced in this work (see Equation 3.1) to characterize the local 3-dimensional tubercle-scale flow effects. $Æ\!R$ displayed correlation with neither $C_{l,max}$ nor α_s. But it seemed to have an inverse correlation with the post-stall operability area: here a lower $Æ\!R$ corresponded to higher post-stall operability area improvements, as evident in the lower right corner SOM values. An $Æ\!R < 1.0$ defines an ellipse with its major axis perpendicular to the airfoil span. Tubercles with $Æ\!R < 1.0$ performed better than those with $Æ\!R > 1.0$ in terms of improved post-stall operability. Tubercles have been widely assumed to produce a pair of SWCRV, and are often compared with delta wing phenomena. However, tuber-

100

cle profiles opposite to the delta wing pattern resulted in improved performance in terms of post-stall operability. It is hypothesized that a tubercle shape with $Æ < 1.0$, generates a pair of weaker SWCRV, just enough to prevent or delay stall.

Aamplitude to wavelength (A/L) ratio is another variable similar to $Æ$ and a weak direct correlation can be observed with post stall operability area. Higher values indicating higher A or lower λ can improve performance in post-stall regime. This geometric parameter was not explored further because ot does not seem to have any correlation with any other performance parameter.

4.1.5 Experimental Validation

Following the SOM results, Peristy *et al.*'s work was expanded to test two new tubercle geometries where limited data existed [1]. This extension of experimentation sought to test the tubercle variables at which the SOM were pointing: lower A and λ. Persity *et al.* tested three tubercle geometries in subsonic wind tunnel at RMC and concluded that tubercle A of 6%c and λ of 11%c performed best. A3L11 was the smallest published tubercle experimental data set. Their work was extended to test the newly selected tubercle geometry and to compare it with the best performing geometry (A3L11) and baseline. A3L11 was the best performer in Peristy *et al.*'s work and it provided a good baseline to test and improve tubercle performance.

To clarify ambiguities in the literature, the tubercle amplitude used in this work is the chordwise distance from tubercle meanline to a peak or valley. Thus the distance between the peak and the valley will be 2A. For example an A of 2%c listed here means that the total distance between the peak and the valley is 4%c and it is important to note that A of 2%c is equivalent to 4%c used in the SOM work i.e. A2L7 and A2L9 tubercles.

101

Table 4.1: Tubercle geometric parameters for the three tubercled airfoils tested at $V_a = 7.5\ m/s$

Tubercle	Amplitude $A[\%c]$	Wavelength $\lambda\ [\%c]$	Re_{Dh}	$\cancel{R}$
A3L11	3	11	4620	0.73
A2L7	2	7	3360	0.5211
A2L9	2	9	3970	0.6866

SOM results indicated that an *A* in the range of 2 to 4%c needed to be explored. The lowest λ value of 11%c resulted in maximum post-stall operability area improvement, so values lower than 11%c also needed to be investigated. Since this work sought the optimal geometry, tubercle shape was selected based on these results to experimentally explore the unknown regime. Results for newly introduced geometric parameters Re_{Dh} and $\cancel{R}$ were also included when defining a new tubercle shape. Normalized Re_{Dh} and $\cancel{R}$ has shown inverse correlations with α_s and $C_{l,max}$. Thus these geometric parameters were further reduced from A3L11.

So a new tubercle shape with an *A* of 2%c and wavelength of 7%c (A2L7) was selected and a new wing manufactured using the procedures followed by Peristy *et al.* [1]. Under the same flow conditions, A2L7 was tested in the wind tunnel at three different Re_c. Results from experimental testing are presented here and, based on the results from A2L7, it was decided to determine the influence of tubercle wavelength. Therefore another tubercle geometry with *A* of 2%c and λ of 9%c (A2L9) was designed and tested. Geometric parameters of the three tubercle geometries compared for the validation of SOM results are compiled in Table 4.1.

4.1.5.1 Results for Re_c of 75×10^3

Results for three tubercle shapes tested at Re_c of 75×10^3 are shown in Figure 4.2. The new tubercle geometries did not show any improvement over the baseline nor over A3L11, when compared with the baseline airfoil, A2L7 did improve α_s from 12° to 14°, as A3L11 did. This did not persist in A2L9, which had higher λ values than A2L7. A2L7 improved α_s over A2L9, but otherwise they performed very similarly in the pre-stall regime. Maximum $C_{l,max}$ values were signifantly reduced with maxima just near 0.7, compared to the baseline's and A3L11's 0.9. A2L7 and A2L9 showed improvement in the post stall operability area and both airfoils stalling very gradually. However, the performance improvements were considerably greater for the A3L11 tubercled airfoil.

4.1.5.2 Results for Re_c of 150×10^3

The experimental results of a baseline and tubercled airfoils at Re_c of 150×10^3 are shown in Figure 4.3 where it can be observed that the A2L7 delayed α_s over A3L11 but did not meet the higher α_s of 16° of the baseline airfoil. It is interesting to note that A2L7 maximum $C_{l,max}$ plateaued at an α of around 11° and stayed there with only slight fluctuations until α reached 15° indicating resistance to stall by tubercles. A3L11 stalled at lower α, but near $\alpha = 13°$ achieved a $C_{l,max}$ of 0.98 that was higher than baseline.

A2L9 improved $C_{l,max}$, over A2L7 achieving a value of 0.8, however it stalled earlier at an angle of 14°. The $C_{l,max}$ gap between A2L9 and the baseline also decreased somewhat with the higher Re_c of 150×10^3 and A2L7 seems to have stalled stepwise with initial C_l at an α of 15° followed by another decline after $\alpha = 20°$. Whereas
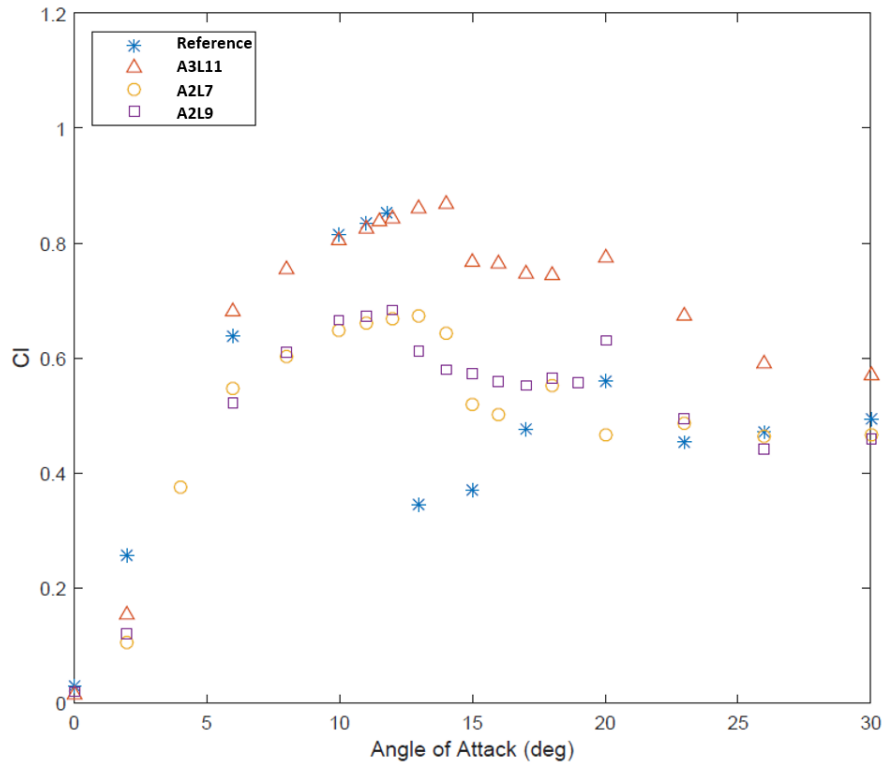
Figure 4.2: Experimental results of tubercled *vs* baseline airfoils at Re_c 75×10^3

A2L9 improved $C_{l,max}$ its stall was more abrupt. Neither A2L7 nor A2L9 were able to match or outperform A3L11's performance in the pre-or post-stall regimes.

A curious feature of the post-stall regime for tubercled airfoils is the presence of multiple quasi-steady-state values of C_l for various α. This multi-mode stall phenomenon was observed only for tubercled airfoils. It was first observed and reported by Peristy *et al.* who employed electronic static pressure transducer but also a water manometer. At α_s, C_p values were seen to fluctuate between multiple quasi-steady-state points. The effects of this phenomenon are very clear in post-stall at α of 23 and $26°$ for tubercled airfoils in Figure 4.3. No such phenomenon was noticed in the un-
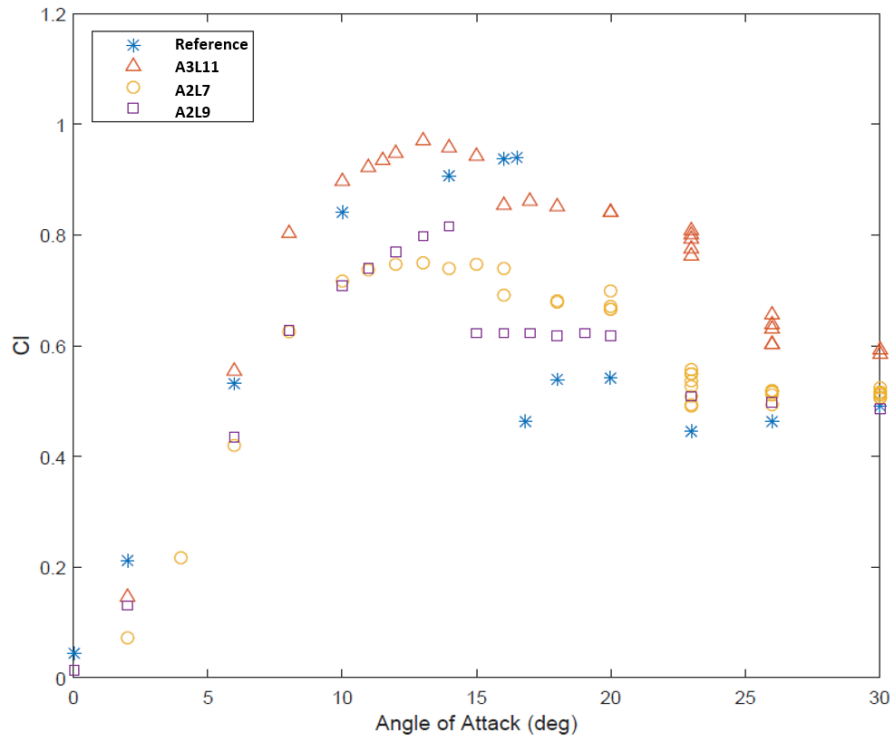
Figure 4.3: Experimental results of tubercled *vs* baseline at Re_c 150×10^3

modified baseline testing. All connections and equipment were verified to ensure the multimode stalled airfoil was not an artifact of experimental method. Fluctuations were steady enough to allow recording of multiple values and so they were not a result of high frequency, single point fluctuations, which were attributed to multi-mode stall characteristics seen by other researchers, including Peristy *et al.* [1].

4.1.5.3   Results for Re_c of 300×10^3

The results for all airfoils at a Re_c of 300×10^3 are shown in Figure 4.4. Where the trends observed in the Re_c of 150×10^3 tests were still evident, the $C_{l,max}$ gap between A2L7 and A2L9 was significantly reduced. The baseline airfoil reached
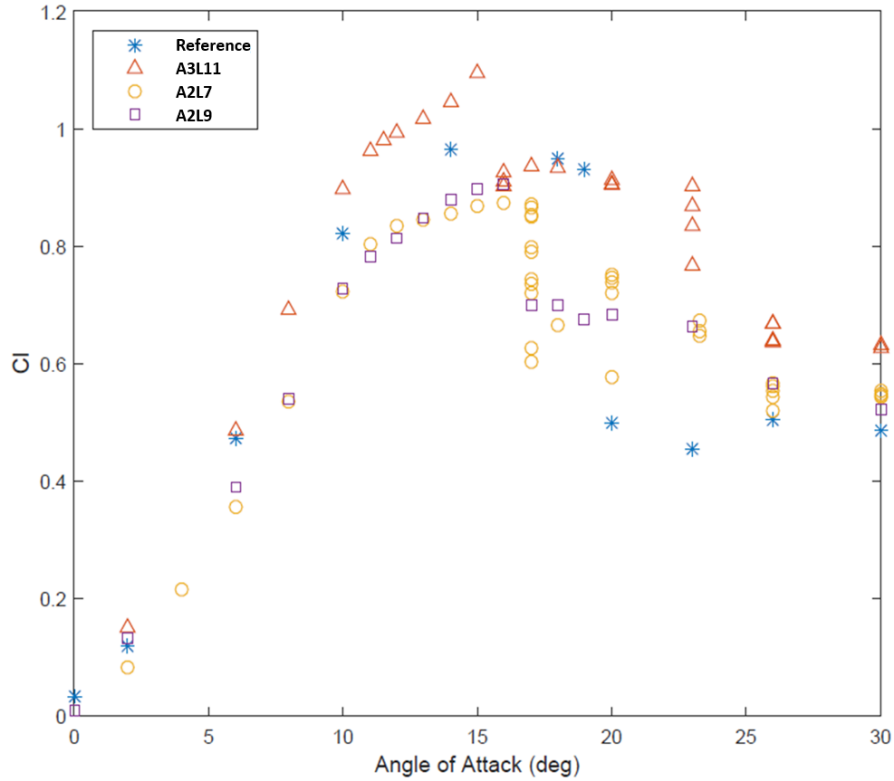
Figure 4.4: Experimental results of tubercled *vs* baseline at Re_c 300×10^3

a slightly higher $C_{l,max}$: 0.96 up from 0.87, compared to 0.9 for A2L7 and A2L9. A2L9 stalled at $\alpha_s = 16°$ with A2L7 slightly improved at $\alpha = 17°$. A3L11 stalled earlier than the other test airfoils but the performance did not drop below that of the baseline, even after stall. The baseline airfoil had the highest α_s of 19°. The multi-mode stall phenomenon was also observed for this Re_c: A2L7 showed multi-mode stall at the point of stall, as opposed to what was observed earlier in the post-stall regime (Figure 4.3). Curiously, the A2L9 airfoil did not exhibit any multi mode stall characteristics. While the A3L11 airfoil had at multiple C_l at α_s, A2L7 and A2L9 performed the same in terms of post stall operability area improvement. Once again,

106

the A3L11 airfoil performed significantly better than all other airfoils, including the baseline. A3L11 stalled at a lower α, but retained its post-stall performance along with a pre-stall performance better than the other airfoils. The $C_{l,max}$ achieved by the A3L11 airfoil was notably significantly higher than that of the baseline.

4.1.5.4 Flow Visualization Results

In an effort to understand tubercle behaviour and flow characteristics, oil flow visualization was performed on the A3L11 and A2L9 tubercled airfoils at a Reynolds number Re_c of 150×10^3 and at α of $15°$. The oil was mobilized in the flow due to the presence of alcohol that evaporated during the tests, capturing the oil flow features, while video was recorded under a UV light.

Figure 4.5 shows flow visualization results for the A3L11 airfoil, revealing the strong SWCRV downstream of tubercle peaks. Oil moved from tubercle peaks and collected downstream of the valleys, annotated by the black arrows in Figure 4.5. This oil collection indicates the presence of a separation bubble downstream of the valley, while no flow separation can be seen downstream of the peaks. Flow was mobilized downstream of any peak, as evident in the bifurcated oil patterns between the two annotated black streamwise lines in Figure 4.5. However, weak mobilization of flow was observed downstream of any valley, in the area between the annotated black and red streamwise lines in Figure 4.5. Mobilized oil flow downstream of tubercle peaks indicated that the SWCRV forced the flow to remain attached. This was observed to persist longer downstream of a peak, and tended to detach earlier downstream of a valley. This is explained by higher curvatures and greater local adverse ΔP in valley regions. A secondary effect of this phenomenon is the tendency of tubercles to act as flow fences, impeding spanwise flow separation. The solid

green line along the span in Figure 4.5 shows the approximate chordwise distance to which oil mobilization was observed.
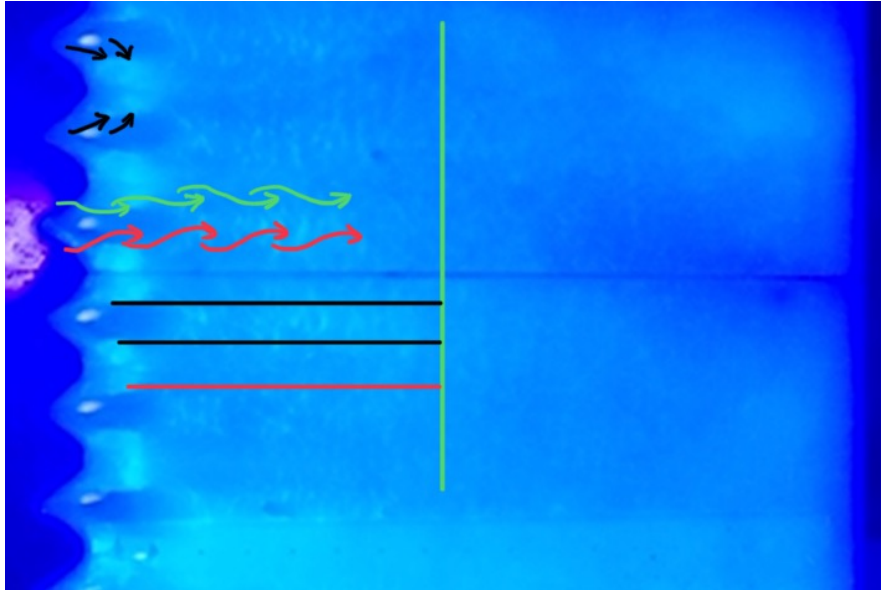
Figure 4.5: A3L11 suction surface flow vizualization at $\alpha = 15°$ and Re_c of 1.5×10^5

Flow visualization for A2L9 is shown in Figure 4.6 where similar flow patterns to A3L11 were observed. Flow was completely swept from the peaks, collecting behind tubercle valleys. The red and green arrows in Figure 4.6 show the direction of SWCRV downstream of a representative peak. Oil is gathered downstream of tubercle valleys which is expected to be the site of a laminar separation bubble. Weak SWCRV are suspected due to the slow mobilization of oil as compared to that observed for A3L11 in Figure 4.5. Weak SWCRV were sufficient to create bifurcation of oil evident downstream of the peak in Figure 4.6. Stream-wise oil patches, outlined in red in Figure 4.6 can be seen downstream of tubercle peaks indicating local separated flow. Oil was observed to be mobilized for about the same chord length as it was for A3L11, but mobilization was comparatively restricted.

108
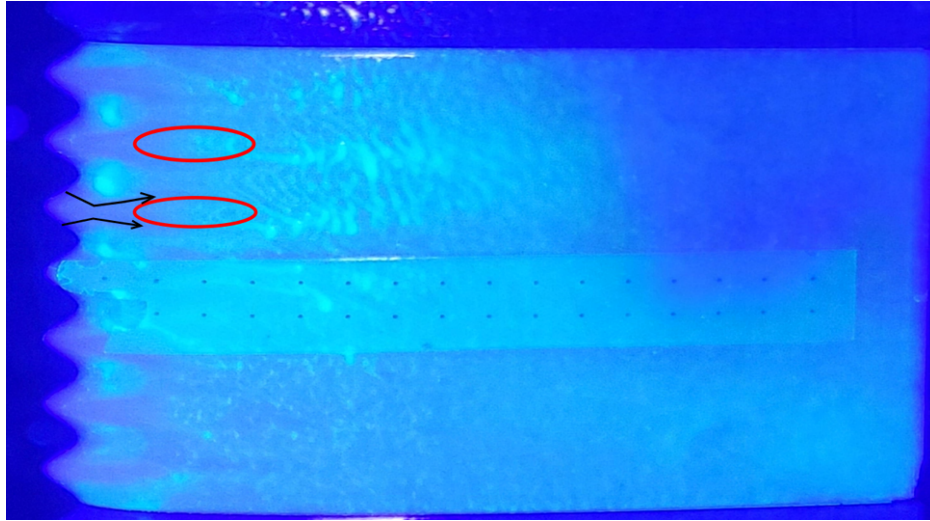
Figure 4.6: A2L9 suction surface flow vizualization at $\alpha = 15°$ and Re_c of 1.5×10^5

From the experimental testing and flow visualization, the characteristic presence of SWCRV downstream of tubercled leading edges can be confirmed, however, their strength and interaction varied from one tubercle shape to another. Flow visualization and C_l *vs* α results both revealed that the A3L11 profile generated more suction by creating stronger SWCRV. The difference between A2L9 and A3L11 is a reduced tubercle amplitude and wavelength for A2L9. It is suspected that for A2L9, either weak SWCRV were being generated or they were in relatively close proximity, possibly interacting with each other. Tubercle amplitude is believed to generate SWCRV whereby wavelength determines the distance between two SWCRV. Greater amplitude can result in stronger SWCRV, however $Æ$ and Re_{Dh} influence the separation point of flow from the tubercle peak, thereby generating SWCRV.

4.1.6 Updated SOM Results

Subsequent to the single airfoil wind tunnel results, two new tubercle geometries were tested, with a primary objective of analyzing and selecting promising tubercle shapes for implementation in the transonic compressor cascade. SOMs were updated with the new experimental data sets and results are presented in Figure 4.7.
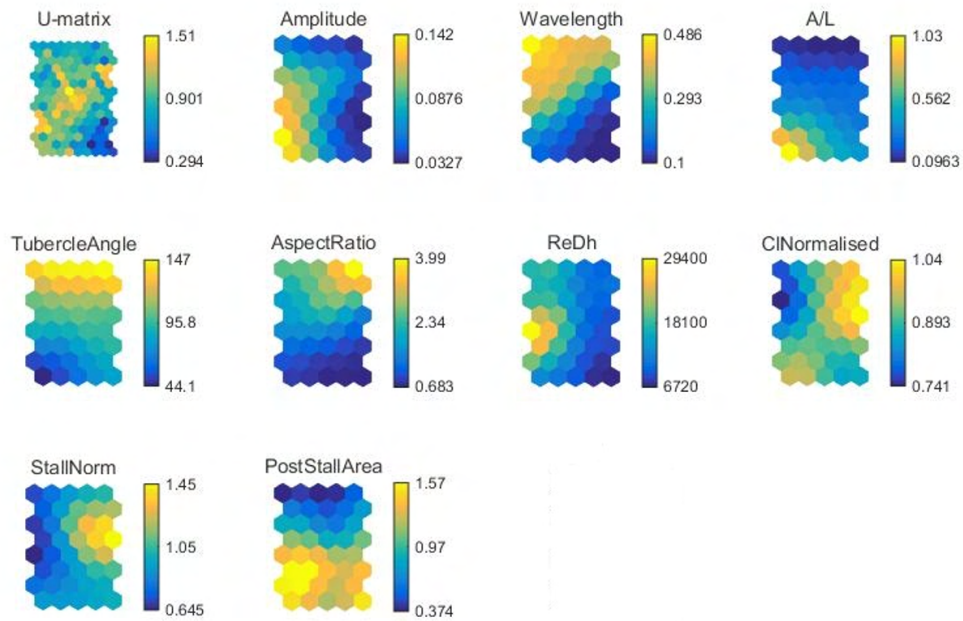
Figure 4.7: SOM of updated experimental tubercle data

Here amplitude still displayed a weak inverse correlation with the $C_{l,max}$ but it seems clear that contrary to the prior hypothesis, the lowest amplitude did not improve the $C_{l,max}$. It was also shown in experimental results that an amplitude less than 6%c did not improve airfoil performance. In this work, values of λ lower than 11%c were explored to fill an experimental gap and to fully explore any correlations between λ and α_s over $C_{l,max}$. Tubercle wavelength λ still appeared to have inverse

correlation with post-stall operability area but values less than 11%c did not seem to have any positive effect. Similarly, Re_{Dh} demonstrated an inverse correlation with α_s but as before, the highest α_s did not correspond with lowest Re_{Dh}. It is clear that the configuration with highest Re_{Dh} resulted in the poorest performing α_s. Re_{Dh} values in the lower range of around 10^4, can result in optimized tubercle airfoil performance for α_s. Tubercle Æ also had a similar inverse correlation with post-stall operability area.

Delta wings are designed on the principles of abrupt flow separation generating characteristic vortex pattern on the suction surface. Aspect ratio analysis also indicated that the tubercles do not perform like delta wings. Based on the tubercle literature survey and the work performed, it was clear that tubercles form a pair of SWCRV on their suction surfaces without abruptly separating the flow on a large scale. Tubercles require a smooth transition from the leading edge to the suction surface. Tubercles give rise to SWCRV that gently provide enough strength to vortices to inject the freestream flow into the boundary layer delaying its separation. Tubercle-generated SWCRV do not have enough strength to persist downstream of the trailing edge and they dissipate earlier. Vortices are not expected to significantly affect the wake of the airfoil.

A final summary of SOM results has been compiled in the Table 4.2 comparing peformance parameters with the new geometric parameters introduced in this work.

From SOM analysis conclusions were made that A around 3%c and λ around 11%c would provide an approximate optimized tubercle geometry. This was decided taking into account all three performance parameters (α_s, $C_{l,max}$ and Post stall operability area). In the next phase of optimization, 2-D cascade testing of multiple tubercle geometries was undertaken as would be expected before any 3-D testing.

111

Table 4.2: Final summary of the the combined results of the SOM plots

	Re_{Dh}	A [%c]	λ [%c]	$\mathbb{R}$	Tubercle angle	$\frac{A}{\lambda}$
Normalized α_s ↑	Strong ↓	Moderate ↓	—	—	—	—
Normalized C_l,max ↑	Moderate ↓	Moderate ↓	—	—	—	—
Post-stall operability area ↑	—	—	Strong ↓	Strong ↓	Weak ↓	Weak ↑

The next section details the results of the range of tubercle geometries tested and the final determination of tubercle geometry for 3-D testing.

4.2 Linear Cascade Testing

Compressor linear cascade testing was performed in two phases: one involved selection of an initial set of tubercle shapes on which wake surveys and flow visualization were conducted. In Phase 2, new tubercle shapes were selected, including the best performing geometries from Phase 1 or from Wind tunnel tests, and secondly more stiffer 3-D printing material was used. Wake total pressure surveys were performed as in Phase 1 but flow visualization was not. Pressure sensitive paint was used in Phase 2 to characterize better suction surface flow at higher incidence angles.

4.2.1 Linear Cascade Testing Phase - 1

4.2.1.1 Tubercle Shape Selection

Two conventional sine wave shapes were selected and thirdly, a power series tubercle geometry was added based on the optimization of Levert-Beaulieu *et al.* [72]. The

Table 4.3: Geometric parameters for tubercle geometries for phase 1 compressor cascade testing

Profile	Amplitude $A[\%c]$	Wavelength $\lambda\ [\%c]$
Baseline	0	0
A2L9	2	9
A3L11	3	11
PSA3L11	3	11

PSA3L11 tubercle shape had the same A of 3%c and λ of 11%c, but the tubercle shape was defined using a power series curve of 0.2, as detailed in Levert-Beaulieu *et al.*'s work. Table 4.3 summarizes the parameters of three selected geometries, with baseline and tubercle profiles shown in Figure 4.8.

4.2.1.2 Wake Surveys

Wake surveys evaluated total pressure loss in the wakes downstream of cascade compressor blades. A traverse scanned the wake from the pressure side of the middle blade to its suction side (about 12 mm = $\frac{1}{2}$ pitch), synchronized with the wind tunnel operation. The traverse was triggered using a *Kulite* pressure transducer when vacuum pressure was sensed. Wake surveys were performed for all four blade profiles for an angle of incidence (AOI) range from 0 to 10° in increments of 2°.

The results for the baseline blade wakes are shown in Figure 4.9 where it can be seen that the wake for 2 and 4° AOI is smaller than for 0°, that itself is similar to the $AOI = 6°$ wake. Wake was measured using the *Aeroprobe* which has the uncertainity in measurement of about ±0.0001 or 0.01% smaller than all wake differences. Minimum total pressure loss for the baseline compressor profile was observed at 2° AOI followed by $AOI = 4°$. These results were expected since compressor blades are designed for such conditions. The results also agree, in general, with the study

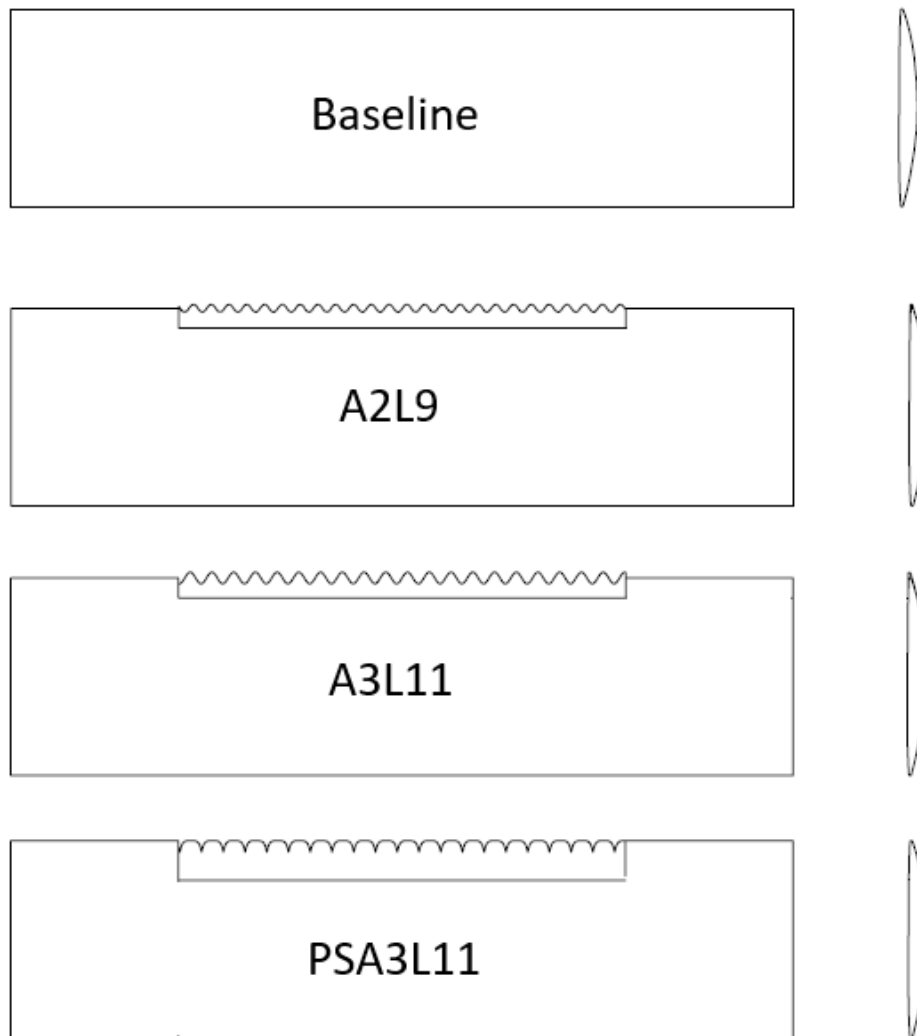Baseline

A2L9

A3L11

PSA3L11

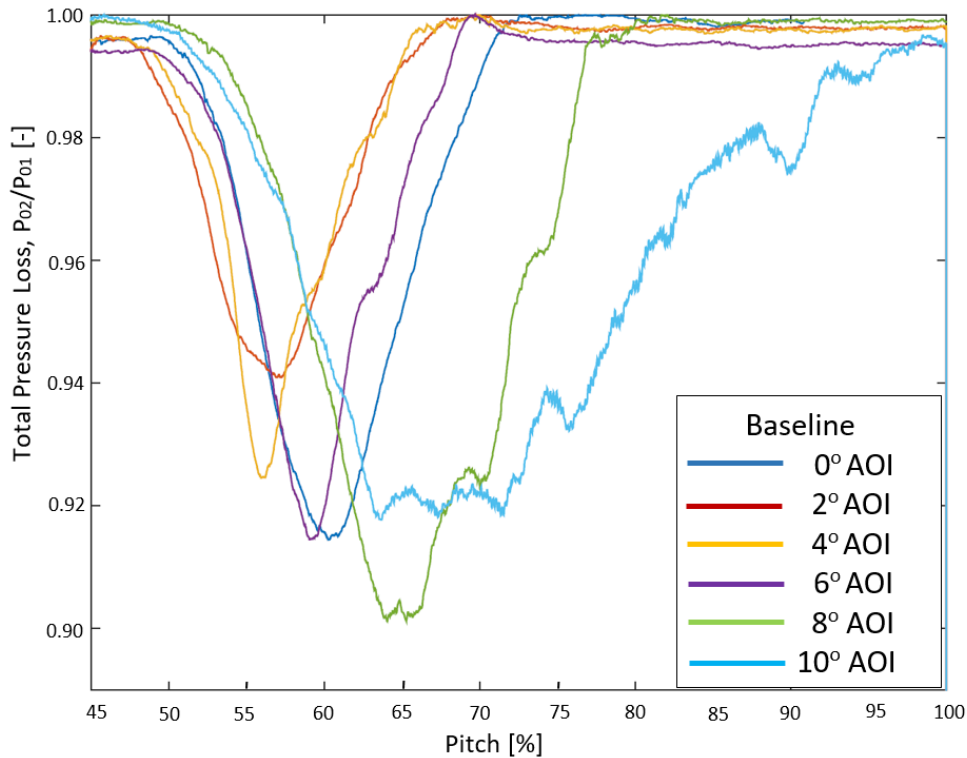Figure 4.8: Four compressor blade planform (left) and profile (right)

Figure 4.9: Baseline wake survey

performed by Lieblein for NACA $65(A_{10})$ series blades [82]. Figure 4.9 shows that the baseline compressor blade stalled at $8°$ and a coincident, significant flow passage blocking was evident, in a widened and deepened wake. By $10°$ AOI, the blade had completely stalled and the wake spanned almost half a pitch, which was 22.8 mm.

Compressor blades are also designed for exit wake angle due to the interaction with the downstream blade rows. So it was considered important to compare exit flow angles for all four compressor blades at $0°$ AOI. For the purposes of comparison in this work $0°$ AOI was considered the design point. The comparison of wake profiles between all four compressor blade profiles at $0°$ AOI is shown in Figure 4.10,
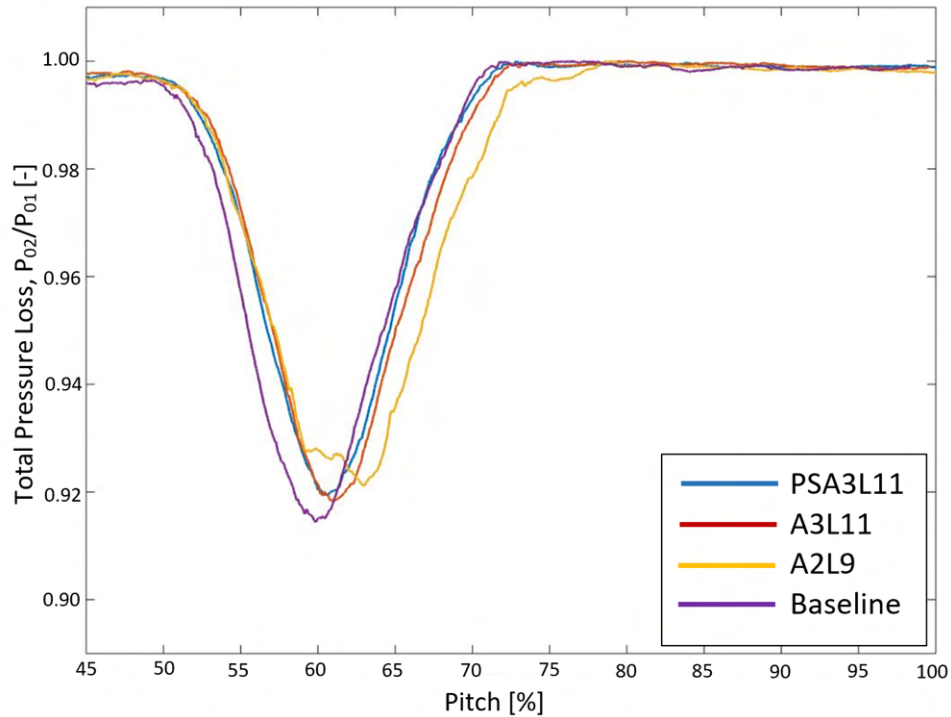
Figure 4.10: Blade wake comparison for all 4 blade geometries at AOI = 0°

where they seem to have similar wakes with only slight differences in their suction surface wake. The A2L9 tubercled compressor blade had a slightly wider wake when compared to the other two tubercled and to the baseline blades. It is clear from the 0° comparison that compressor blade performance at design point is not compromised by tubercles.

Wake angles were assessed to ensure no compromises are being made elsewhere with the use of tubercles. The exit flow angles of all four compressor blades are compared in Figure 4.11. The baseline compressor blade reached a negative AOI angle of $-10°$ and passage flow angle was consistently around $10°$. The exit flow angle of the tubercled blades A3L11 and PSA3L11 reached negative incidences of

116
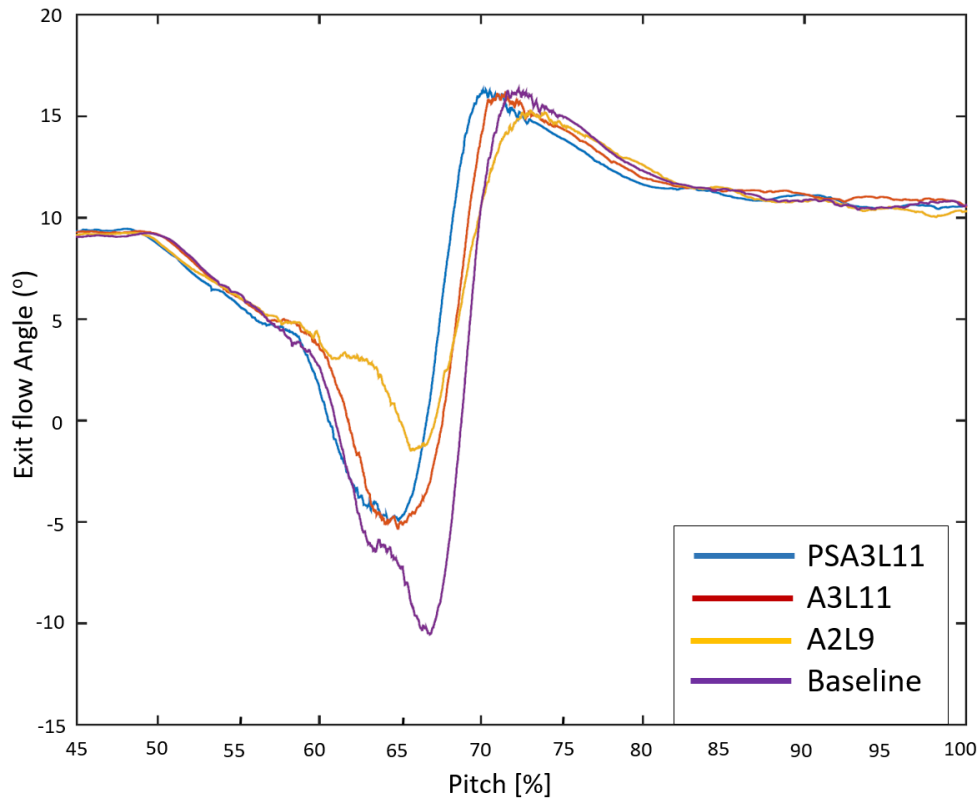
Figure 4.11: Exit flow angle comparison for all 4 blade geometries at AOI = 0°

$-5°$ whereas A2L9 reached just $-2°$. On the suction side of the wake, similar angles of around $16°$ were observed for all four blades.

Compressor blade wake results were analysed for all the angles but wakes were found to be very similar from AOI of 0 to 8°. Wakes for AOIs 2, 4 and 6° are shown in Appendix because their results were very similar. At 8° AOI, blades were assessed to have stalled when significantly wider wakes were observed, as shown in Figure 4.12. The tubercled A3L11 and PSA3L11 blades had narrower wakes than the baseline did. At 8°, the PSA3L11 blade wake was even finer, as if the tubercles eliminated compressor blade stall. The tubercled A2L9 profile performed similar to

117
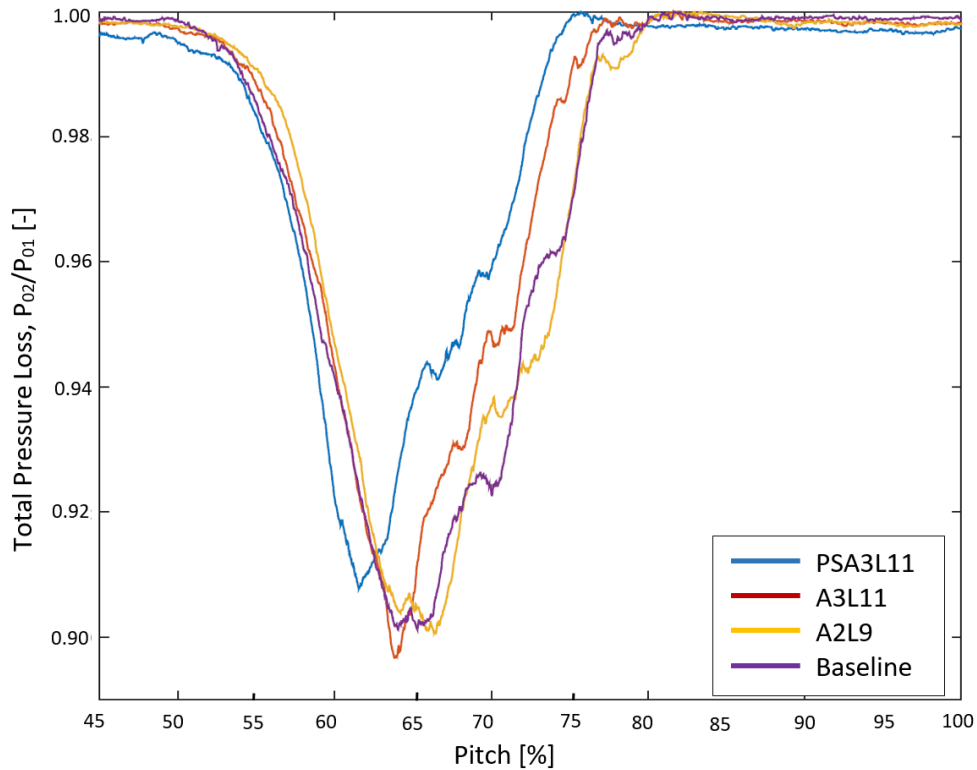
Figure 4.12: Blade wake comparison for all 4 blade geometries at AOI = $8°$

the baseline, with only minor differences.

On the suction side of the blade wakes (right hand side in Figure 4.12), a oscillating pitchwise pattern is clearly evident for all four compressor blade profiles except at $0°$ AOI. Recall that the compressor profiles were thin and some minor blade deflections under load were observed using high speed video, however no evidence of vibration was detected. This can be improved in the future by designing the compressor cascade for a larger transonic wind tunnel. Bigger cross-sectional area of compressor cascade will enable the testing of physically larger and stronger compressor blades. The increased volume will allow for static pressure ports which will

118
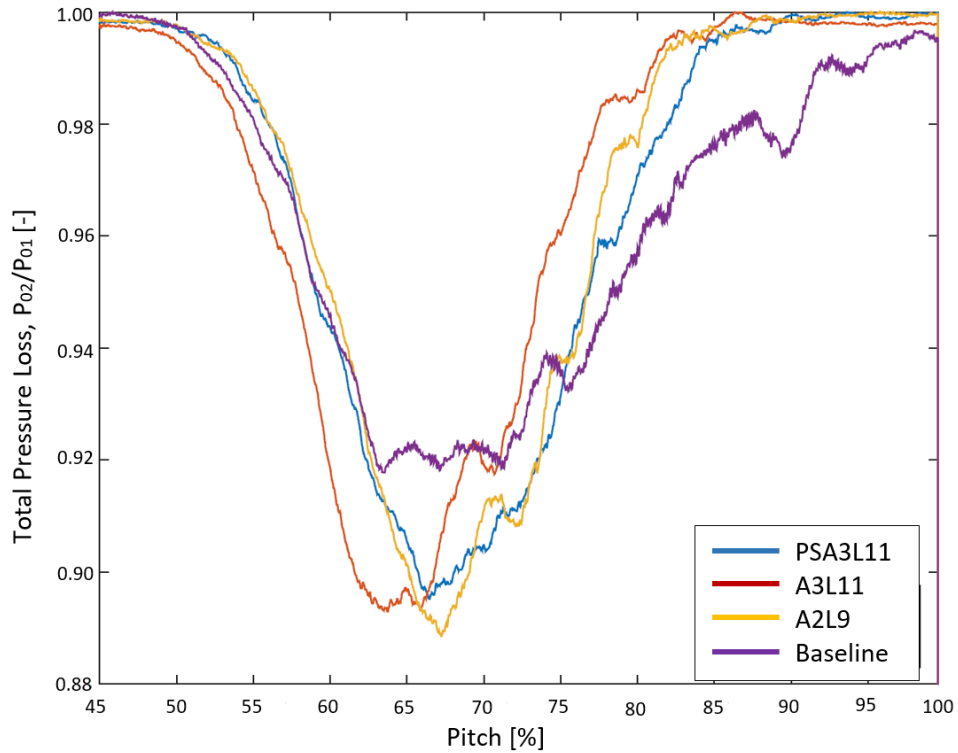
Figure 4.13: Blade wake comparison for all 4 blade geometries at AOI = 10°

enhance compressor instrumentation.

At 10° AOI, the baseline compressor blade had stalled and can be observed to be blocking more than half of the pitch shown in Figure 4.13. The tubercled blades were also stalled, but apparantly in a more controlled fashion. The A3L11 tubercle profile seemed to have the least total pressure loss, a result that is in line with other experimental work. Tubercled blade stall is much more gradual and usually delayed, as compared to baseline stall. In this work, wakes from the tubercled blades were deeper and more concentrated when compared to baseline wakes. It is suspected that the formation of SWCRV from the tubercles resulted in higher total pressure loss but

they apparently prevented full stall formation, resulting in a narrower, deeper wake and minimal passage blockage.

4.2.1.3 Cascade Losses

Total pressure measurements were used to compare the performance of compressor blade geometries. A tubercle geometry informed from 2-D compressor cascade results was used for 3-D compressor experiments. The compressor wake mixed-out loss calculations were not performed in this work. Instead, the cascade was designed with a five-hole probe about 2/3rd axial chord downstream of the blade row to ensure that wake mixing had already occurred.

From the wake survey analysis, total pressure loss coefficient (γ) shown in Equation 4.1, was used for comparison of the three tubercled blades with the baseline.

$$\gamma = \frac{P_{01} - P_{02}}{P_{01} - P_{1s}} \tag{4.1}$$

where, P_{01} is the total pressure at cascade inlet, P_{02} is the total pressure at cascade exit and P_{1s} is the static pressure at cascade inlet.

Figure 4.14 displays results for all six AOI and for all four compressor blade profiles. Measurement uncertainities were calculated and they are well within the marker size. A full uncertainty analysis can be found in Appendix C.1. Tubercle profiles performed better than the baseline, even at off-design AOI. PSA3L11 tubercled blade consistently outperformed the baseline and other tubercled blades at almost all AOI, with notable improvements at 8° AOI. However, it did not perform better than the other two tubercled airfoils at 10° AOI. A3L11 was another profile that seemed to consistently outperform the baseline. A2L9 did not perform better

than baseline at most of the lower AOI but loss coefficient reduced at higher AOI. From these reults, it was concluded that the PSA3L11 performed the best of all three test airfoils, with all tubercled blades performing better than baseline at higher AOI. Total pressure loss coefficient values were compared to the study by Lieblein [82]. They were generally lower, but the trend of increased total pressure losses at higher AOI was similar. The difference may be the different blade geometries and the percentage of pitch considered for wake calculation. For this work, the full total pressure measurement was considered for wake calculation due to the different wake widths, especially at higher AOIs. This was considered important to remain consistent in performing these calculation to avoid any variability from one blade to another, since wake comparison was the primary objective.
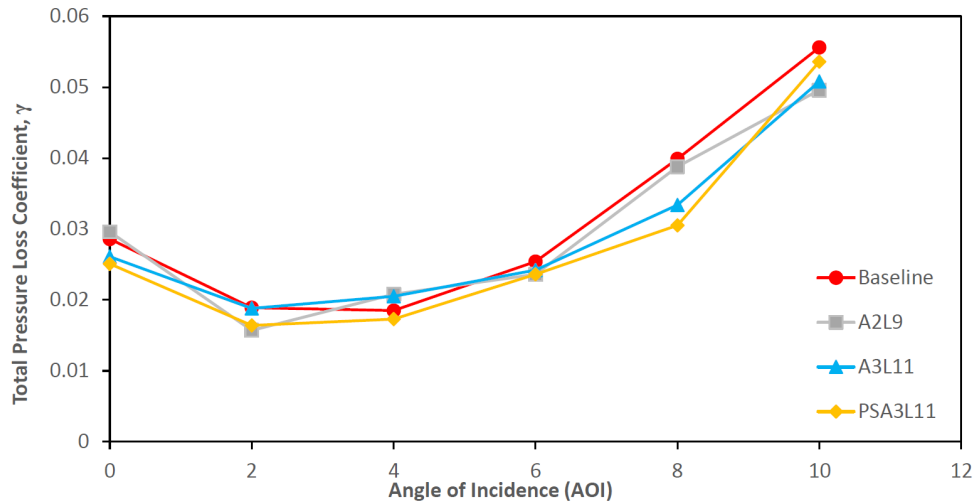

Figure 4.14: Compressor cascade loss coefficient

4.2.1.4   Surface Flow Visualization

To better understand the effects of tubercle shape on stall behaviour, surface oil flow visualization was performed at 8° AOI, where stall had first been observed. It was also where tubercled airfoils were able to suppress stall, whereas the baseline profile was stalled by this point. Flow visualization of the baseline blade suction surface at 8° AOI is shown in Figure 4.15. The suction surface clearly demonstrates the immobilized oil spots downstream of the annotated $\frac{x}{c} \approx 0.2$ black line, illustrating that the blade has stalled. Upstream of the $\frac{x}{c} \approx 0.2$ location, no oil can be seen, since it had been swept downstream to the separated region by the attached flow. Figure 4.16 shows the baseline compressor blade suction surface with a greater quantity of oil on the suction surface. Several non-streamwise oil deposits can be seen downstream of the separation line at $\frac{x}{c} \approx 0.2$, indicating completely separated flow.

Flow visualization results for tubercled airfoils are shown in Figures 4.17, 4.18, and 4.19 where they were all observed to delay stall point to chordwise downstream locations of approximately x≈ 0.4%c, x≈ 0.5%c and x≈ 0.6%c respectively.

Higher AOI for tubercled profiles led to the generation of SWCRV, believed to be stronger with increased AOI. The generation of SWCRV led to a unique flow phenomenon whereby these vortices delay flow separation downstream of the tubercle peaks, but not behind the tubercle valleys. This phenomenon led to the generation of fluidic flow fences along the blade span.

Shown in Figure 4.17, oil flow visualization of the A2L9 tubercle blade suction surface at $AOI = 8°$ clearly demonstrates that SWCRV are being generated from each tubercle. In the suction surface flow upstream of separation point, oil streaks originating from each tubercle shape can be observed. These oil streak cores di-
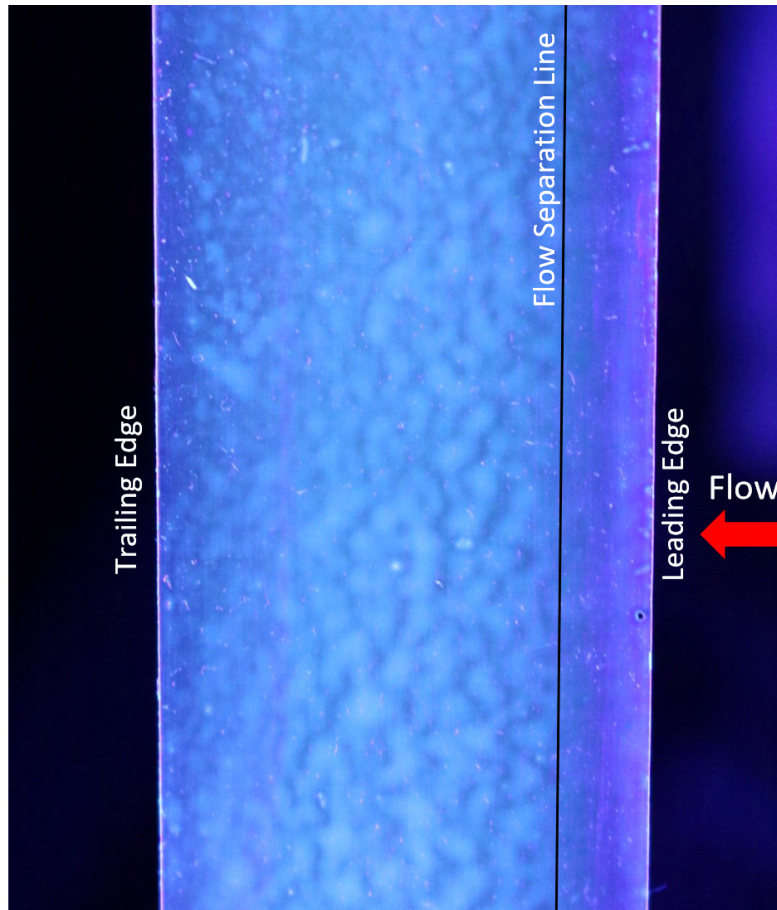
Figure 4.15: Oil flow visualization for the baseline blade suction surface at AOI = 8°

verge as one moves along the blade chord, ultimately interfering with the ones from adjacent tubercles and weakening each other. The annotated circle in Figure 4.17 highlights this. These oil streaks are observed to demolish each other shortly downstream of $\frac{x}{c} \approx 0.4$, annotated by the solid black line. It is believed that the interaction of SWCRVs from adjacent tubercles enhances the effectiveness of the tubercle shape. The SWCRV energize the boundary layer, clearly displayed by the mobilized oil and in delayed compressor stall. Chord-wise strips of undisturbed oil can be seen leading

Figure 4.16: Off axis view of oil flow visualization for the baseline suction surface at AOI = 8°

Figure 4.17: Off axis view of oil flow visualization for A2L9 suction surface at AOI = 8°
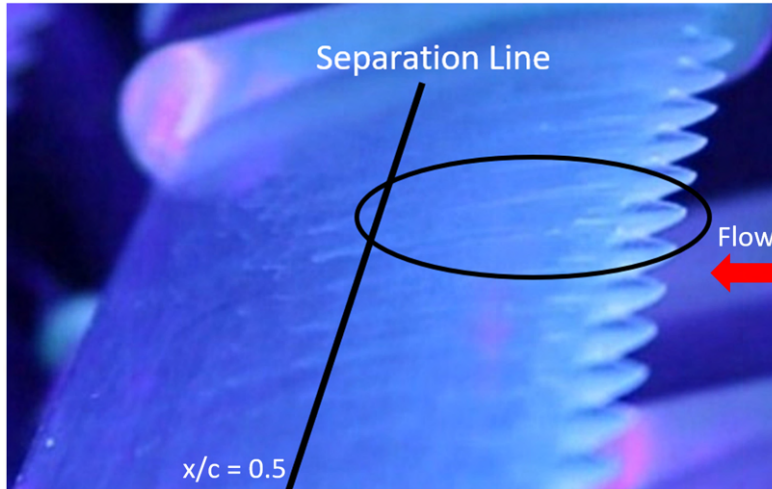
Figure 4.18: Off axis view of oil flow visualization for A3L11 suction surface at AOI = 8°

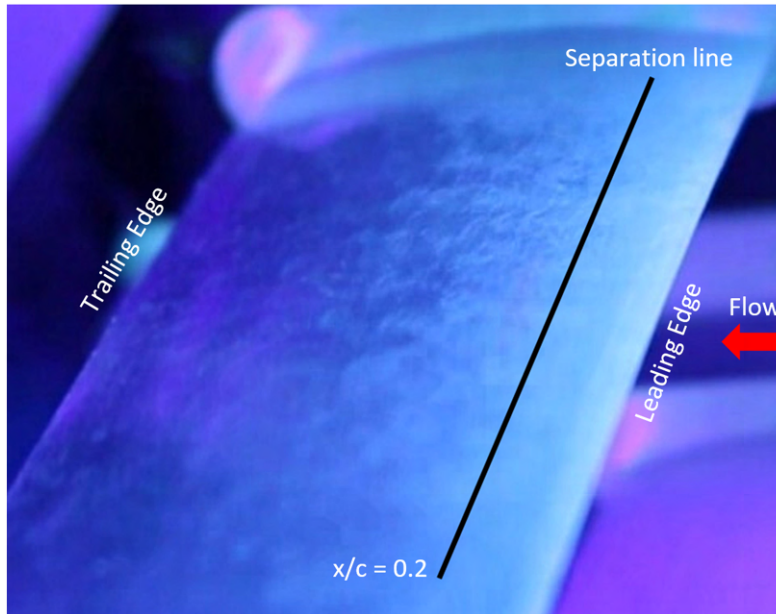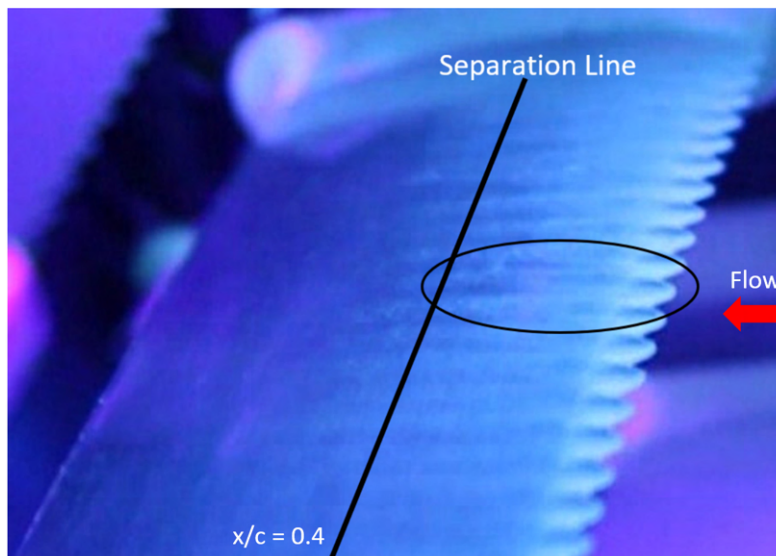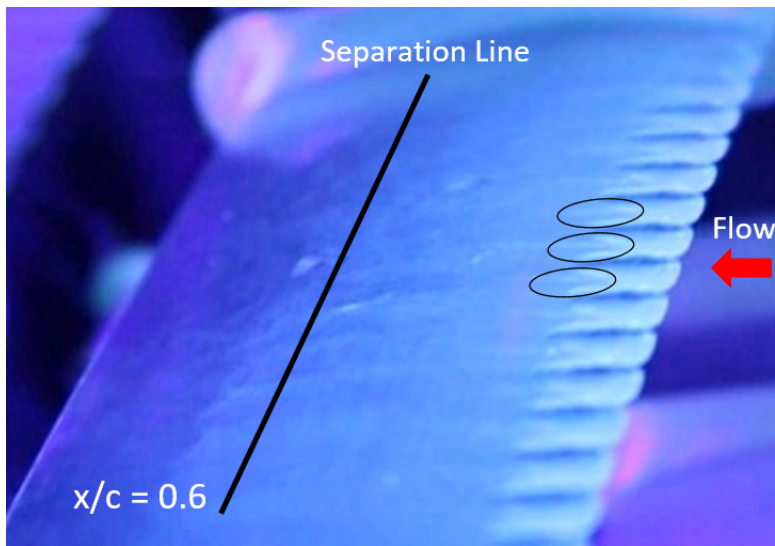Figure 4.19: Oil flow visualization for PSA3L11 suction surface at AOI = 8°
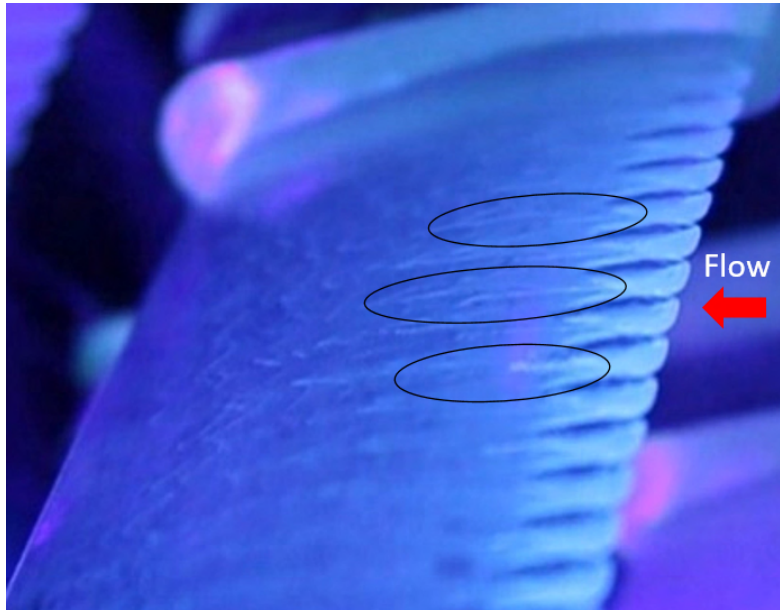
Figure 4.20: Oil flow visualization for PSA3L11 suction surface at AOI = 8° (lower oil quantity)

out of tubercle valleys in Figure 4.17 indicating separated flow. This phenomenon, called compartmentalization first proposed by Fish and Lauder [83] prevents blade stall from spreading spanwise along the blade. These SWCRV travel further apart from one another as they progress along the blade chord, eventually encountering adjacent vortices from an adjoining tubercle.

The interaction of SWCRV from adjacent tubercles is dictated by the Re_{Dh} and λ because these geometric parameters describe the proximity of tubercles. Tubercle amplitude A influences the strength of vortices being generated and it is believed that this can result in destructive interference of adjacent vortices, negatively influencing the flow on the suction surface. When compared to A3L11 and PSA3L11, due to the lower λ of the A2L9 tubercle profile, more tightly spaced tubercles result in earlier

interference of SWCRV generated by adjacent turbercles.

The oil flow visualization of A3L11 tubercle blade is shown in Figure 4.18. Compared to A2L9, A3L11 has relatively fewer tubercles for the same span meaning that SWCRV being generated were spanwise further away from each other. The increased strength of SWCRV due to the increased A might have resulted in better boundary layer energization. It can be seen that flow stayed attached longer chordwise, reaching x$\approx 0.5\%c$. During the analysis of high speed video, it was observed that the flow seems to be mobilized even until $0.7c$. It was clearly seen in Figure 4.18 that oil was smoothly swept downstream for a longer distance.

Reseachers have primarily studied tubercle shape based on sine waves, so flow phenomenon generated by power series profiles is largely undocumented. The PSA3l11 profile is an unconventional approach to tubercle shape since power series profiles are essentially elongated tubercle peaks and narrower, steeper tubercle valleys. In basic terms, PSA3L11 is a straight leading edge with narrow valleys at intervals. It is also very interesting that PSA3L11 had lower total pressure losses at pre-stall AOIs out of three tubercle shapes tested. It is believed that SWCRV are still being generated from the tubercle valleys but they are further apart from their adjacent pair of SWCRV. The SWCRV can potentially travel longer downstream of the blade delaying stall than those generated by the more conventional, sinusoidal tubercles shown in Figure 4.21. Stronger SWCRV support flow behind the straighter peak leading edge. This is evident from flow lines behind the flat peak tubercle regions in Figure 4.19. Moreover, the valleys where the flow is known to separate first, are narrower, giving rise to a greater degree of attached flow on the cascade suction surfaces. It seems that the PSA3L11 efficiently managed the SWCRV to delay stall. It is also suspected that the vortices generated by one valley were not strong enough to allow

the flow to remain fully-attached over a single tubercle with a straight LE peak. This was most evident in Figure 4.19, annotated by black ovals close to the leading edge. It is believed that mutual interference between SWCRV from adjacent tubercles is reduced. It can also be noted in Figure 4.20 where a lesser quantity of oil was used for better visualization, that small patches of oil can be observed behind the flat peak at the leading edge due to the effect of SWCRV. However, no oil was observed in the downstream sections of the blade until it stalled at $\frac{x}{c} \approx 0.6$. Video revealed that the flow was mobilized until 0.8c.
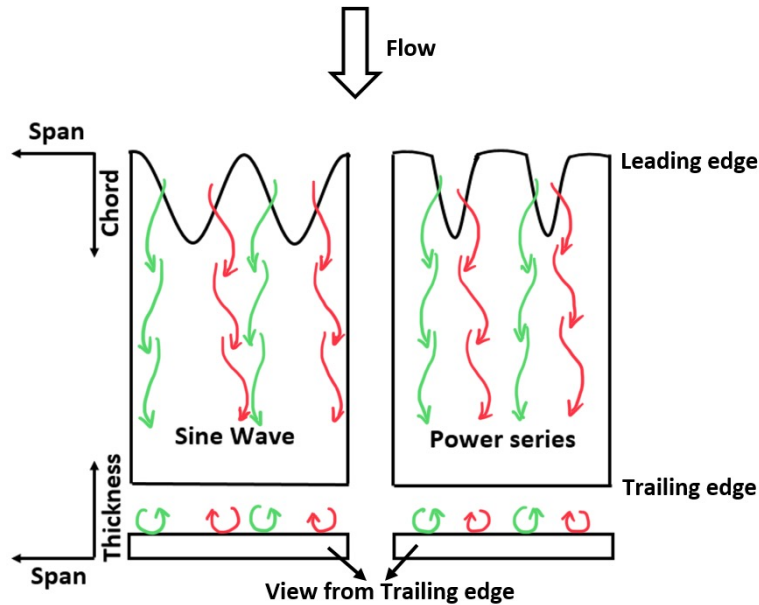

Figure 4.21: Conventional sine wave *vs* power series tubercles

To summarize, flow compartmentalization can be clearly seen, as flow behind the peak is attached while flow behind the valley is separated preventing spanwise spread of local stall. Similar flow phenomenon were also evident on power series profiles, and greater expanses of attached flow were evident particularly behind tu-

Table 4.4: Phase 2 cascade blade tubercle geometries

Blade Profile	A [%c]	λ [%c]
Baseline	0	0
A4L13	4	13
A3L11	3	11
PSA3L9	3	9
PSA3L11	3	11

bercle peaks. A power series tubercle shape was tested for the first time here on compressor blades. Comparable performance between baseline, traditional tubercle shape and power series can be observed at lower AOI. Traditional tubercle geometry performed best at higher AOI of $10°$.

4.2.2 Compressor Cascade Testing Phase - 2

Results from Phase 1 compressor cascade testing indicated that tubercle geometries A3L11 and PSA3L11 performed better than the baseline airfoil. But tubercle shapes with geometric parameters (A and λ) less than the A3L11 were also tested. Oil flow visualization indicated that higher tubercle spacing reduced inter-tubercle interference and improved blade performance. The power series tubercle geometry performed better at lower AOIs and delayed stall with limited improvement at $10°$ AOI. Interestingly, the cascade blades flexed slightly under load at higher AOI.

In Phase 2, the 3-D printing material was changed to the more rigid *Accura Bluestone* material. Calculations based on material properties were performed and compressor blade loading calculations completed using Keerthi *et al.*'s blade coefficient values [16]. New tubercle geometries were selected based on previous results; as summarized in Table 4.4.

129

4.2.2.1 Wake Analysis

Cascade wake analysis was performed in Phase 2 in a similar fashion to Phase 1. Interestingly blades that stalled at AOI of 8° in Phase 1 did not seem to stall until 10°. Wake analysis for AOI of 10° and 12° are compared to the baseline profile performance shown in Figure 4.22 and 4.23.

In Figure 4.22 for 10° AOI, A3L11 and PSA3L11 tubercle geometries had very similar wake characteristics to the baseline, but the wake was observed to be shifted towards suction surface for the other two (namely A4L13 and PSA3L9). These two tubercle geometries continued to outperform the others as they did in Phase 1. A4L13 and PSA3L9 profiles seem to have wider wake than the baseline. In phase 2, the baseline airfoil experienced delayed stall from 8° AOI to 10° AOI. A potential reason for this is the change in material, since it led to significantly reduced blade flexing. Experiments for these AOI were repeated thrice to validate the results.

Due to the change in behaviour of baseline compressor blade at 10° AOI, wake analysis was extended to 12° AOI to ensure blade stall behaviour could be compared. Wake analysis at 12° AOI is shown in Figure 4.23. Here the baseline cascade blade had stalled completely and its wake can be seen occupying the full blade passage. All tubercled profiles performed better at 12° AOI, as evidenced by wake widths shown in Figure 4.22 and 4.23. The PSA3L11 tubercle profile improved on the baseline but was the worst performer among the tubercled blades. This is consistent with Phase 1 results.
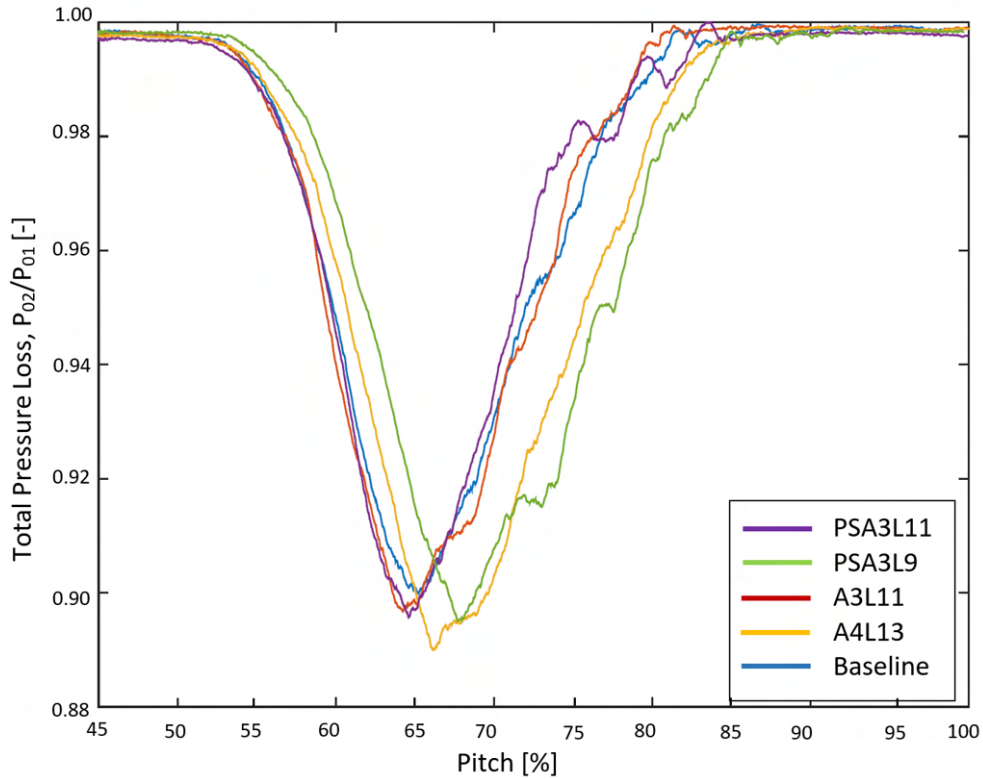
Figure 4.22: Phase 2 blade wake comparison for all 5 blade geometries at AOI = 10°

4.2.2.2 Phase 2 Cascade Losses

The total pressure loss coefficient results are shown in Figure 4.24. At lower AOIs the baseline and tubercled cascades performed very similarly with the baseline performing slightly better at 0° and tubercled blades outperforming the baseline at an AOI of 2°. The baseline blades performed better at 4 and 6° AOI, which can be explained by the loss of total pressure due to the generation of vortices when flow was attached, and of course, there was no need for flow control. Tubercled airfoils performed better at 8° AOI as expected, since stall initiated at this AOI in Phase 1. However, the trend did not continue to 10° AOI where surprisingly, the baseline performed better
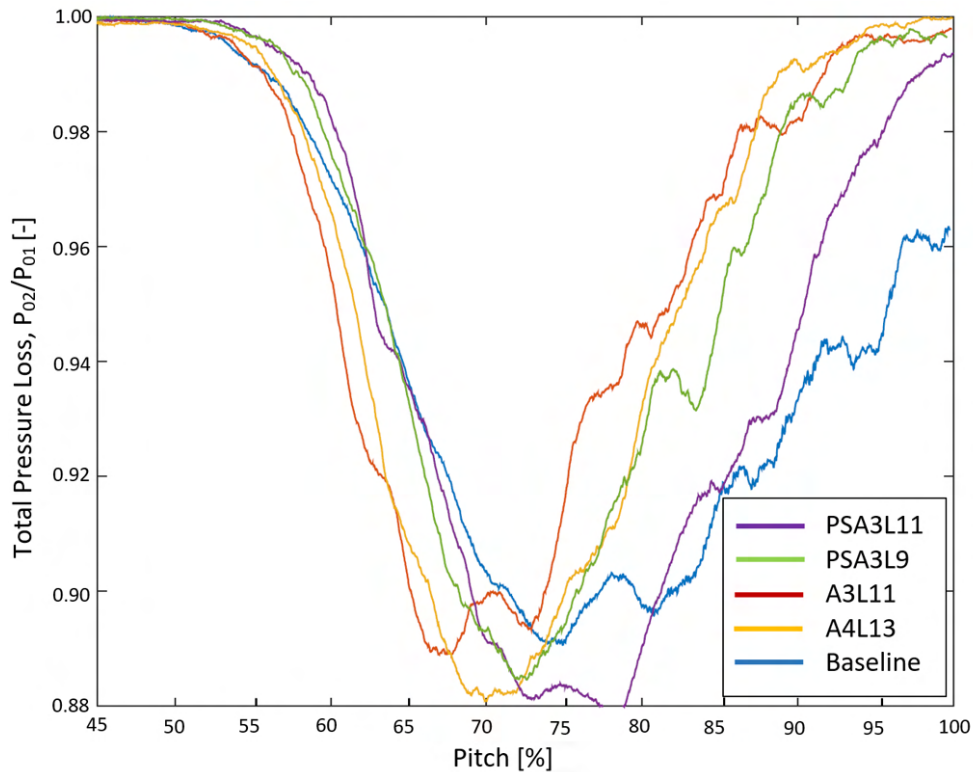
Figure 4.23: Phase 2 blade wake comparison for all 5 blade geometries at AOI = 12°

than all tubercled airfoils. The baseline profile experienced a significant rise in total pressure losses at 12° AOI due to the full span blade stall with wakes almost filling the pitch-wise spacing.

These results present evidence that, when compared to the baseline, the A3L11 profile consistently encountered lower pressure losses at all AOI except at 4 and 6°. A3L11 had best results at two critical AOI: 0°, the design point and 12°, the point of complete compressor blade stall. Per the theory proposed after Phase 1 tests, the newly proposed reduced tubercle wavelength PSA3L9 experienced improved results over PSA3L11 in the post-stall regime and had better or similar performance than
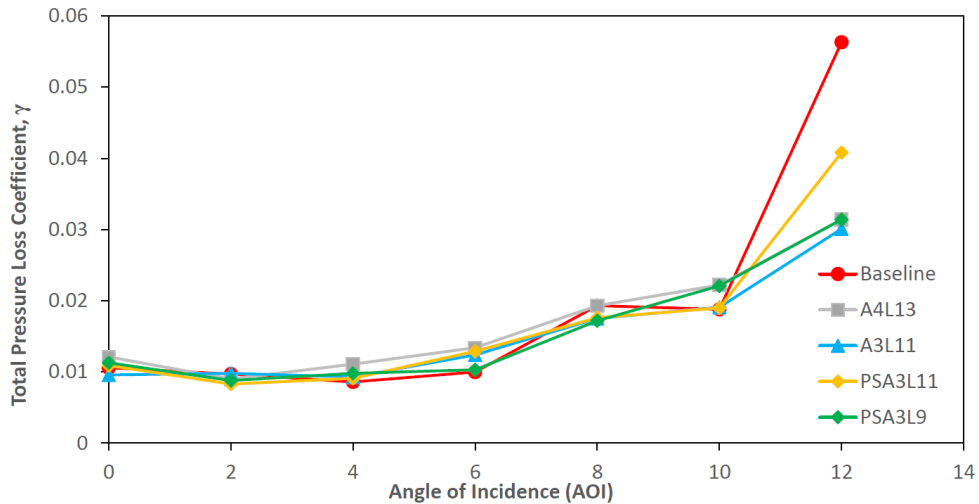
Figure 4.24: Phase 2 total pressure loss coefficients for all 5 blade geometries

the baseline at all AOI except 4°. This (PSA3L9) profile performed very similarly to A3L11 except it experienced slightly higher total pressure losses at 0° AOI which can be attributed to the reduced wavelength geometry generating more SWCRV per unit span. In all, PSA3L11 was the best performing geometry in Phase 1 but had higher total pressure losses at 12° AOI compared to other tubercle geometries. The slightly higher wavelength and amplitude A4L13 tubercle shape improved loss coefficients in the post-stall regime, but this came at the cost of increased losses in the pre-stall regime, specifically at AOIs of 4 and 6°. The PSA3L11 profile showed unsurprising results, with improvements in pre-stall regime at all AOI but performance lagged behind all other tubercle geometries in the post-stall regime. Post-stall regime was of primary concern in this study to improve compressor stall characteristics. The objective of this work was to find a tubercle geometry that can delay compressor stall without affecting compressor performance in pre-stall regime.

4.2.2.3 Pressure Sensitive Paint Testing

Pressure sensitive paint testing was performed at 8 and 12° AOI. The former was selected due to the significant increase in total pressure loss coefficient, indicating stall onset and 12° AOI was selected to understand tubercle flow better after blade stall. PSP results are shown in Figure 4.25 and 4.26, looking at the cascade middle blade suction surface with the pressure values indicated on the right.

As shown in Figure 4.25(c) it can be observed that at 8° AOI, A3L11 has an area of low pressure downstream of the tubercle valley. This tubercled blade clearly demonstrated the presence of SWCRV, generating regions of low pressure towards the leading edges. The streaks, indicating low pressure regions on the tubercled blade suction surfaces, can be easily seen on A3L11 (Figure 4.25(c)) and A4L13 (Figure 4.25(b)). It is not as clear in the PSA3L11 and PSA3L9 results of Figures 4.25(a) and (d) respectively, since these tubercle shapes were not expected to generate SWCRV of sufficient strength to counter stall at an AOI of 8°.

Here, both A3L11 and A4L13 displayed the lowest suction surface pressures out of all compressor blade profiles tested. A3L11 showed more intense low-pressure regions near the leading edge whereas A4L13 showed slightly less intense but somewhat more widely chordwise distributed low-pressure regions, especially on the suction surface. The A4L13 blade displayed less green coloured area toward the trailing edge of the blade, signifying lower suction. For both A3L11 and A4L13, the flow seemed to remain attached longer chordwise. The power series profile, PSA3L9, showed slight flow improvements as compared to the baseline, whereas its longer wavelength counterpart PSA3L11 did not improve attached flow on suction surface as much. In general, flow visualization results agreed with the total pressure loss co-
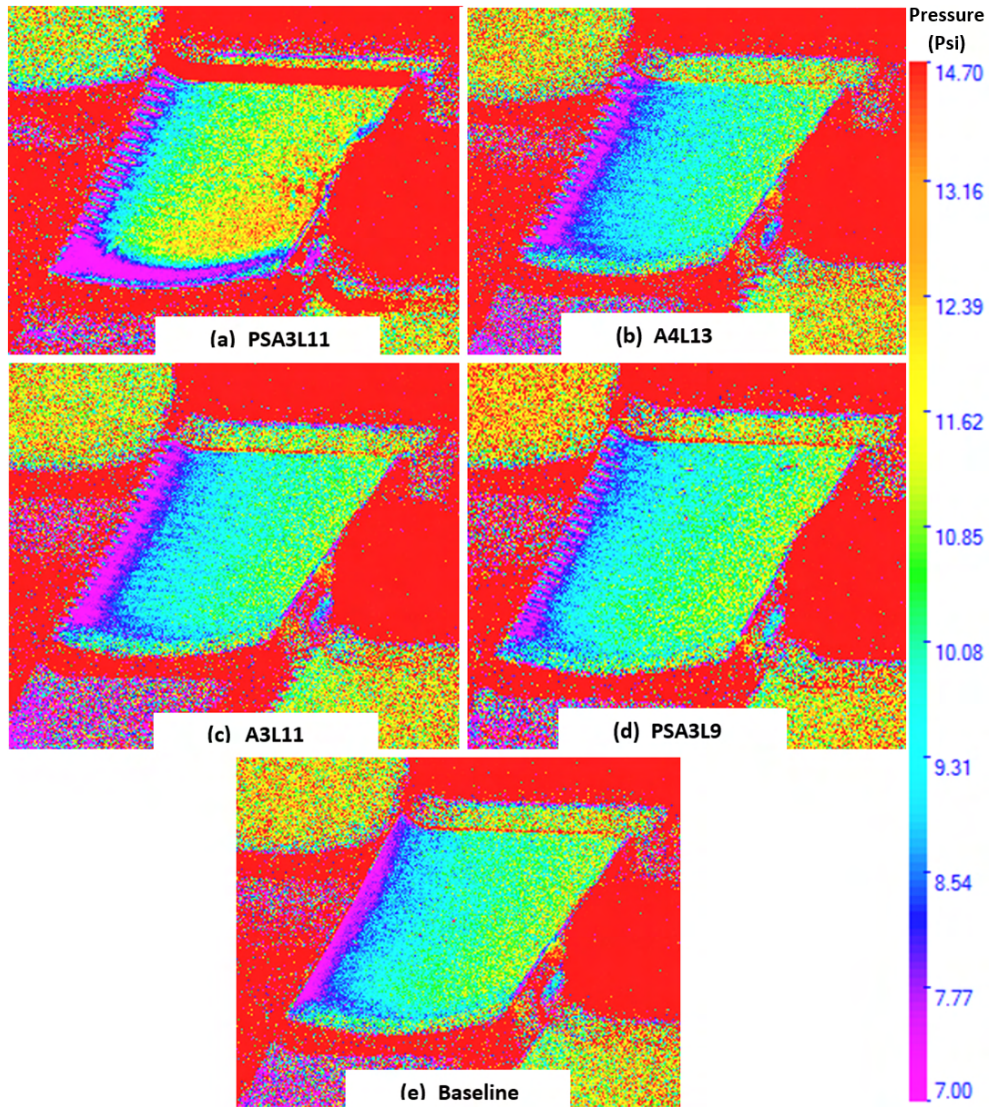
Figure 4.25: Suction surface pressure sensitive paint results at 8° AOI

efficient, except for PSA3L11. A4L13 had a higher loss coefficient than the baseline, as shown in Figure 4.24, but the PSP revealed significant improvements: specifically higher suction, and the flow seemed to be attached for longer chordwise than it did on the baseline blade (Figure 4.25(c) vs (e)). The stronger SWCRV revealed by the PSP are likely the cause of higher total pressure loss coefficients for A4L13.

The AOI = 12° post-stall PSP results presented in Figure 4.26 revealed irregular patterns of flow over the suction surfaces of all profiles tested. The baseline blade flow separated near the centre of the blade, evident from the lack of low presure region (pink) in Figure 4.26(e). The flow seemed to be influenced by the endwalls, a pattern also seen for the tubercled blades tested. Comparing the span-wise centre region of the blades, A3L11 (Figure 4.26(c)) had higher suction than the baseline (Figure 4.26(e)), indicating attached flow. A4L13 (Figure 4.26(b)) displayed uniform flow along the span of the blade, potentially due to the stronger SWCRV compartmentalizing the apparent endwall effect. Tubercle geometries were able to isolate the flow from endwall effects much better than the baseline, since a more uniform low pressure region (pink) was present. For the baseline, a much stronger low pressure region can be seen on both sides with significantly different pressure in spanwise central section. A4L13 profile showed slightly more blue, presumed to result from data manipulation while aligning two images of the PSP. Data manipulation was only performed for A4L13 due to a mis-alignment of camera during those runs. PSA3L11 and PSA3L9 demonstrated slight improvements in delaying flow separation over the baseline. PSP results indicated that A3L11 and A4L13 performed better among tested tubercle profiles, especially at higher AOI.

PSP and total pressure losses indicate that A3L11 and A4L13 are the two tubercle shapes most effective at delaying stall at post-stall AOI, with A3L11 slightly better
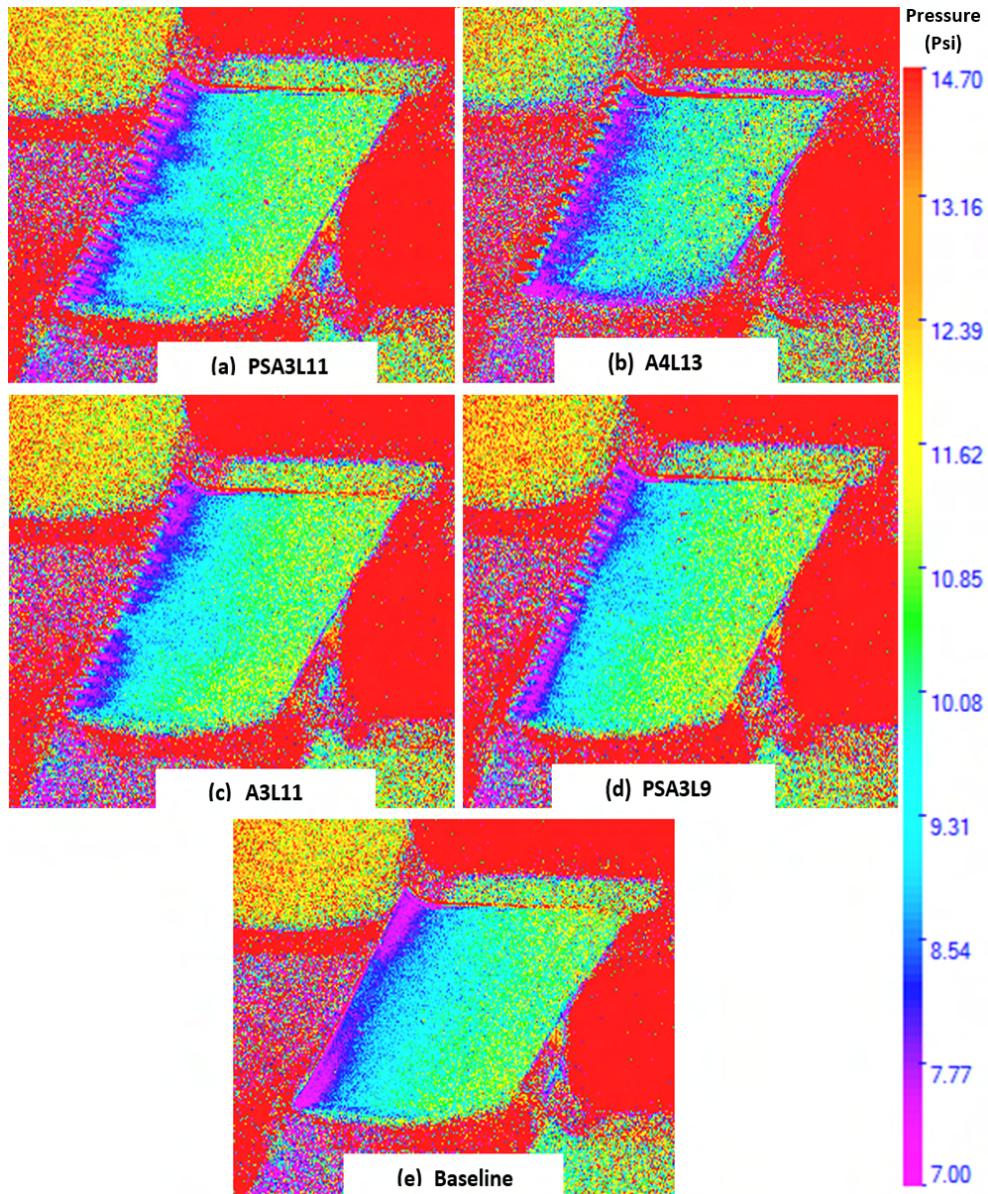
136

Figure 4.26: Suction surface pressure sensitive paint results at 12° AOI

of the two. The A3L11 profile's PSP and total pressure loss coefficients results were consistently better than A4L13 in pre-stall regime. PSA3L11 also performed best in the pre-stall regime but its performance in the post-stall AOI lagged behind the conventional sinusoidal tubercled profiles. A3L11 showed comparable performance in pre-stall regime to PSA3L11 and in post-stall to A4L13. The consistent performance of A3L11 in pre-and post-stall regime led to its selection for implementation on the A-250 compressor blades for the 3-D compressor rig testing. Singnificant post stall performance improvement was one of the primary factor in the selection of A3L11 for final phase testing.

4.3   Compressor Rig Testing

In Phase 1 and 2 testing, the A3L11 tubercle profile consistently outperformed the others in the pre-stall regime while significantly improving the post-stall flow regime. Except at 6 degrees, A3L11 showed improved total pressure loss coefficient in Phase 1. Similarly, it had lower total pressure loss coefficients results in Phase 2 except at 4 and $6°$ AOI. The PSA3L11 and PSA3L9 profiles also had better results than the baseline for total pressure loss coefficients, but PSP results did not present any evidence of these improvements. The PSP results indicated lower suction, indicating reduced tubercle effect at higher AOI.

Compressor cascade work was performed on a 2-D linear cascade to optimize tubercle geometry for the mid-span section of the first stage rotor blade, without any rotational component. Neither radial pressure gradients nor pulsating flow were incorporated in the testing and results from 2-D compressor cascade were used to select an optimized tubercle geometry for 3-D A-250 axial compressor. A selected

full-span tubercle geometry was applied to all stages of the test compressor.

4.3.1   Compressor Map Analysis

Full scale operational compressor testing was performed on four different axial compressor configurations (see Table 3.6), including one on the unmodified component to establish baseline performance. Compressor testing was only performed in steady state compressor operating regimes. The baseline A-250 axial compressor generated maximum pressure ratio of 1.89 when operating at 95% design speed. Compressor testing was performed first at lower speeds, then progressively faster until the design speed was reached to maintain the pressure and temperature within safety margins. The measured mass flow rate and exit pressure were used to generate compressor maps. The baseline compressor map is shown in Figure 4.27 where it is evident that a maximum compressor corrected mass flow rate of 1.23 kg/sec was achieved with the throttle valve fully open.

Tubercle testing began with the rotor and stator compressor blades modified using the optimized tubercle shape from linear cascade testing. Configuration 2 (A3L11) compressor with both rotor and stator blades modified was tested first, generating a similar pressure ratio to the baseline at 60% RPM, but at a lower corrected mass flow rate. With increased RPM, Configuration 2 matched the baseline performance at 70% RPM, and improved on performance to 80% rpm where higher corrected mass flow rate and increased maximum pressure ratio are clear in Figure 4.27. Configuration 2 reached a pressure ratio of 1.57 as compared to 1.54 for the baseline. However, this trend did not continue to 90% rpm where a significantly reduced pressure ratio was achieved compared to the baseline. Similar degraded performance was observed for 95% RPM where Configuration 2 followed the baseline constant RPM curve closely,

139
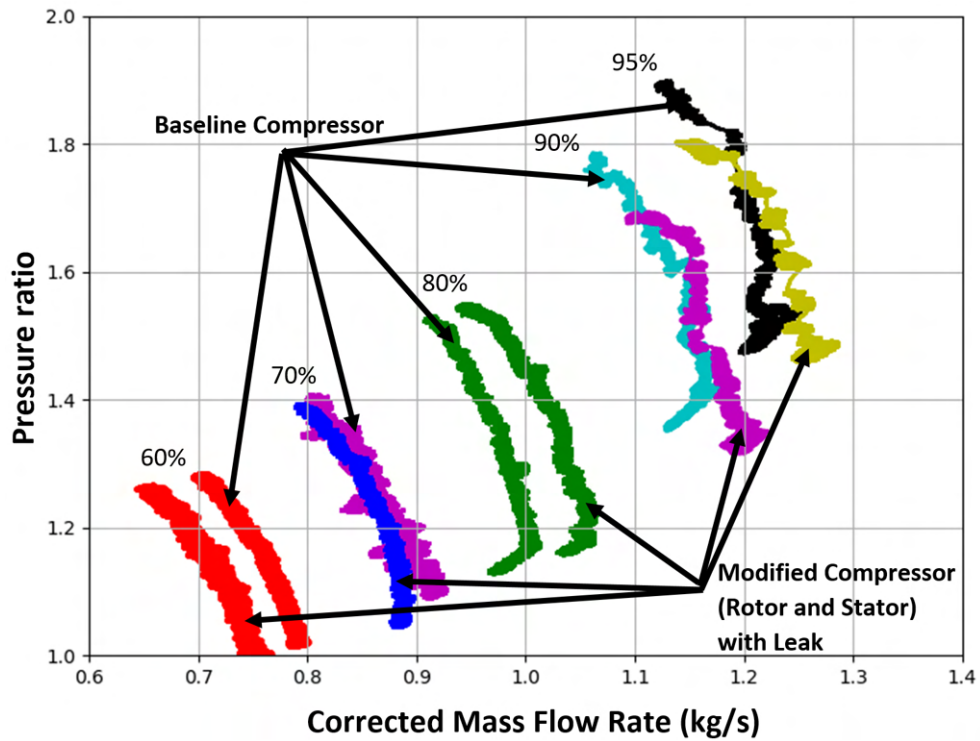
Figure 4.27: Compressor map of modified A-250 (Rotor and Stator (A3L11)) *vs* baseline with bleed valve slightly open (Configuration 1 and 2)

but was not able to reach the same peak PR. After the testing of Configuration 2 was completed, it was determined that the bleed valve at the fifth stage had been stuck partially open. It was interesting to see that Configuration 2 performance was on par with the baseline until 80% RPM where a bleed valve was not expected to help a compressor to achieve higher pressure ratio. The Configuration 2 compressor reached a peak pressure ratio of 1.81 at 95% RPM compared to 1.89 for the baseline.
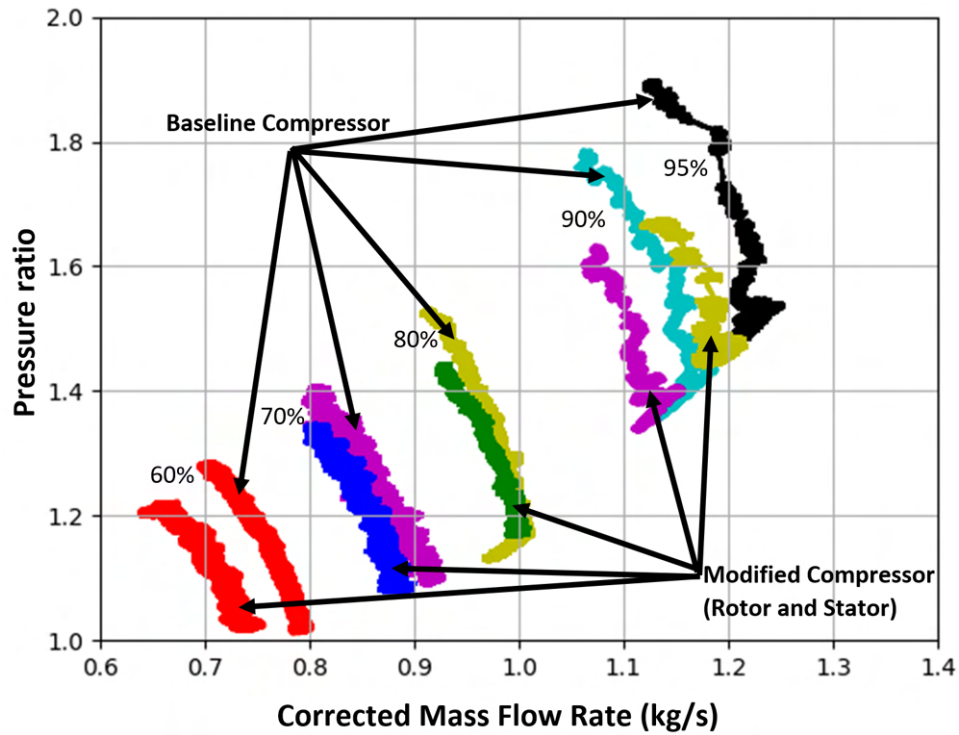
Figure 4.28: Compressor map of modified A-250 (Rotor and Stator) *vs* baseline compressor map with bleed valve closed (Configuration 1 and 3)

Modified compressor Configuration 3 is the fully tubercled compressor, but tested with the bleed valve closed. Its performance comparison with the baseline is shown in Figure 4.28. The tubercled compressor was expected to improve performance even beyond the 80% demonstrated by Configuration 2. But closing the bleed valve did not improve performance over the baseline nor Configuration 2 results. Indeed, the maximum pressure ratio reached was only 1.68.

This perplexing result was explained after more careful consideration of tubercle design: The tubercle shape was optimized based on the first stage rotor blade. The flow condition for the rotor blades involve a blade-relative velocity component due
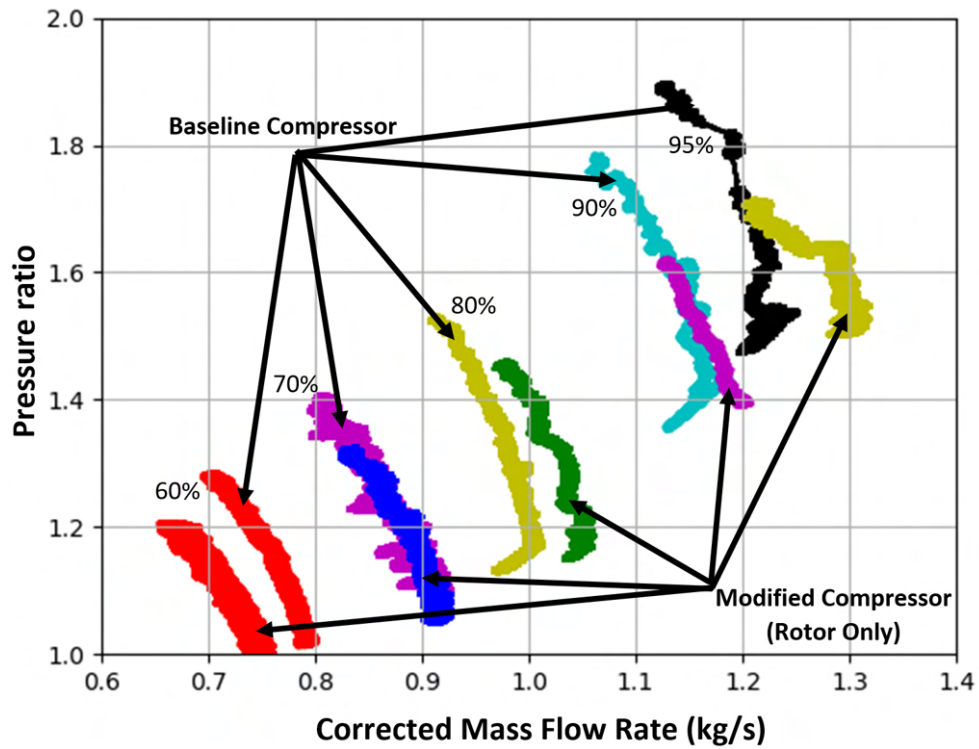
Figure 4.29: Modified A-250 (Rotor only) *vs* baseline compressor map (Configuration 1 and 4)

Table 4.5: Compressor pressure ratio results for configurations tested

RPM (% design speed)	Configurations			
	1 (Baseline)	2 (Valve Open)	3	4
60	1.28	1.27	1.22	1.21
70	1.41	1.4	1.36	1.34
80	1.54	1.57	1.45	1.46
90	1.78	1.7	1.63	1.62
95	1.9	1.8	1.68	1.72

to rotation. Relative flow conditions were considered during the tubercle shape optimization. It was also anticipated that the rotor blades would encounter stall before the stator blades due to the higher relative flow speed. It was hypothesized that the modified stator blades are contributing to the increased vorticity when flow control is not required. Increased vorticity is estimated to result in increased compressor losses. To test this hypothesis, Configuration 4 was developed for a compressor with tubercles on rotor blades only. The results are shown in Figure 4.29 where improvements were apparant in corrected mass flow rate but not in pressure ratio. Configuration 4 performed very similarly to the Configuration 3, achieving a maximum pressure rato of 1.7 significantly lower than the baseline performance. The pressure ratio maxima achieved at a range of design speeds are summarized in Table 4.5.

4.3.2 Stall Inception Analysis

The A-250 compressor stages were instrumented with *Kulite* fast response pressure transducers in the overtip regions (see Table 3.5 for locations). When the modified Configurations (2,3,4) compressor map results did not manifest the anticipated improvements: presure ratio increase or stall delay, *Kulite* data were explored to analyze flow characteristics inside the compressor. The *Kulites* were originally fitted at different axial locations to track the progress of rotating stall cells in Bennett *et al.*'s study [2]. To help explain tubercle results and baseline rotating stall characteristics, the A-250 baseline compressor stall at 60% and 70% rpm indicated the presence of a rotating stall cell, shown in Figures 4.30 and 4.31. Stall cell's rotational speed was calculated to be approximately 56% of the compressor rotational speed at both 60 and 70% speed tests. This is in agreement with the findings of Bennett *et al.* [2]. It can be clearly observed that the rotating stall develops in compressor's first stage

(red plot) and the rotating stall cell, shown with red circles. In Figure 4.30 and 4.31, stall cell can be seen progressing to downstream stages of compressor. In Figure 4.31, the stall cell increased intensity with time and progressively bigger spikes can be observed that developed into full compressor stall at 70% RPM. The results from this study, shown in Figure 4.30 and 4.31, are in agreement with those of Bennett *et al.* [2].
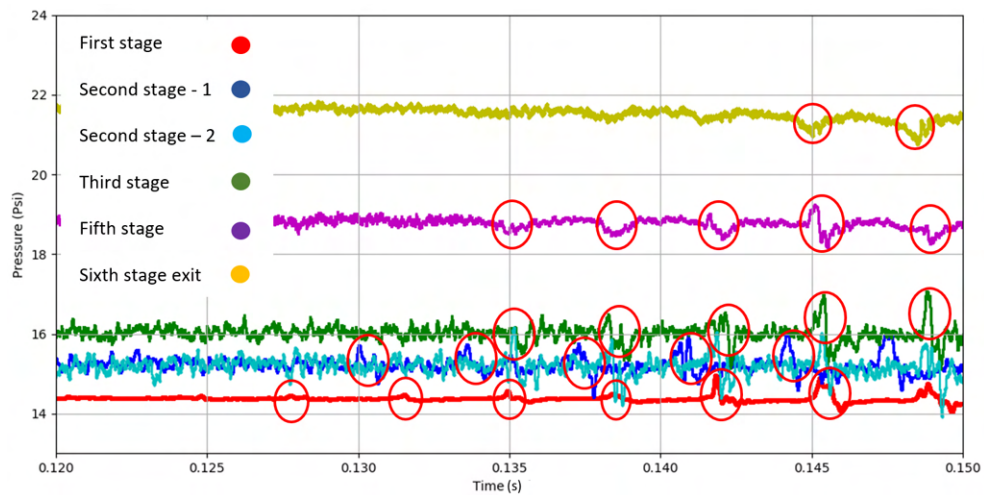
Figure 4.30: Casing static pressure traces for the baseline configuration (1) at 60% design speed

Kulite measurements were also taken for modified test configurations, except Configuration 4 since that test's unmodified stators necessitated an uninstrumented casing be installed. These tests clearly showed that the modified A-250 compressor stall characteristics were fundamentally different. *Kulite* results for Configuration 3 are shown in Figures 4.32, to 4.34. Here, no stall cell formed at the initial stage at any speed. These results contradict the B-parameter findings (see Section 2.2.3) of Greitzer *et al.* [28]. No changes were made to the plenum nor any other components and

Figure 4.31: Casing static pressure traces for the baseline configuration (1) at 70% design speed

Figure 4.32: Casing static pressure traces for the modified rotor and stator compressor (3) at 60% design speed

145

Figure 4.33: Casing static pressure traces for the modified rotor and stator compressor (3) at 70% design speed

Figure 4.34: Kulite pressure traces for the modified rotor and stator compressor (3) at 90% speed

the value for the *B*-parameter was unchanged. In the tubercled compressor, periodic pre-stall disturbances were not obse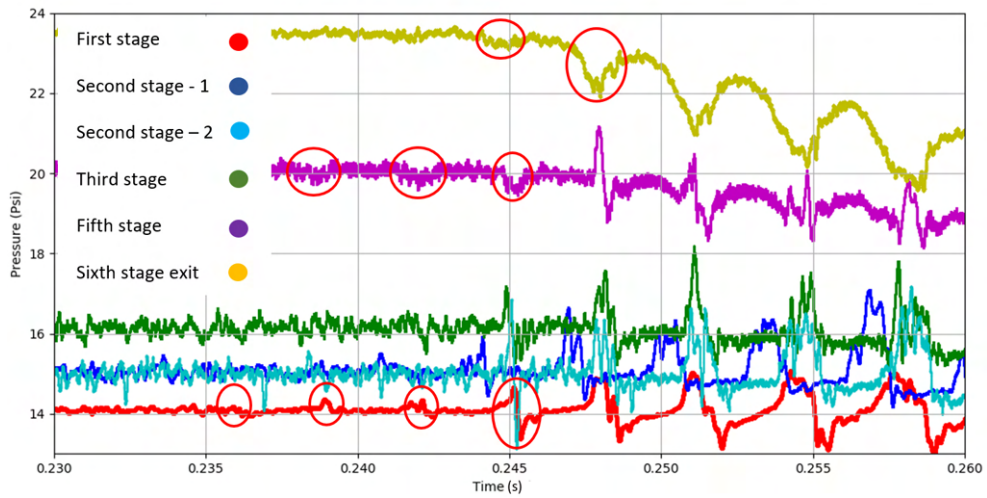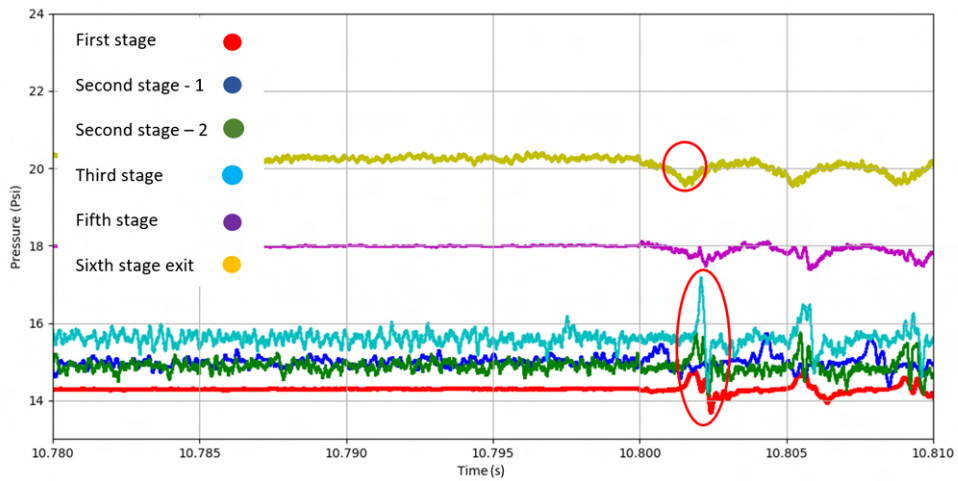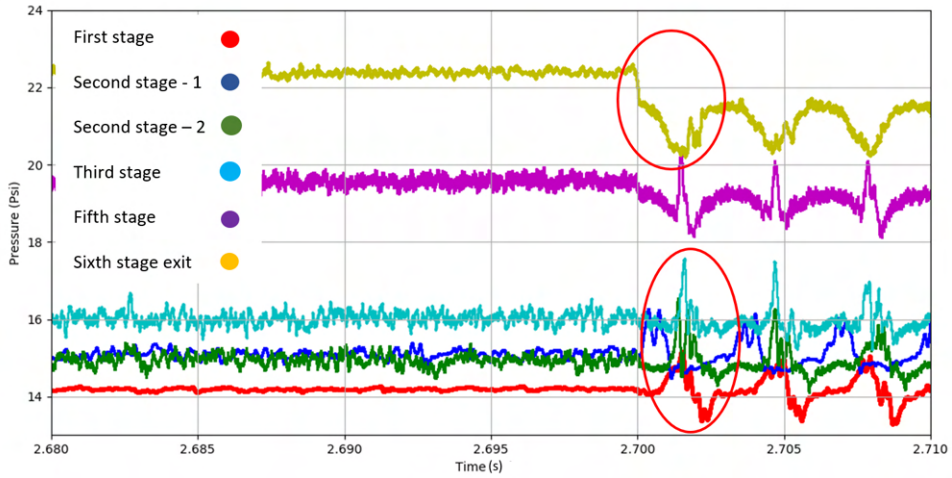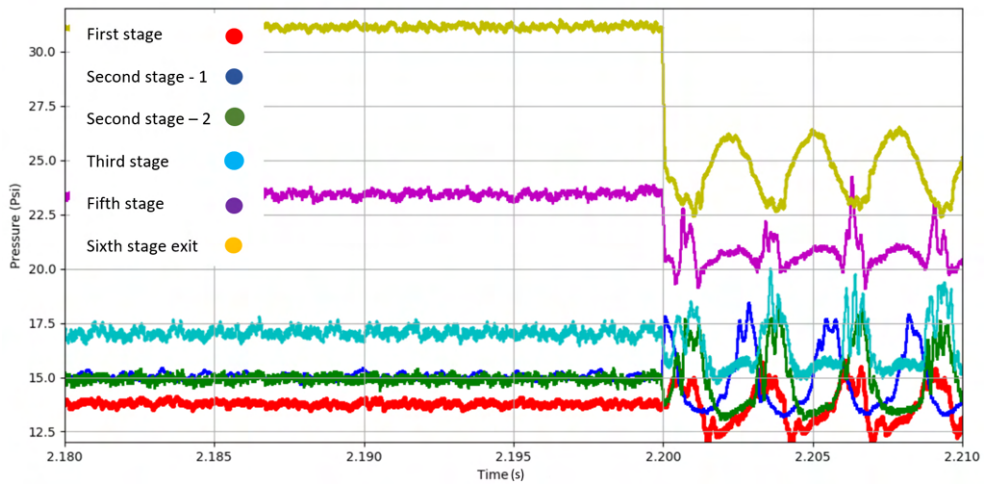rved in any of the six stages of the compressor (Figure 4.32 for example at 60% speed). Moreover, it can be observed in Figure 4.33 and 4.34 that compressor stalled first at Stage 6, the exit of the axial stage. This is evidence of a sudden flow breakdown that progresses from the later stages to the upstream compressor stages. In Figure 4.32, it can be observed that the compressor encountered sudden flow collapse at a run time of 10.8025 *s*. In Figure 4.33 similar and more dramatic results are observed for 70% speed at 2.7 s. Here, the stall initiated with sudden and clear collapse of stable flow at the sixth stage (yellow trace). At 90% speed, as seen in Figure 4.34, the event occured at 2.2s.

From the *Kulite* analysis, it is observed that tubercles affected the flow, successfully delaying the compressor stall cell formation in the early stages. This is attributed to the tubercle design, since the tubercle shape was optimized for the first stage rotor blade and its flow conditions. The same shape was used for all the compressor blades, even with the understanding that different flow conditions existed for other stages. It is hypothesized that the tubercles degraded the performance in later stages of the compressor, reducing overall performance for more reasons than that are explained presently. Documented tubercle studies clearly demonstrate that the tubercles, when not optimized, result in lower maximum lift, lower lift curve slope and an earlier, but more gradual stall. Here the positive influence that the tubercles had in early stages demonstrated the great potential for tubercle applications in high speed axial compressors.

Tubercle performance enhancement is also supported by improvements in stable compressor performance at 80% speed observed in Configuration 2 (see Figure 4.27). It is believed that the bleed valve at the fifth stage of the compressor helped isolate

147

the stall formed in later stages from upstream stages. The bleed valve likely hindered upstream stall propagation delaying a full compressor stall. But the partially open bleed valve was not able to continue hindering the stall from later stages when the compressor was run at 90 or 95% speed.

For future testing, it will be interesting to assess the effect of tubercles on stall cell formation when they are incorporated solely on the first stage rotor blades. This is because the A250 stall characteristic involves stall cells forming at the first stage. Tubercles show promise to prevent formation of these stall cells, improving overall compressor performance by expanding operability.

SWCRV were not expected to significantly influence the compressor flow due to their local influence. It is believed that, with careful manufacturing of tubercles on the compressor blades, they can diminish tip leakage flow by generating a SWCRV that restricts tip leakage flow migration to the suction side. Using a single tubercle shape from hub to the tip was not ideal since conditions change radially and axially, affecting overall tubercle effectiveness while not significantly degrading compressor mass flow.

4.3.3 Tubercle Shape Fabrication Deficiencies

In many tubercle studies, 3-D printed plastic was used for manufacturing test articles. The actual tubercle size for these applications always was sufficient to fair out sharp edges to achieve smooth transitions. SOM studies revealed that tubercles tended not to perform well when shaped like delta wings. In the 2-D compressor cascade testing, compressor blades were 3-D printed ensuring smooth transitions of tubercles to the airfoil surfaces. In the tubercle optimization for the cascade work, the compressor blade size was scaled 1.5:1, making the geometry suitable for 3-D printing. How-

ever, for the 3-D compressor rig testing, actual A-250 compressor blades were used and manufacturing for the desired tubercle shape on the actual compressor blades was extremely complicated. Technical challenges included hardened blade material, small blade size and extremely small tubercle size with amplitude on the scale of one to two millimeters.
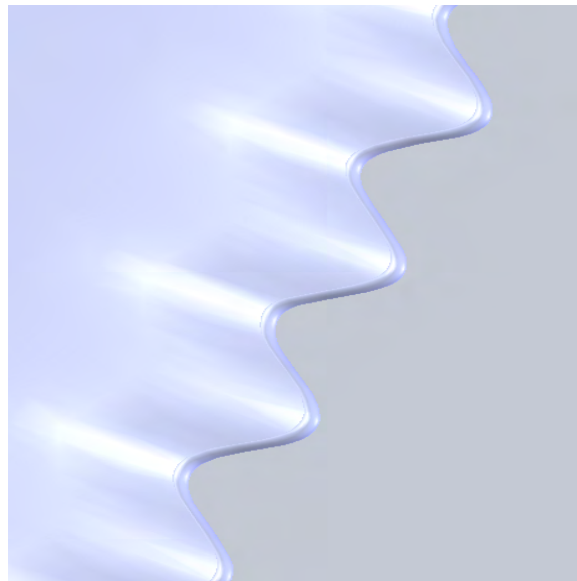
Figure 4.35: CAD Isometric view of compressor blade with tubercle modified leading edge

The compressor blade tubercle shape used in the 2-D compressor cascade can be seen in the CAD rendering in Figure 4.35, where a smooth transition from the tubercle leading edge to the blade airfoil is clear. To manufacture the same tubercle shape on the leading edges of the A-250 compressor blades required sinker EDM machining. EDM machining was the only method determined to be able to achieve sufficient accuracy. Leading edge was eroded in the form of desired tubercle geometry using electric sparks. But this resulted in sharp edges at the transition points from tubercle

149
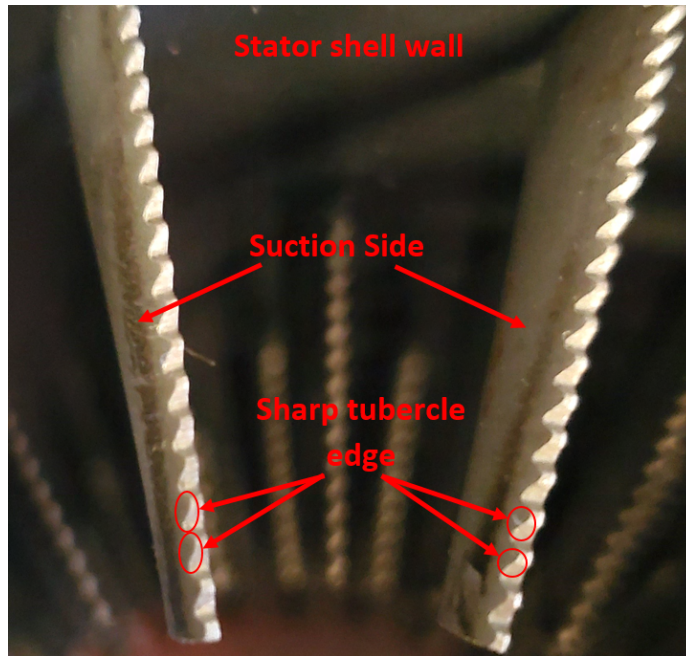
Figure 4.36: Modified A-250 stator blade with sharp tubercle edges

to blade airfoil, especially in the valleys of the tubercles, due to the increased airfoil thickness easily seen, and highlighted in Figure 4.36 with red circles. It is hypothesized that, when the load on the compressor was increased, these sharp edges forced abrupt flow separation resulting in stronger SWCRV. Results from the SOM and 2-D cascade analysis gave clear indications that tubercles are effective when optimal amount of SWCRV are generated. The optimal strength of SWCRV should be able to delay blade stall. Compressor blades in the later stages are observed to be shorter chord-wise, but their maximum thickness remained the same as initial stages. It is believed that sharp edges at tubercle transition points resulted in generation of extra strong SWCRV, defying the expected tubercle effect of delaying and softening the effects of stall. These sharp edges caused abrupt flow separation leaving the com-

pressor flow significantly degraded as compared to those validated in 2-D cascade work.

This was the first ever attempt of modifying hardened A-250 compressor blades with tubercle geometry. While largely successful, it would be improved through obtaining greater precision in final tubercle shape. This will entail dedicated research in manufacturing and surface finishing procedures. Tubercle manufacturing techniques can equally benefit from compressor modification trials in a research machine shop setting where the primary focus of the machinist is to achieve desired accuracy and surface finish. This is good practice demonstrated by the Lietmeyer's team [84] that manufactured riblets on compressor blade surfaces.

5 Conclusions and Recommendations

5.1 General

This work was initiated to assess the performance of leading edge tubercles on gas turbine axial compressor blades. For this goal, tubercle optimization was performed using Self Organizing Maps (SOM), a neural network technique that highlighted correlations between tubercle geometric and performance parameters. Tubercle geometries were selected from the SOM analysis and tested in a compressor linear cascade. Finally, the best performing tubercle geometry was selected for the testing in a 3-D rotating compressor rig at operational conditions.

5.2 Conclusions

In order to train the SOM for optimizing tubercles, geometric, flow and performance paameters were collected from literature. Two geometric parameters: Reynolds number based on hydraulic diameter (Re_{Dh}) and tubercle aspect ratio ($\cancel{A}R$) and one performance parameter: post-stall operability area, were introduced to characterize better the 3-D flow phenomenon introduced by tubercles. SOM results indicated that

lower Re_{Dh} corresponded to higher maximum coefficient of lift ($C_{l,max}$) and higher stall angles (α_s). It was found in previous studies that lower tubercle $\math!R$ improved airfoil performance, which was interesting because lower $\math!R$ is characteristics of a tubercle shape dissimilar to the delta wing. However, some researchers believe that each tubercle acts like a delta wing, causing abrupt flow separation and consequently, streamwise counter rotating vortices (SWCRV) in the process. The findings in this work were contrary to this belief and suggested tubercle geometries should be adept at generating SWCRV with optimal vortex strength, avoiding destructive mutual interference. SOM results also indicated that optimized $C_{l,max}$ and α_s performance would be achieved with tubercle amplitude (A) around 3% of chord (c). The tubercle wavelength (λ) did not display any strong correlation; however, lower tubercle λ showed direct correlation with improved post-stall operability area. The overall results indicated that lower A, λ and Re_{Dh} resulted in improved airfoil profile performance with increased $C_{l,max}$, higher α_s and larger post-stall operability area. SOM also indicated that the tubercles do not perform well when shaped like tiny delta wings but rather need smooth transitions in order to generate SWCRV with optimal strength to delay boundary layer separation. SOM was limited by tubercle experimental data available for training. Tubercle A below 3%c and λ below 11%c were not explored. These gaps were explored in low speed wind tunnel testing. Larger data set would have further improved the effectiveness of SOM.

Three tubercle geometries were then selected for testing in a compressor linear cascade based on the *Rolls-Royce* A-250 axial compressor first stage rotor blade mean geometry and flow conditions. Baseline and modified compressor blade performance was compared using total pressure measurements, flow visualization and pressure sensitive paint (PSP). It was found that all tubercled geometries delayed

153

stall, as compared to their baseline, while showing comparable and slightly increased losses at the design angle of incidence (AOI). In flow visualization tests, mobilized oil behind the tubercle peaks indicated the presence of SWCRV. Flow seemed to be separated behind tubercle valleys and SWCRV from adjacent tubercle peaks could be observed expanding spanwise, downstream of the valley, in some cases destructively interacting with each another. For total pressure measurements, the $A = 3\%c$ and $\lambda = 11\%c$ (A3L11) performed best in the post-stall regime with comparable performance at other pre-stall AOI. Power series profiles ($A = 3\%c$ and $\lambda = 11\%c$ (PSA3L11) were able to delay stall but total pressure losses were observed to be higher than sinusoidal tubercle geometries. From PSP analysis, it was found that A3L11 and $A = 4\%$ and $\lambda = 13\%$ (A4L13) profiles displayed lowest pressure coefficients (suction) at post-stall AOI on the suction surface indicating attached flow and reduced pressure loss. In the cascade tests (Phase 1), the power series tubercle shape had the best performance at all pre-stall AOI, followed by A3L11. But A3L11 had the most consistent performance, followed by PSA3L11. At the conclusion of both phases of the linear cascade tests, the A3L11 tubercle shape was selected for testing in a 3-D compressor rig at operational conditions. The linear cascade work was limited by a small test section cross-sectional area and consequently small blade geometry. The compressor profiles tested were very thin and their limited strength and dimension precision were major factors in the selection of manufacturing material.

A-250 axial compressor blades were modified to incorporate tubercles using Sinker Electrical Discharge Machining (*EDM*). Compressor testing was performed with four different configurations: the baseline unmodified compressor (Configuration 1); with modified rotor and stator blades, with the bleed valve partially open and fully closed (Configurations 2 and 3 respectively); finally, only rotor blades mod-

ified (Configuration 4) with bleed valve closed. Compared to the baseline, testing with modified rotor and stator blades showed promising results with improvements in pressure ratio up to 80% speed. But the improvement trends were not sustained at higher, 90 and 95% speeds; nor did Configurations 3 and 4 show any improvements in pressure ratio over the baseline. High-speed, casing-mounted pressure transducers revealed stall cells in the first stage of Configuration 1 (the baseline A-250 compressor) before full stall developed. This was expected since Bennett *et al.* [2] had already characterized the A-250 stall and shown it consistent with the Greitzer compressor model predictions. But for tubercled compressor, rotating stall cells were not observed at any speed. Tubercles eliminated the formation of stall cells in any stage of the compressor prior to full compressor stall, initiated at the final stage and thereby, deviating from Greitzer's compressor model. This notable event is attributed to the fact that tubercle optimization was performed for the mid-span flow conditions of the first stage rotor. However, the flow conditions vary significantly in later stages. Some improvements observed for Configuration 2 at 80% speed can be attributed to the isolation provided by the open bleed valve preventing stall from propagating upstream.

The early successful improvement (up to 80% speed) by a tubercled compressor is attributed to the tubercle manufacturing technique for the A-250 compressor. Sinker EDM produced abrupt transitions on leading edges, particularly in the tubercle valleys, instigating flow separation and increased losses under load. Tubercle design and manufacturing challenges resulted in some unexpected outcomes. Tubercles showed potential, both increasing pressure ratio despite having a partially open bleed valve during operation and successfully eliminating stall cell formation. With improvements in manufacturing technique, tubercles can potentially improve com-

155

pressor performance, as undesired abrupt edges from machining almost certainly limited their performance.

5.3 Recommendations

Compressor cascade work should be extended in a larger transonic wind tunnel allowing bigger cross-sectional area of the compressor cascade and enabling the testing of physically larger compressor blades. Larger compressor blade can be manufactured with static ports, which would be advantageous in tubercle performance assessment. Larger blades can also be manufactured using stronger materials, eliminating any blade deflection under load. Compressor cascade testing should also be performed for different compressor stages at stage-specific flow conditions.

3-D testing of an axial compressor is recommended with just the first stage rotor blade modified. This should reveal if the tubercled first stage actually mitigates compressor stall cell formation at first stage without any adverse affects on later compressor stages, which would enhance the understanding of tubercle performance.

The tubercle manufacturing technique should be improved for future applications. Feasibility of finishing procedures must be researched to ensure smooth edges, and precise replication of shapes tested in the linear cascade. Ideally, a new compressor rotor should be manufactured to avoid surface discontinuities from machining. It is often difficult to achieve these minute detailed finishes in a commercial setting, so their manufacturing should take place in a lab environment where the primary focus of the machinist will be to achieve a precise shape.

During the operation of the compressor rig, the V10 engine was difficult to control due to the excessive power requirement to run the A-250 axial compressor and

insufficient feedback control. It is recommended to implement a feedback loop throttle control system in any future axial compressor rig testing.

Bibliography

[1] L. H. Peristy, Asghar A. Perez, R. E., and W. Allan. Reynolds Number Effect of Leading Edge Tubercles on Airfoil Aerodynamics. In *34th AIAA Applied Aerodynamics Conference*, number AIAA 2016-3260, San Diego, CA, June 2016.

[2] L. G. N. Bennett and W. D. E. Allan. Examination of Rotating Stall Inception in a Small High Speed Axial Compressor. Volume 7:155–165, 06 2009.

[3] B. Coxworth. Speedo nemesis fins inspired by the humpback whale, https://newatlas.com/speedo-nemesis-swim-fins-humpback-whale, 2014.

[4] F. White. *Fluid Mechanics, 7th Edition, McGraw- Hill, New York, 2011*.

[5] I.J. Day. Stall Inception in Axial Flow Compressor. In *Proceedings of the International Gas Turbine and Aeroengine Congress and Exhibition*, number 91-GT-086, Orlando, Florida, June 1991.

[6] A. Epstein, J. Ffowcs Williams, and E. Greitzer. Active suppression of aerodynamic instabilities in turbomachines. *Journal of Propulsion Power*, 5(2):204–211, 1994.

[7] Johari H., C. Henoch, D. Custodio, and A. Levshin. Effects of Leading-Edge Protuberances on Airfoil Performance. *AIAA Journal*, 45(11):2634–2642, Nov 2007.

[8] J. Vesanto, J. Himberg, Alhoniemi E., and J. Parhankangs. Som toolbox for matlab 5. In *SOM Toolbox Team, Helsinki University of Technology*, number A57, April 2000.

[9] ISSI - Innovative Scientific Solutions, Inc., 7610 McEwen Road, Dayton, OH. *ISSI ProAcquire PSP-CCD-C/M Cameras - Operations Manual and Data Acquisition Package (Version 3.3)*, 2018. Available at `www.psp-tsp.com`.

[10] J. Ilott, W. Allan, A. Asghar, and R. Woodason. Characterization of the Discharge Flow of a Dual Volute Axi-Centrifugal Gas Turbine Compressor. In *49th AIAA/ASME/SAE/ASEE Joint Propulsion Conference*, number AIAA 2013-3633, July 14 - 17, 2013.

[11] F.E. Fish and J.M. Battle. Hydrodynamic Design of the Humpback Whale Flipper. *Journal of Morphology*, 225(1):51–60, November 1995.

[12] A. Asghar, R. Perez, P. Jansen, and W. Allan. Application of leading-edge tubercles to enhance propeller performance. *AIAA Journal*, 58:10, 2020.

[13] A. Corsini, G. Delibra, and A. Sheard. The application of sinusoidal blade-leading edges in a fan-design methodology to improve stall resistance. *Journal of Power and Engineering*, 228(3):255–271, 2014.

[14] D. Bouchard, A. Asghar, Hardes J., R. Edwards, W. Allan, and M. LaViolette. Influence of a Novel Three-dimensional Leading Edge Geometry on the Aerodynamic Performance of Transonic Cascade Vanes. In *Transactions of the ASME/IGTI TurboExpo*, number GT2012-69926, Copenhagen, Denmark, June 2012.

[15] P.W. Weber, L.E. Howle, and M.M. Murray. Lift, Drag, and Cavitation Onset On Rudders With Leading-edge Tubercles. *Marine Technology and SNAME News*, 47(01):27–36, 01 2010.

[16] M.C. Keerthi, M.S. Rajeshwaran, A. Kushari, and A. De. Effect of Leading-Edge Tubercles on Compressor Cascade Performance. *AIAA Journal*, 54(3):912–923, March 2016.

[17] H. Emmons, C. Pearson, and H. Grant. Compressor surge and stall propagation. *Trans., ASME*, 1955.

[18] H. Takata and S. Nagano. Non-linear analysis of rotating stall. *Journal of Engineering Gas Turbine Power, ASME*, 94(4):279–293, 1972.

[19] I. J. Day. Stall, surge, and 75 years of research. *ASME J. Turbomach*, 138(1):011001, 2016.

[20] I. Day, E. Greitzer, and N. Cumpsty. Prediction of compressor performance in rotating stall. *ASME Journal of Eng. Gas Turbine Power*, 100(1):1–12, 1978.

[21] I. Day and N. Cumpsty. The measurement and interpretation of flow within rotating stall cells in axial compressors. *Journal of Mechanical Engineering Science*, 20(2):101–115, 1978.

[22] I. Day. Stall inception in axial flow compressors. *ASME J. Turbomach.*, 115(1):1–9, 1993.

[23] F. Moore. A theory of rotating stall of multistage axial compressors: Part 2 - finite disturbances. 106(2)(321-326), 1984.

[24] T. Hynes and E. Greitzer. Method for assessing effects of circumferential flow field distortion on compressor stability. 109(3)(371-379), 1987.

159

[25] E. Greitzer. Surge and rotating stall in axial flow compressors-part i: Theoretical compression system model. *ASME Journal of Engineering Gas Turbine Power*, 98(2):190–198, 1976.

[26] N. M. Mcdougall, N. A. Cumptsy, and T. P. Hynes. Stall inception in axial compressors. *ASME J. Turbmach*, 112(1):116–123, 1990.

[27] I. Day, T. Breur, J. Escuret, M. Cherrett, and A. Wilson. Stall inception and the prospect for active control in four high speed compressors. *ASME J. Turbomach*, 121(1):18–27, 1999.

[28] E. Greitzer. Surge and rotating stall in axial flow compressor part 1: Theoretical compression system model. 98(2)(190-198):9, April.

[29] G. Ludwig and J. Nanni. A rotating stall control system for turbojet engines. *ASME J. Eng. Gas Turbine Power*, 101(3):305–313, 1979.

[30] V. Garnier, A. Epstein, and E. Greitzer. Rotating waves as a stall inception indicator in axial compressor. *ASME J. Turbomach*, 113(2):290–301, 1991.

[31] M. Inuoe, M. Kuroumaru, T. Iwamoto, and Y. Ando. Detection of a rotating stall precursor in isolated axial flow compressor rotors. *ASME J. Turbomach*, 113(2):281–287, 1991.

[32] A. Young, I. Day, and G. Pullan. Stall warning by blade passing signature analysis. *ASME J. Turbomach*, 135(1):011033, 2012.

[33] J. Paduano, A. Epstein, A. Valavani, J. Longley, J. Greitzer, and G. Guennete. Active control of rotating stall in a low speed axial compressor. *ASME J. Turbomach*, 115(1):48–56, 1993.

[34] I. Day. Active suppression of rotating stall and surge in axial flow compressors. *ASME J. Turbomach*, 115(1):40–47, 1993.

[35] C. Gmelin, V. Zander, M. Hecklau, F. Thiele, W. Nitsche, A. Huppertz, and M. Swoboda. Active flow control concepts on a highly loaded subsonic compressor cascade: Resume of experimental and numerical results. *ASME J. Turbomach*, 134(6):061021, 2012.

[36] U. Stark and H. Saathoff. Passive and Active Methods to Enhance Axial Flow Compressor Aerodynamics. *Hermann Schlichting – 100 Years*, pages 145–167, July 2009.

[37] Z. Haideng, W. Yun, and L. Yinghong. Mechanism of Compressor Airfoil Boundary Layer Flow Control Using Nanosecond Plasma Actuation. *International Journal of Heat and Fluid Flow*, 80:108502, 2019.

[38] S. Saddoughi, G. Bennett, M. Boespflug, S. L. Puterbaugh, and A.R. Wadia. Experimental Investigation of Tip Clearance Flow in a Transonic Compressor With and Without Plasma Actuators. *ASME J. Turbomachinery*, 137:041008, 2015.

[39] G. Jothiprasad, R.C. Murray, K. Essenhigh, S. Saddoughi, G. Bennett, A.R. Wadia, and A. Breeze-Stringfellow. Control of Tip-Clearance Flow in a Low Speed Axial Compressor Rotor With Plasma Actuation. *ASME J. Turbomachinery*, 134:021019, 2012.

[40] J. M. Haynes, G. J. Hendricks, and A. H. Epstein. Active stabilization of rotating stall in a three-stage axial compressor. *ASME J. Turbomach*, 116(2):226–239, 1994.

[41] C. Freeman, A. Wilson, I. Day, and M. Swinbanks. Experiments in active control of stall on an aeroengine gas turbine. *ASME J. Turbomach*, 120(4):637–647, 1998.

[42] M. Boyce, R. N. Schiller, and A. R. Desai. Study of casing treatment effects in axial flow compressors. *ASME Journal of Engineering for Power*, 97(4):477–483, 1975.

[43] H. Fujita and H. Takata. A study on configurations of casing treatments for axial flow compressors. *Bulletin Japan Society of Mechanical Engineers*, 27(230):1675–1681, 1984.

[44] H. Takata and Y. Tsukuda. Stall margin improvement by casing treatments-its mechanisms and effectiveness. *ASME Journal of Engineering Gas Turbines and Power*, 99(1):121–133, 1977.

[45] H. Chunill. The Inner Workings of Axial Casing Grooves in a One and a Half Stage Axial Compressor with a Large Rotor Tip Gap: Changes in Stall Margin and Efficiency. *ASME J. Turbomachinery*, (TURBO-18-1152), August 2018.

[46] J. A. Brent. Single stage experimental evaluation of tandem-airfoil rotor and stator blading for compressors. Technical Report N72-26690, NASA, Springfield, Virginia, USA, 1972.

[47] K. Bammert and R. Staude. Optimization for rotor blades of tandem design for axial flow compressors. *ASME J. Turbomach.*, 102(2):369–375, 1980.

[48] A. Kumar, H. Chhugani, S. More, and A.M. Pradeep. Effect of differential tip clearance on the performance of a tandem rotor. *ASME J. Turbomach.*, 144(8):081007, 2022.

[49] M. Mohsen, F. M. Owis, and A. A. Hashim. The Impact of Tandem Rotor Blades on the Performance of Transonic Axial Compressors. *Aerospace Science and Technology*, 67:237–248, 2017.

[50] Boese M. and Fottner L. Effects of Riblets on the Loss Behaviour of a Highly Loaded Compressor Cascade. *Proceedings of the ASME TURBO EXPO 2002*, (GT-2002-30438), June 2002.

[51] C. Lietmeyer, K. Oehlert, and J. R. Seume. Optimal application of riblets on compressor blades and their contamination behavior. *ASME J. Turbomach.*, 135(1):011036, 2013.

[52] Miklosovic D.S., M.M. Murray, L.E. Howle, and F.E. Fish. Leading-edge tubercles delay stall on humpback whale (*Megaptera noaeangliae*) flippers. *Phys. Fluids*, 16(5):L39 –L42, May 2004.

[53] M.M. Zhang, G.F. Wang, and J.Z. Xu. Aerodynamic Control of Low-Reynolds-Number Airfoil with Leading Edge Protuberances. *AIAA Journal*, 51(8):1960–1971, 2013. 10.2514/1.J052319.

[54] K.L. Hansen, R.M. Kelso, and B.B. Dally. Performance Variations of Leading-Edge Tubercles for Distinct Airfoil Profiles. *AIAA Journal*, 49:185–194, 2011.

[55] W.D.E. Allan, A. Asghar, M. LaViolette, and R. Woodason. Influence of a Novel 3D Leading Edge Geometry on the Aerodynamic Performance of Low Pressure Turbine Blade Cascade Vanes. In *Proceedings of ASME Turbo Expo 2014: Turbine Technical Conference and Exposition*, number (GT-2014-25899), Düsseldorf, Germany, June 16-20 2014.

[56] M.D. Bolzon, R.M. Kelso, and M. Arjomandi. Tubercles and Their Applications. *Journal of Aerospace Engineering*, pages 1–10, 2015.

[57] C. Cai, Z. Zuo, S. Liu, and Y. Wu. Numerical Investigations of Hydrodynamic Performance of Hydrofoils with Leading-Edge Protuberances. *Adv. in Mech. Eng.*, 7.

[58] Z. Wei, T.H. New, and Y.D. Cui. An Experimental Study on Flow Separation Controll of Hydrofoils with Leading-Edge Tubercles at low Reynolds Number. *Exp. Fluids*, 47(2):321–331, 2009. 10.2514/1.J052319.

[59] P. T. Soderman. Aerodynamic effects of leading-edge serrations on a two-dimensional airfoil. *Technical Memorandum (TM)*, (NASA-TM-X-2643 A-3706), 1972.

[60] M.M. Miklosovic and D.S. Murray. Experimental Evaluation of Sinusoidal Leading Edges. *J. of Aircraft*, 44(4):1404–1408, Sept 2007.

[61] Z. Wei, T.H. New, and Y.D. Cui. An experimental study on flow separation control of hydrofoils with leading-edge tubercles at low reynolds number. *Ocean Engineering*, 108:336–349, 2015.

[62] A.A. De Paula, B.R.M. Padilha, B.S. Mattos, and J.R. Meneghini. The Airfoil Thickness Effect on Wavy Leading Edge Performance. In *AIAA SciTech Forum - 54th AIAA Aerospace Sciences Meeting*, number AIAA 2016-1306, San Diego, CA, January 4-8 2016.

[63] N. Rostamzadeh, R.M. Kelso, D. D. Dally, and K. L. Hansen. The Effect of Undulating Leading-edge Modifications on NACA 0021 Airfoil Characteristics. *Physics of Fluids*, 25(11):117101, 2013.

[64] A.A. De Paula, J.R. Meneghini, V.G. Kleine, and R.M. Girard. The Wavy Leading Edge Performance for a Very Thick Airfoil. In *AIAA SciTech Forum, 55th AIAA Aerospace Sciences Meeting*, number AIAA 2017-0492, Grapevine, TX, January 9-13 2017.

[65] E.A. van Nierop, S. Alben, and M.P. Brenner. How Bumps on Whale Flippers Delay Stall: an Aerodynamic Model. *Physical Review Letters*, 100(054502):1–4, February 2008.

[66] H.C. Pedro and M. Kobayashi. Numerical study of stall delay on humpback whale flippers. *46th AIAA Aerospace Sciences Meeting and Exhibit*.

[67] A. Dropkin, D. Custodio, C. W. Henoch, and H. Johari. Computation of flow field around an airfoil with leading-edge protuberances. *Journal of Aircraft*, 49(5):1345–1355, 2012.

[68] J.C. Lin. Review of research on low-profile vortex generators to control boundary-layer separation. *Progress in Aerospace Sciences*, 38(4):389–420, 2002.

[69] P. R. Ashill, J. L. Fulker, and K. C. Hackett. A review of recent developments in flow control. *The Aeronautical Journal*, 109(1095):205–232, 2005.

[70] J.F.D. Câmara and J.M.M. Sousa. Numerical Study on the Use of a Sinusoidal leading Edge for Passive Stall Control at Low Reynolds Number. In *AIAA Aerospace Science Meeting Including the New Horizons Forum and Aerospace Exposition*, number AIAA 2013-0062, Grapevine, TX, 7-10 January 2013.

[71] C. Cai, Z. Zuo, M. Morimoto, T. Maeda, Y. Kamada, and S. Liu. Two-Step Stall Characteristic of an Airfoil with a Single Leading-Edge Protuberance. *AIAA Journal*, 56(1):64–77, 2018. 10.2514/1.J055921.

[72] A. Levert-Beaulieu, R. Perez, and P. Jansen. Euler-based aerodynamics shape optimisation of leading edge tubercles in transonic flow. In *Proceedings of the AIAA SciTech Forum and Exposition*, number 1383-1400, San Diego, California, USA, January 2019.

[73] M.D. Bolzon, R.M. Kelso, and M. Arjomandi. The Effects of Tubercles on Swept Wing Performance at Low Angles of Attack. In *19th Australian Fluid Mechanics Conference*, December 2014.

[74] S. Sudhakar, N. Karthikeyan, and L. Venkatakrishnan. Influence of leading edge tubercles on aerodynamic characteristics of a high aspect-ratio uav. *Aerospace Science and Technology*, 69:281–289, 2017.

[75] T. Kohonen. The self-organizing map. *Proceedings of IEEE*, 78:9, 1990.

[76] D. Miljkovic. Fault detection for aircraft piston engine using self-organizing map. *40th MIPRO/CTS*, pages 1258–1263, 2017.

[77] A. Rai and S.H. Upadhyay. Intelligent bearing performance degradation assessment and remaining useful life prediction based on self-organising map and support vector regression. *Proceedings of the Institution of Mechanical Engineers, Part C: Journal of Mechanical Engineering Science*, 232(6):1118–1132, 2018.

[78] G. Huang, Y. Shiah, C. Bai, and W. Chong. Experimental study of the protuberance effect on the blade performance of a small horizontal axis wind turbine. 147(202-211):9, October.

[79] C. Hirsch. *Advanced Methods for Cascade Testing*. North Atlantic Treaty Organization, Advisory Group for Aerospace Research and Development, AGARD-AG-328 edition, 1993.

[80] J. Wetzel and R.E.A. Arndt. Hydrodynamic Design Considerations for Hydroacoustic Facilities: Part I–Flow Quality. *Journal of Fluid Engineering*, 116:224–331, 1994.

[81] Innovative Scientific Solutions Inc. Pressure sensitive paint camera. ISSI booklet, www.psp-tsp.com.

[82] S. Lieblein. Aerodynamic design of axial-flow compressors- vi - experimental flow in two-dimensional cascades. Number NACA RM E55K01a, Lewis flight propulsion laboratory, Cleveland, Ohio, USA.

[83] F.E. Fish and G.V. Lauder. Passive and Active Flow Control by Swimming Fishes and Mammals. *Annual Review of Fluid Mechanics*, 38:193–224, January 2006.

[84] C. Lietmeyer, B. Denkena, T. Krawczyk, R. Kling, L. Overmeyer, B. Wojakowski, E. Reithmeier, R. Scheuer, T. Vynnyk, and J. Seume. Recent advances in manufacturing of riblets on compressor blades and their aerodynamic impact. 135(041008-1).

Appendices

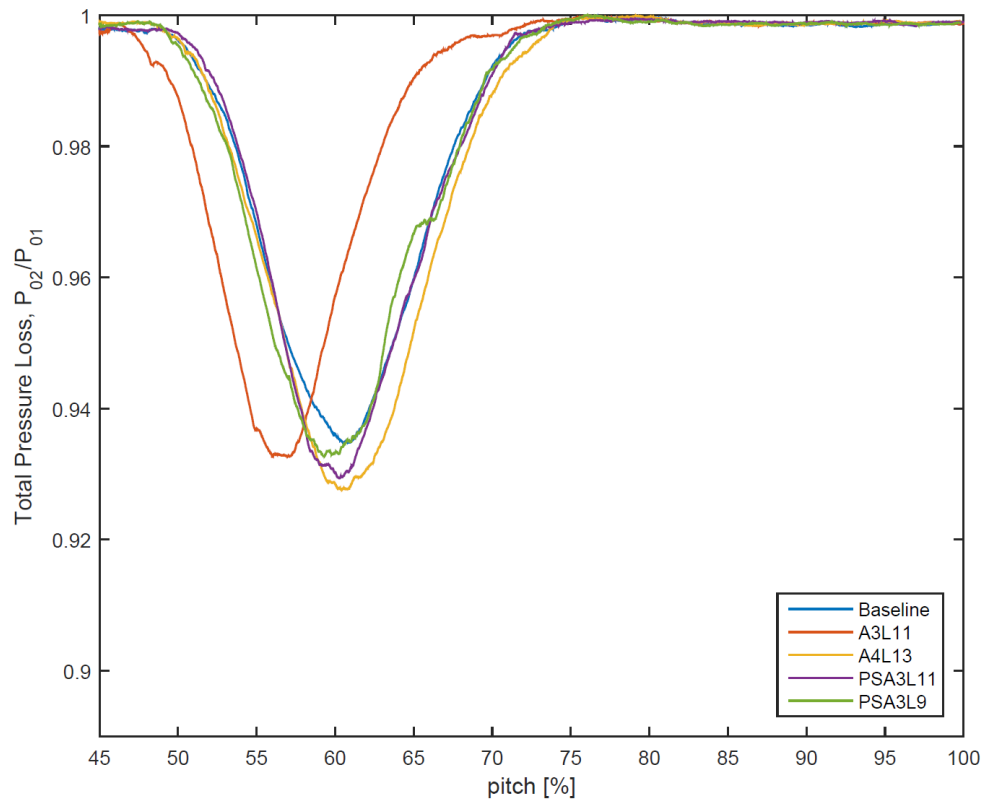# A   Linear Cascade - Wake Measurement Plots

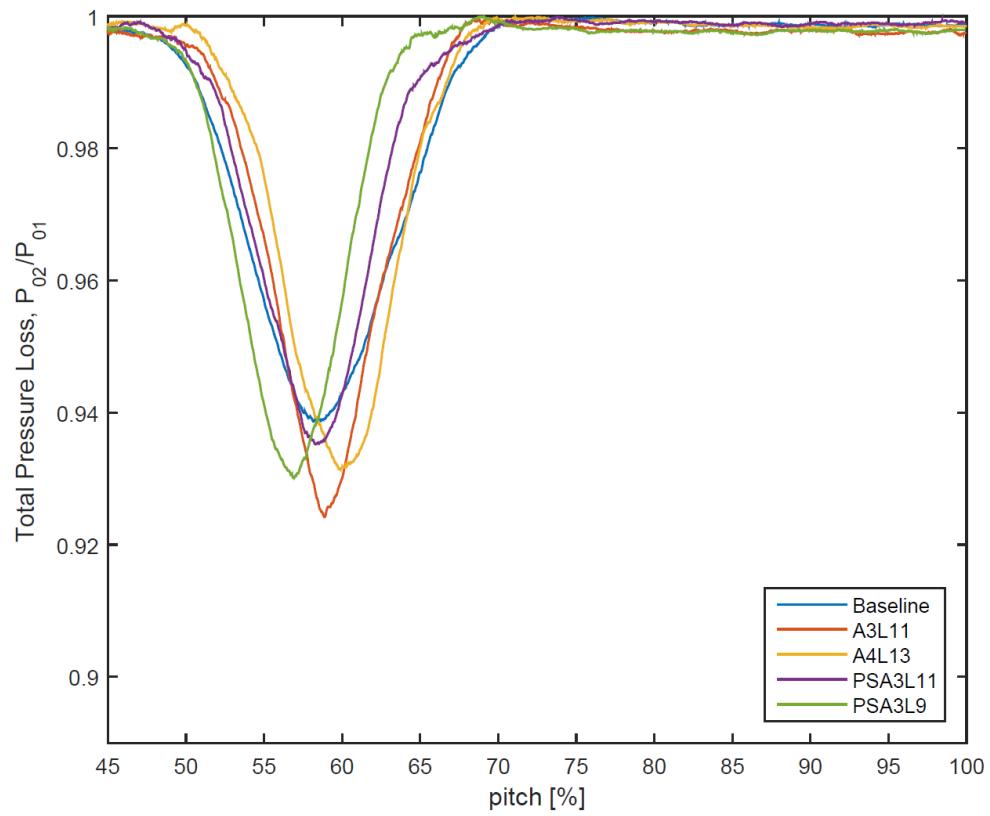Figure A.1: Phase 2 blade wake comparison for all 5 blades at AOI = 0°

Figure A.2: Phase 2 blade wake comparison for all 5 blades at AOI = $2°$

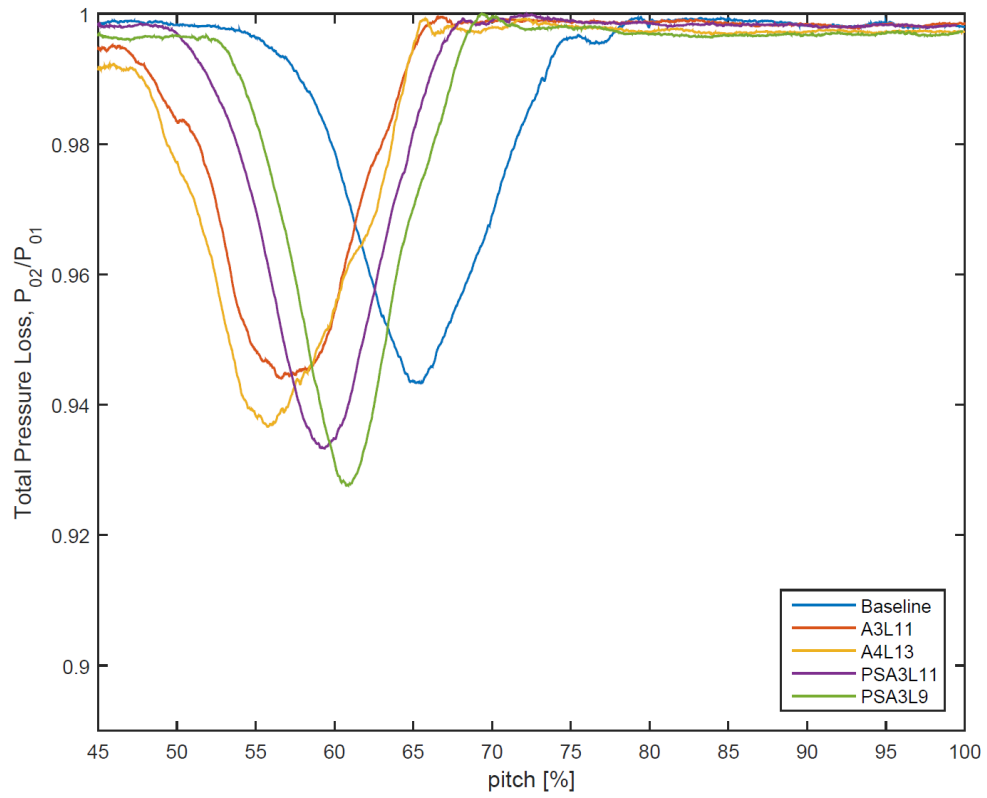Figure A.3: Phase 2 blade wake comparison for all 5 blades at AOI = 4°
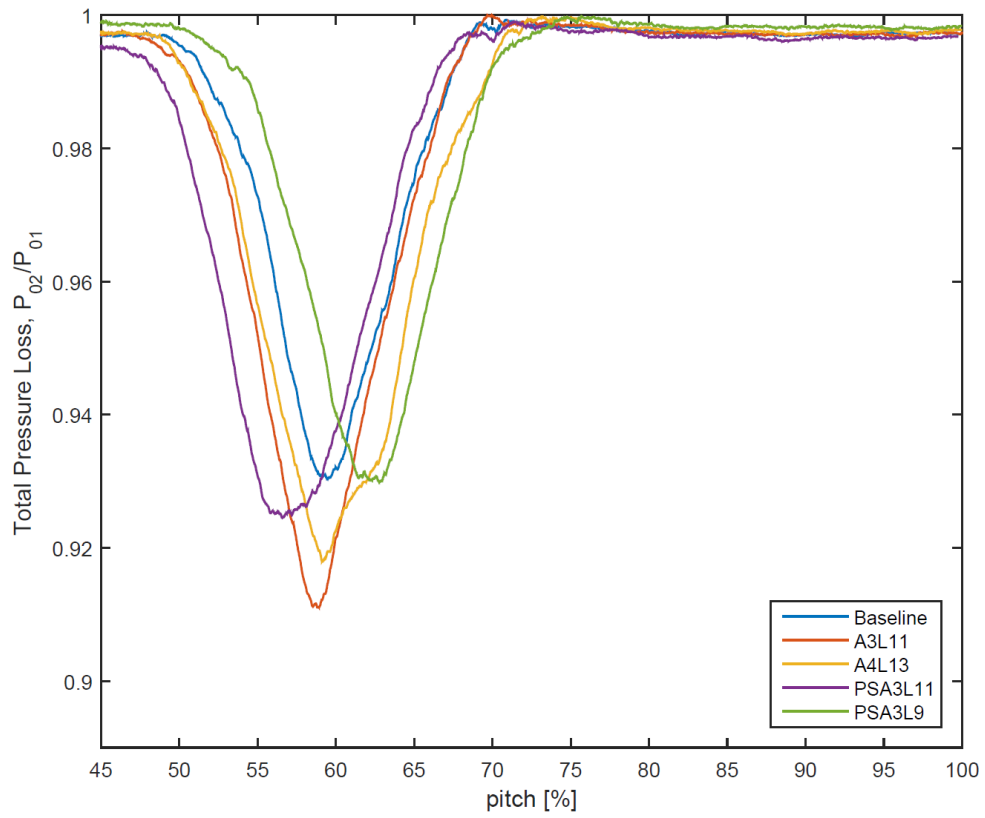
Figure A.4: Phase 2 blade wake comparison for all 5 blades at AOI = 6°
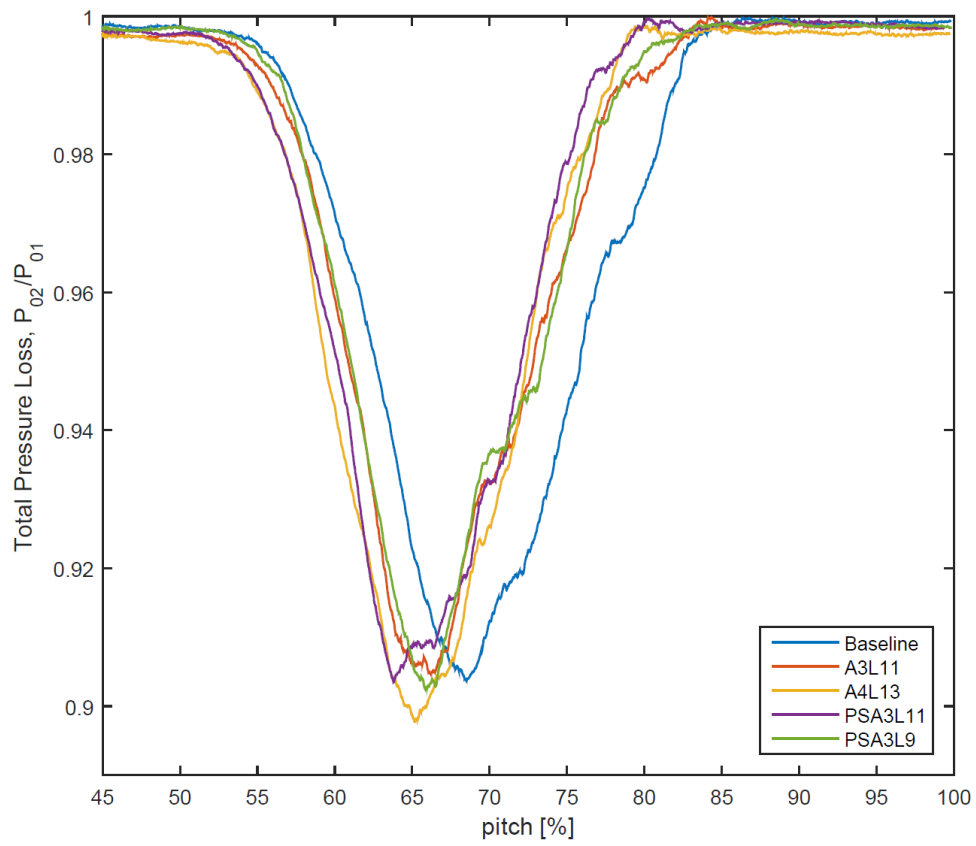
Figure A.5: Phase 2 blade wake comparison for all 5 blades at AOI = 8°

B   Compressor Properties and Uncertainties

B.1   Compressor Blade Properties

Table B.1: Compressor blade properties for each stage [2]

Axial Stage	Number of Rotor Blades	Rotor Hub-Tip Ratio	Number of Stator Blades
1	16	0.38	14
2	20	0.49	26
3	20	0.58	28
4	25	0.64	32
5	28	0.68	36
6	25	0.72	30

B.2   Uncertainity Values

Table B.2: Measurement uncertainities

Sensor	Uncertainty	Units	% Uncertainty Value
XCE-093-50A	± 0.345 [0.05]	kPa [psi]	8.3
XCQ-093-50D	± 0.345 [0.05]	kPa [psi]	8.3
Omega CCT-05	40.4	RPM	0.098
Omega J-Type Thermocouple	1.7	K	8.5
PXI2300-5BDI	± 0.025	psi	0.25
A-Tech 8709 potentiometer	0.1	mm	0.2
PX429-100G5V	0.08	psi	0.08

C   Uncertainty Calculations

C.1   Total Pressure Loss Coefficient

This section demonstrates the uncertainty calculation of total pressure loss coefficient (γ). Total pressure loss coefficient is shown in Equation C.1.

$$\gamma = \frac{P_{01} - P_{02}}{P_{01} - P_{1s}} \tag{C.1}$$

Taking partial derivative of each variable will give three distinct relations shown in Equation C.2, C.3 and C.4.

$$\frac{\partial \gamma}{\partial P_{02}} = \frac{1}{P_{1s} - P_{01}} \tag{C.2}$$

$$\frac{\partial \gamma}{\partial P_{01}} = \frac{P_{02} - P_{1s}}{(P_{01} - P_{1s})^2} \tag{C.3}$$

$$\frac{\partial \gamma}{\partial P_{1s}} = \frac{P_{01} - P_{02}}{(P_{01} - P_{1s})^2} \tag{C.4}$$

The uncertainty of γ can be calculated by combining three partial derivatives as shown in Equation C.5.

$$\delta_\gamma = \sqrt{\left(\frac{\partial \gamma}{\partial P_{02}} \delta_{P_{02}}\right)^2 + \left(\frac{\partial \gamma}{\partial P_{01}} \delta_{P_{01}}\right)^2 + \left(\frac{\partial \gamma}{\partial P_{1s}} \delta_{P_{1s}}\right)^2} \tag{C.5}$$

The total pressure loss coefficient was calculated to be approximately 0.000404 psi and uncertainty percentage of around 0.808% when compared against maximum γ value.

C.2 Pressure Ratio

Pressure ratio of A-250 compressor was calculated using Equation C.6.

$$PR = \frac{P_2}{P_{01}} \tag{C.6}$$

The partial derivatives of the pressure ratio with its variables are shown in Equation C.7 and C.8

$$\frac{\partial PR}{\partial P_2} = \frac{1}{P_{01}} \tag{C.7}$$

$$\frac{\partial PR}{\partial P_{01}} = -\frac{P_2}{(P_{01})^2} \tag{C.8}$$

Pressure ratio uncertainty can be calculated using Equation C.9.

$$\delta_{PR} = \sqrt{\left(\frac{\partial PR}{\partial P_2} \delta_{P_2} \right)^2 + \left(\frac{\partial PR}{\partial P_{01}} \delta_{P_{01}} \right)^2} \tag{C.9}$$